

UC Davis

UC Davis Previously Published Works

Title

Highly Reliable Compact RF-MEMS Contact Switch: Design, Fabrication and Characterization

Permalink

<https://escholarship.org/uc/item/8sc0p500>

Author

Liu, Yuhao

Publication Date

2016-12-01

Copyright Information

This work is made available under the terms of a Creative Commons Attribution-ShareAlike License, available at <https://creativecommons.org/licenses/by-sa/4.0/>

Peer reviewed

Highly Reliable Compact RF-MEMS Contact Switch: Design,
Fabrication and Characterization

By

YUHAO LIU
B.ENG. (McMaster University) 2011

DISSERTATION

Submitted in partial satisfaction of the requirements for the degree of

DOCTOR OF PHILOSOPHY

in

Electrical and Computer Engineering

in the

OFFICE OF GRADUATE STUDIES

of the

UNIVERSITY OF CALIFORNIA

DAVIS

Approved:

Xiaoguang Liu

Anh-Vu Pham

Q.Jane Gu

Committee in Charge

2016

Copyright © 2016 by

Yuhao Liu

All rights reserved.

*To my parents, Yadong Liu and Yun Tang, who give me endless love and support,
and to my uncle (dajiu), Ping Tang, who taught me Ohm's law when I was six.*

CONTENTS

List of Figures	vi
List of Tables	xi
Abstract	xii
Acknowledgments	xiv
1 Introduction	1
1.1 RF-MEMS Switches Technology	1
1.2 Reliability Issues in RF-MEMS Switches	7
1.3 Hot-switching Damage of RF-MEMS Metal Contact Switch	12
2 Extension of the Hot-Switching Reliability of RF-MEMS Switches Using A Series Contact Protection Technique	16
2.1 Introduction	16
2.2 Device concept	16
2.2.1 OFF-state to ON-state	19
2.2.2 ON-state to OFF-state	23
2.3 Switch Design and Modeling	24
2.3.1 Switch Geometries	24
2.3.2 Mechanical Design and Simulation	26
2.3.3 EM Analysis	34
2.4 Device Fabrication	34
2.5 Measurement and discussion	37
2.5.1 Actuation voltage	37
2.5.2 S-parameters	38
2.5.3 Linearity	38
2.5.4 Switching time	40
2.5.5 Mechanical cycle test	43

2.5.6	Hot-switching lifetime	45
2.6	Conclusion	47
3	High-Power High-Isolation RF-MEMS Switches with Enhanced Hot-switching Reliability Using A Shunt Protection Technique	49
3.1	Introduction	49
3.2	Analysis and Design	50
3.2.1	Comparison Between Shunt Protected Switch and Unprotected Switch (From OFF to ON/ ON to OFF)	50
3.2.2	Comparison Between Shunt-protected Switch and Series-protected Switch	55
3.2.3	Switch Design and EM Analysis	64
3.3	Experimental Validation	64
3.3.1	Device Fabrication	64
3.3.2	S-Parameters	69
3.3.3	Linearity Test	71
3.3.4	Switching Time	71
3.3.5	Mechanical Cycle Test	73
3.3.6	Hot-switching Lifetime Test	74
3.4	Conclusion	78
4	Single-Actuator Shunt-Series RF-MEMS Switch for Improved Hot Switching Performance and Isolation	80
4.1	Introduction	80
4.2	Design	80
4.3	Experimental Validation	85
4.3.1	Fabrication	85
4.3.2	Measurement and Discussion	85
4.4	Conclusion	86

A	Metal Contact RF MEMS Switch Fabrication Process	90
A.1	Introduction	90
A.2	Fabrication Process	90
A.2.1	Wafer Preparation	90
A.2.2	Silicon Chrome Biasing Line	90
A.2.3	Gold Metal Contact Line	91
A.2.4	Platinum Protection Contact	92
A.2.5	Chromium Sacrificial Layer	92
A.2.6	Dimple Layer	93
A.2.7	Seed Layer	93
A.2.8	Plating and Release	94

LIST OF FIGURES

1.1	A variety of MEMS devices.	2
1.2	Cross-section view and electrical CLR model of (a) Metal contact RF MEMS switches; (b) Capacitive RF MEMS switches.	3
1.3	A variety of RF-MEMS switches: (a) and (b) Capacitive RF MEMS switches; (c) and (d) Metal contact RF MEMS switches	4
1.4	Application areas of RF-MEMS: (a) switching matrices, (b) wide- band front-end receivers, and (c) passive base-station antennas . . .	8
1.5	a) Frictional polymer formation in a Ru contact; (b) adhesion failure with Au contact material being removed when switch is forced open; (c) excessive material transfer and reshaping of the contacts	9
1.6	Material transfer phenomenon under hot-switching voltage.	12
2.1	Concept of RF-MEMS switch with series protection contact : (a) 3-D view; (b) Top view; (c) Profile view;	17
2.2	Switching sequence of the device: (a) Off-state; (b) Transition-state from off-state to on-state; (c) On-state; (d) Transition-state from on-state to off-state.	18
2.3	Equivalent circuit model of switches (a) without protection and (b) with protection.	20
2.4	(a) Calculated electric field intensity of unprotected switch and switches with different protection contact resistances (at RF fre- quency of 2.4 GHz). (b) Zoom-in view of (a) for low protection contact resistance.	22
2.5	(a) Calculated electric field intensity under different input power levels without the protection contacts at 2.4 GHz at the closest gap (0.5 μm); (b) Calculated electric field intensity under various input power levels with the protection contacts at 2.4 GHz at the closest gap (0.5 μm) with respect to different protection contact resistances.	23

2.6	Dimensions of the proposed switch. (a) Top view; (b) Side view. . .	24
2.7	Beam profile predicted by theoretical model under different biasing voltages.	29
2.8	Calculated and simulated contact force under different biasing voltages.	29
2.9	Calculated and simulated restoring force of protection contact for different dimple positions.	31
2.10	Simulated Von Mises Stress under 90 V actuation voltage.	31
2.11	Beam deflection due to positive stress gradient.	32
2.12	First (a) and second (b) contact dimple movement under different actuation voltage with different negative stress gradient.	33
2.13	Simulated insertion loss and isolation for different switching stages.	35
2.14	Simulated surface current distribution (a) when the protection contacts are closed, and (b) when the low-resistance contacts are closed.	35
2.15	Fabrication process of the switch.	36
2.16	(a) Optical images of a pair of protected (left) and unprotected switch (right), (b) Scanning electron microscope (SEM) image of the fabricated switch (left) and zoom-in picture (right).	37
2.17	(a) Measured S-parameters, (b) Zoom in of (a) from 0 GHz - 6 GHz	39
2.18	(a) Linearity test setup schematics, and measured IIP3 for both (b) through line and (c) MEMS switch.	40
2.19	(a) Test setup schematics for switching time measurement, (b) test setup schematics for hot-switching lifetime characterization.	41
2.20	Test bench photo for S-parameters, switching time and reliability measurement.	42
2.21	(a) Switching-on time of protected switch, (b) switching-off time of protected switch.	43
2.22	(a) Switching-on time of unprotected switch, (b) switching-off time of unprotected switch.	44

2.23	Contact resistance changes of the protection contact and low-resistance contact over 500 million mechanical cycles.	44
2.24	(a) Measured contact resistances of switches pair under 1 W of different cycling numbers, (b) contact resistances of switches pair under 2 W of different cycling numbers.	46
3.1	Concepts of (a)-(c) series-protection scheme for hot-switching life-time enhancement.	51
3.2	Concepts of (a)-(c) the proposed shunt-protection scheme for hot-switching life-time enhancement.	52
3.3	Equivalent circuit of (a) switch without protection at the moment of hot-switching; (b) switch with shunt protection at the moment of hot-switching (step B1, B4).	54
3.4	(a) Calculated electric field intensity of unprotected switch and switches with different shunt protection contact resistances; (b) zoom in of (a) for low shunt protection resistance.	56
3.5	Ratio between the electric field intensity on the main contacts of the protected switch and the unprotected switch.	56
3.6	Equivalent circuit of (a) switch with series protection at the moment of hot-switching (step A2, A3); (b) switch with shunt protection at the moment of hot-switching (step B2, B3).	57
3.7	Comparison between the calculated electric field intensity of the main contacts of the series-protected and shunt-protected switches when the protection contact resistances are (a) 20 Ω ; (b) 10 Ω ; (c) 5 Ω ; (d) 2 Ω . The calculation assumes a center frequency of 2.4 GHz.	58
3.8	Equivalent circuit of (a) switch with series protection before the protection contact is closed (open) (step A1, A2); (b) switch with shunt protection before the protection contact is closed (open) (step B0).	59

3.9	Equivalent circuit model of the shunt-protected switch when the protection contact is about to open (close) while the main contact is closed (step B2, B3).	61
3.10	Calculated S-parameter for a shunt-protected switch, a series-protected switch and an unprotected switch.	63
3.11	(a) Top view of the shunt-protected switch; (b) side view of the cantilever.	65
3.12	(a) Current distribution of the switch before the main switch closed; (b) current distribution of the switch after the main switch closed.	67
3.13	Simulated (a) isolation of the switch in INITIAL state, HIGH ISOLATION state, and TRANSITION state; (b) insertion loss of the switch in the ON state.	68
3.14	Pictures of the (a) protected switch and (b) unprotected switch.	69
3.15	Measured S-parameter of shunt-protected switch: (a) isolation of INITIAL state, HIGH ISOLATION state, and TRANSITION state; (b) insertion loss of ON state.	70
3.16	Measured S-parameter of unprotected switch: (a) isolation of OFF state; (b) insertion loss of ON state.	71
3.17	(a) Linearity test setup; (b) IP3 of the shunt-protected MEMS switch; (c) IP3 of the through line.	72
3.18	Setup schematics for switching time measurement.	73
3.19	(a) Switching-on time; (b) switching-off time.	74
3.20	Mechanical cycling test for two RF-MEMS switch devices (Test stopped after the last data points were collected).	75
3.21	Test setup for hot-switching reliability characterization.	76
3.22	Contact resistances changes over cycling period of three unprotected switches under 1-W hot-switching condition (All devices failed as open circuit at the next data points collection).	76
3.23	Actuation waveform for the shunt protected switches.	77

3.24	Contact resistances changes over cycling period of three protected switches under 1-W hot-switching condition (All devices failed as open circuit at the next data points collection).	77
3.25	Contact resistances changes over cycling period of three continuous protected switches under 1-W hot-switching condition (One device failed as open circuit at the next data point collection, and for the other two devices test stopped after the last data points were collected).	78
4.1	Concept of single-actuator shunt-series RF MEMS switch: (a) Top view; (b) Profile view; Equivalent circuits of (c) isolation state; (d) Equivalent circuit of transition state when both series and shunt contacts are closed; (e) Equivalent circuit of closed state.	81
4.2	Simulated electromechanical and RF performances of the proposed shunt-series RF MEMS switch: (a) Off state; (b) High isolation state; (c) Transition state; (d) ON state.	82
4.3	Summary of key fabrication process steps of high isolation MEMS switch: (a) SiCr biasline patterning; (b) Bottom gold contact layer; (c) Cu sacrificial layer; (d) Photoresist dimple patterning; (e) Au electroplating for cantilever beam; (f) Released cantilever beam. . .	86
4.4	(a) SEM of the fabricated RF MEMS switch; (b) Optical image of the switch.	87
4.5	Measured performance of the shunt-series switch: (a) Off-state; (b) High isolation state; (c) Transition from high-isolation- to on-state; (d) On state.	88

LIST OF TABLES

1.1	Comparison between different types of tuning devices.	6
2.1	Geometry parameters of the switch	25
2.2	Comparison of switch lifetime under hot-switching condition	48
3.1	Geometry parameters of the switch	66

Abstract of the Dissertation

Highly Reliable Compact RF-MEMS Contact Switch: Design, Fabrication and Characterization

The dissertation presents techniques that can address reliability degradation of radio frequency micro-electromechanical (RF-MEMS) metal contact switches due to hot-switching damages. In the first proposed technique, sacrificial contacts are placed in parallel with low-resistance contacts to significantly reduce the electric field across the latter. The lower field strength drastically reduces the contact degradation associated with field induced damages. Theoretical and numerical modeling show that the proposed protection scheme introduces minimal, if any, impact on the switch's RF performance. To realize the protection scheme, a novel cantilever structure was designed to allow the correct protection actuation sequence to be realized using a single actuator and bias electrode. Experiments show that, the protected switch design exhibits over 100 times improvement in hot-switching lifetime compared with unprotected switches. In particular, the series-protected switches can achieve 100–150 million cycle lifetime at 1 W hot-switching and 50 million cycles at 2 W hot-switching before catastrophic failure, in an open-air lab test setup.

The second proposed scheme is a shunt protection technique to improve the hot-switching reliability. The proposed technique places shunt protection contacts in front of the main contact of an RF-MEMS metal contact switch to block the RF signal while the main contact is switching on or off. The shunt protection contact creates a local cold-switching condition for the main contact to increase the lifetime of the switch under hot-switching condition. The shunt protection technique can also increase the overall isolation of the switch. Experiments shows that the protected switch has 50 times longer lifetime under hot-switching condition compared with unprotected switch. The protected switch has >100 million cycles and up to 500 million cycles lifetime under 1-W hot-switching condition, measured

in open-air lab environment. Besides, the isolation of the shunt-protected switch is 70 dB at 1.0 GHz and 36 dB at 40 GHz, and insertion loss is 0.30 dB at 1.0 GHz and 0.43 dB at 40 GHz. A compact switch design using a single actuator and bias electrode with shunt protection contact was also proposed and experimentally demonstrated.

Acknowledgments

I would like to thank many people for their help to get me here and let me have the chance to finish my dissertation. First and foremost, I would like to thank my Ph.D advisor, Prof. Xiaoguang Liu for his invaluable support, guidance, and encouragement over the past five years. He not only taught me a great amount of things on technical issues, but also guided me to think independently and creatively. It has been a great honor and pleasure working with Prof. Liu. I am lucky and grateful to be his student. I would also like to thank Prof. Anh-Vu Pham and Prof. Q. Jane Gu for reviewing my thesis and Ph.D. work and serving as my committee members.

I would like to express my gratitude to the staff members of the CNM2 clean-room at UC Davis for all of the support, including Corey D. Wolin, Dr. Yusha, Bey, Rijuta Ravichandran, and Dr. Chan Ho Kim. Without their timely maintenance, I can never finish my fabrication easily and on time.

Next, I would like to thank my colleagues at DART lab for their support and friendship including: Akash Anand, Songjie Bi, Naimul Hasan, Hao Wang, James Do, Daniel Kuzmenko, Meijiao Li, and Fengqi Hu. I would also like to thank my colleagues and friends at ECE department for making this journey a pleasant experience including: Bo Yu, Yu Ye, Jinbo Li, Shilei Hao, Jeronimo Segovia, Hooman Rashtian, Yaping Liang, Qianteng Wu, Juan Zeng, Binzhi Li, Kuanping Shang, Chuan Qin, Yunpeng Zhu, Binbin Guan, Stanley Cheung, Stevan Djordjevic, Runxiang Yu and Huan Tang.

Thank you to my friends in China, U.S, and Canada who are always there for me including: Wei Wang, Yihang Zhang, Chen He, Yu Luo, Yao Nie, Tian Yu, Xiaofei Shao, Hai Wang, Weishu Kong, Jing Jiang, Zhengyang Mao, Shengli Lin, Yilong Wang, Mengdi Chen, Yue Zhang and Songzhi Jing.

Finally, I would like to thank my family in China for their unconditional love and support, especially to my parents, Yadong Liu and Yun Tang for their care and attention over the years. I could not finish my education without their help. I

would also like to thank my uncle, Ping Tang, who passed away in 2014. He was an electrical engineer before retired. He inspired my interest in electrical engineering when I was a kid. I can always remember the summer time when he took me to his lab and we discussed Ohm's law and capacitors. May you rest in peace, as memories of you live on.

Chapter 1

Introduction

1.1 RF-MEMS Switches Technology

There's plenty of room at the bottom [1]. Since its introduction in 1990s, Micro-Electro-Mechanical-Systems (MEMS) have dramatically evolved and matured. By using micro-machining techniques, MEMS device can achieve small size varying from less than a micron to a few millimeters. Different actuation mechanisms and device physical properties than are not available in macro-devices can be achieved and used by shrinking the device size. Controlling electronics (Integrated circuit) can also be fabricated alongside MEMS device using standard IC fabrication and integrated with MEMS device [2]. MEMS has a broad range of applications. Typical MEMS devices can be found in different categories of application: ink-jet printers [3], accelerometers [4], gyroscopes [5], displays [6], optical switching [7], microphone [8], bio-MEMS [9], RF-MEMS switches [10] and etc. Fig 1.1 shows a variety of MEMS devices.

RF MEMS switches are miniature devices that can manipulate RF current flow with mechanical moving part on top of RF circuits. The actuation mechanisms of the moving part can be electrostatic [14], magnetic [15], thermal [16], and piezoelectric [17]. There are two major categories of RF MEMS switches: capacitive switches and metal-contact switches [18]. The capacitive switches manipulate the RF currents by capacitively coupling to RF circuits, while the metal-contact

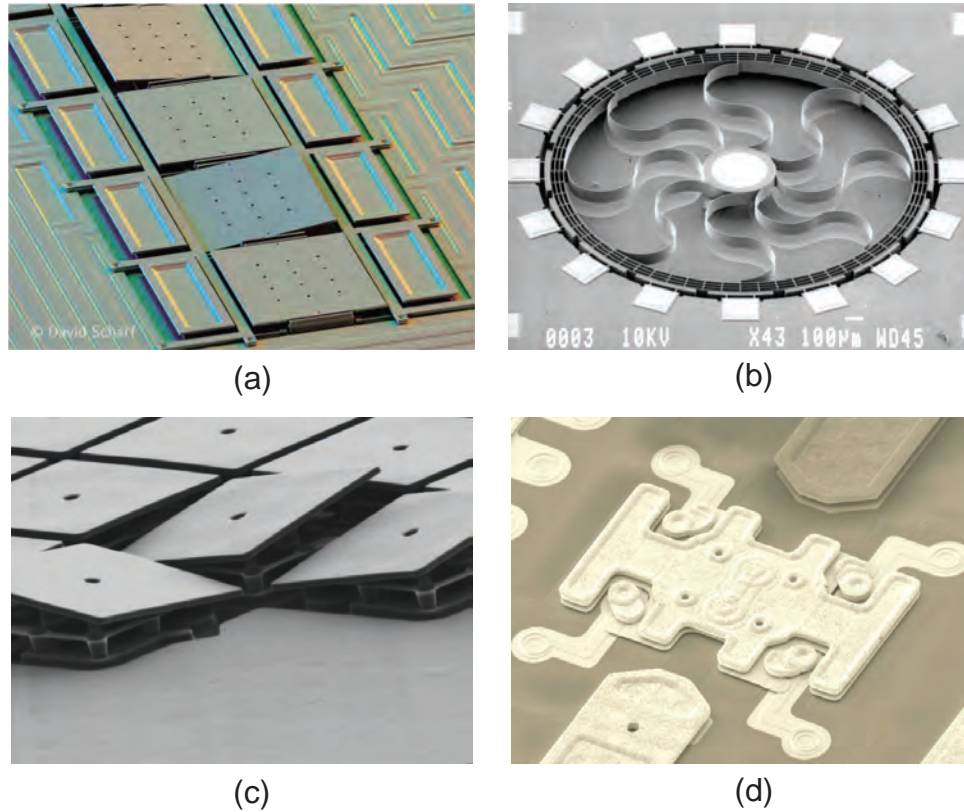


Figure 1.1. A variety of MEMS devices: (a) Optical MEMS switch ©2006 IEEE. Reprinted, with permission, from [11]; (b) MEMS gyroscope ©2000 IEEE. Reprinted, with permission, from [12]; (c) Texas Instruments MEMS display ©1998 IEEE. Reprinted, with permission, from [6]; (d) DelfMEMS RF MEMS switch ©2007 IEEE. Reprinted, with permission, from [13].

switches manipulate RF currents by making directing metal contact to RF circuits. Fig 1.2 shows the cross-section view and electrical CLR model, and Fig 1.3 shows SEM images of several capacitive RF MEMS switches and metal contact RF MEMS switches receptively. Gold is often used as metal contact to lower contact resistance in metal contact RF MEMS switch. The dielectric film in capacitive RF MEMS switches enhances the on-state and off-state capacitance ratio.

Compared with other RF switches (p-i-n Diode, YIG, BST, Schottky Diode, Silicon-on-Insulator (SOI) switch), RF MEMS switches have several strength [18, 19, 24]:

1. Extremely low loss (<0.2 dB), low on-resistance (0.5Ω - 2Ω for metal-contact devices, 0.1Ω - 0.2Ω for capacitive devices), low off-state capacitance (2 ff- 16 ff),

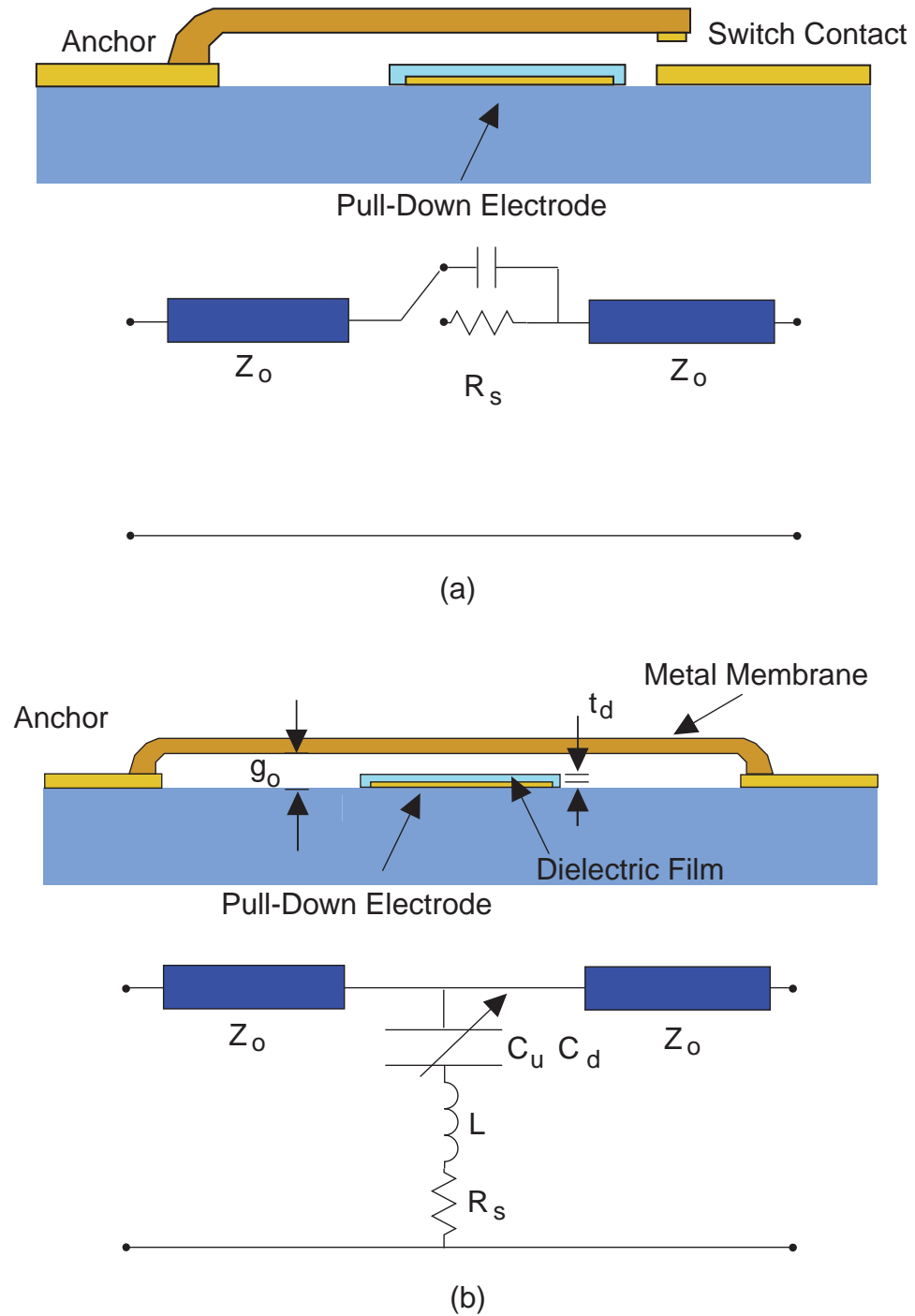


Figure 1.2. Cross-section view and electrical CLR model of (a) Metal contact RF MEMS switches; (b) Capacitive RF MEMS switches. ©2001 IEEE. Reprinted, with permission, from [19]

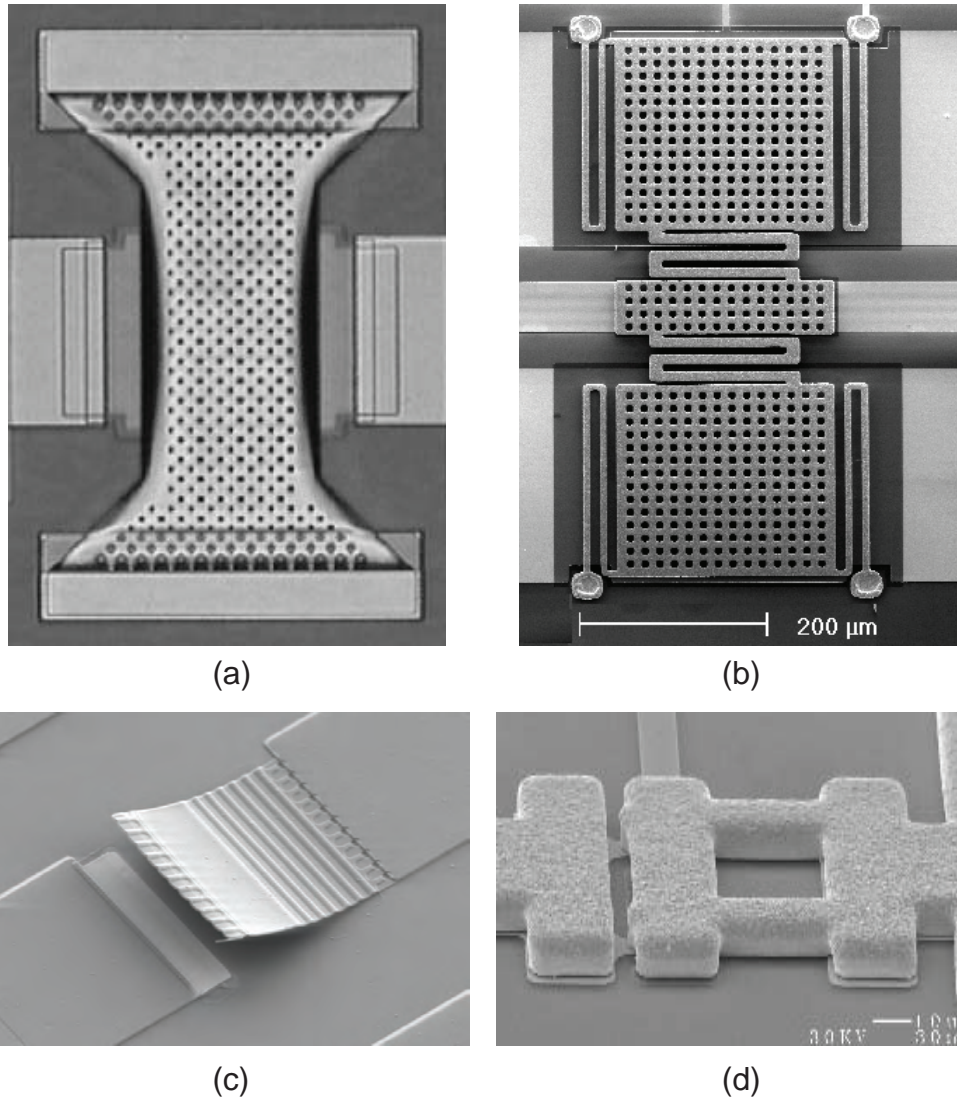


Figure 1.3. A variety of RF-MEMS switches: (a) and (b) Capacitive RF MEMS switches ©1998 IEEE. Reprinted, with permission, from [20], ©2000 IEEE. Reprinted, with permission, from [21]; (c) and (d) Metal contact RF MEMS switches ©2001 IEEE. Reprinted, with permission, from [22], ©2012 IEEE. Reprinted, with permission, from [23].

very high isolation up to mm-wave frequencies. The figure of merit of RF switch is defined by ($FOM = R_{on}C_{off}$). The FOM of RF MEMS switch is in the range of 0.2 fs-32 fs, very small comparing to SOI and GaAs switches [25].

2. Very high linearity: For identical input powers, RF MEMS switches are 20 dB-50 dB better than GaAs or SOI devices [25].

3. High voltage swing handling. In some applications, such as antenna tuning, a large RF voltage swing appears across the switch. RF-MEMS switch can handle voltage swing much better than GaAs or SOI device. Unlike FET switch, the biasing line of RF MEMS switch is isolated from the RF terminals. The RF voltage swing will not cause biasing problem of the switch.

4. High power handling: RF MEMS switches can usually handle 1 W-10 W.

The RF MEMS switch also has some disadvantages:

1. Hermetic packaging: Hermetic packing can increase the reliability of RF MEMS switch. However, hermetic packing can increase the cost of the device.

2. High voltage biasing voltage: The biasing voltage for a reliable RF MEMS switches is in the range of 25 V-90 V. High-voltage drive circuits are needed for biasing RF MEMS switches.

3. Reliability: Capacitive RF MEMS switches has problems with dielectric charging, and metal contact RF MEMS switch has reliability problems of the metal contact [26].

Table 1.1 shows the comparison between different types of RF tuning devices [24].

RF MEMS switches were initially developed for low-cost and high-performance phase shifters and wide-angle 77 GHz switched-beam systems and phase arrays [27–30]. Then, RF-MEMS switches were designed to replace p-i-n diode and GaAs FET switches in cellphone front-end. However, advances in SiGe, CMOS, and SOI (Silicon-on-insulator) technology has virtually eliminated RF MEMS switches from applications above. High-performance and highly dense phased array can be designed in SiGe and CMOS process [31, 32]. Switches designed in SOI technology

Table 1.1. Comparison between different types of tuning devices. ©2009 IEEE. Adapted, with permission, from [24]

	YIG	BST	Schottky Diode	p-i-n Diode	MEMS
Q	500-2000	30-150	30-150	$R_s = 1\Omega$	50-400
Tuning Range	2-18 GHz	$C_r = 2 - 3$	$C_r = 3 - 5$	High	$C_r = 2 - 100$
Tuning Speed	ms	ns	ns	ns	μs
Linearity, IIP3 (dBm)	20	10-35	10-35	>33	>60
Power Handling (mW)	50-200	20-200	10-100	High	100-1000
Power Consumption	0.5-5 W	0	0	20-30 mA	0
Temperature Sensitivity	High	High	Low	Low	Low
Biasing	Magnet	High R	High R	LC choke	High R
Planar	No	Yes	Yes	Yes	Yes
Cost	High	Low	Low	Low	Low

has also been dominated cellphone RF front-end [25] due to its significantly lower cost than RF MEMS switches. Although RF MEMS does not succeed in those applications, there are still a wide range of applications that only RF-MEMS switches can fulfill [33]:

(1) **Automated Test Equipment** The ATE usually requires low-insertion, high-isolation and high-linearity switching elements from DC to RF. RF MEMS switch can provide such switching ability from 0 to 60 GHz. There are commercially

available RF MEMS switches for ATE application [34].

(2)**Switching Matrices** RF-MEMS switches can be used in switching matrices, which is critical for satellite and defense application [35].

(3)**Defense Systems** RF-MEMS switches can provide much better performance than GaAs devices. Tunable filters, attenuators, true-time delay line in wide-band RF

transceivers can benefit from low-loss, high-isolation and high-linearity RF-MEMS switches.

(4)**Intelligent Base-State Antennas** RF MEMS switches can be used in next generation of antennas in base station. The antenna needs tuning abilities to achieve beam scanning and pattern nulling. RF-MEMS switches is the enabling device to achieve the tuning abilities.

Fig. 1.4 shows the potential application of RF-MEMS switches.

1.2 Reliability Issues in RF-MEMS Switches

Despite there are a wide range of potential applications of RF-MEMS switches, reliability issues has hindered the practical use of RF MEMS switches in RF systems. Intense research efforts has been devoted to resolve reliability issues [36].

For capacitive RF MEMS switch, the dominant failure mode is the charging of the dielectric layer. The charging is due to the charge injection during electrode actuation and charge trapping in the dielectric layer. There are two failure cases in capacitive actuation [36]. The first one is that the beam returns to the up-state position after applying actuation voltage. In this case, the charge is transferred from the metallic beam to the surface states and the force applied on the beam is reduced, causing the beam to return to the up-state position. The pull-down voltage also increases because the charge will remains on the surface states. The second one is that the charge trapped in the dielectric film, and the charge actuates the beam even when the biasing voltage is removed. The methods used to reduce charging dielectric film includes [18]: (a) Use of different dielectric materials. The

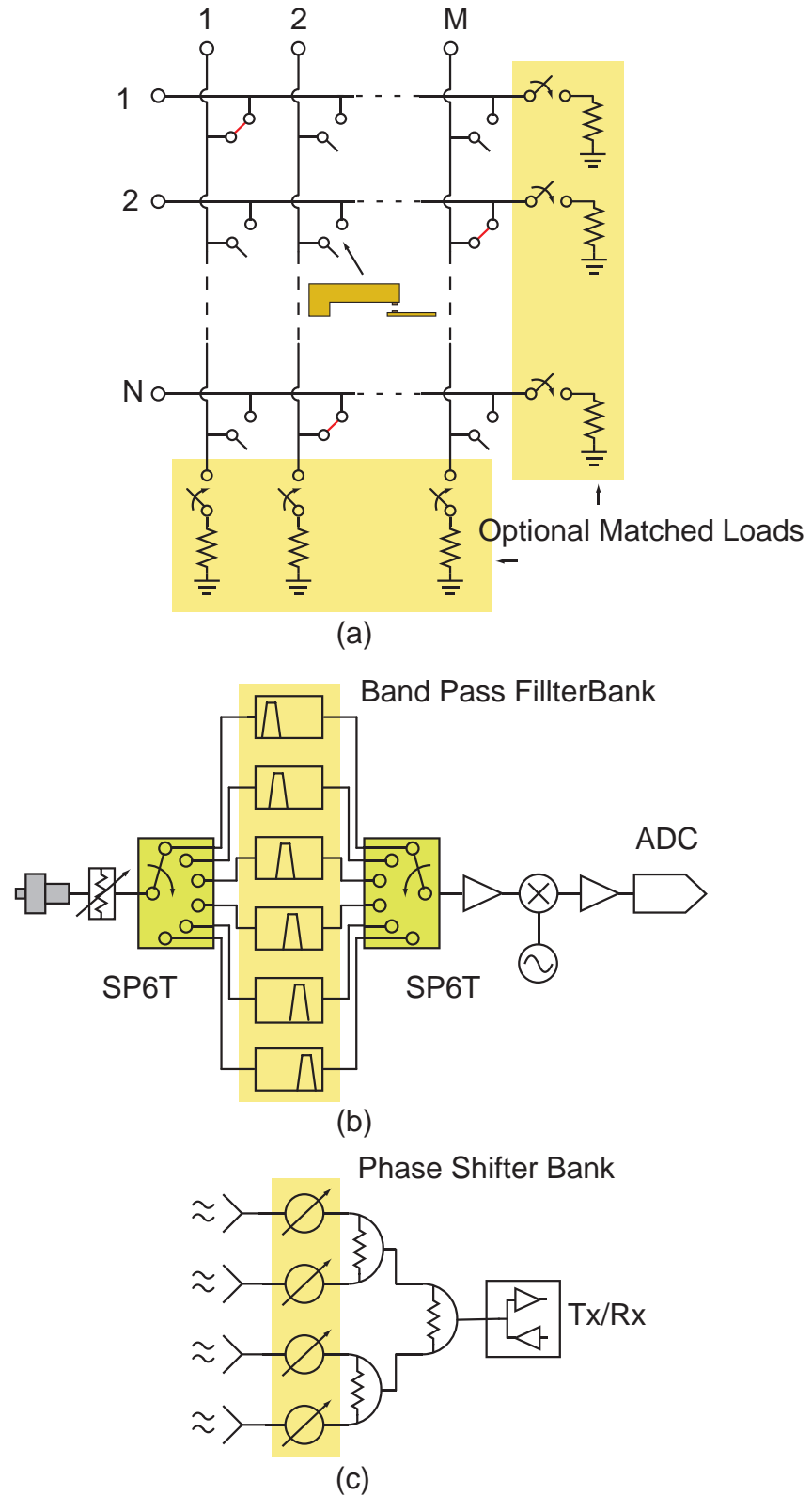


Figure 1.4. Application areas of RF-MEMS: (a) switching matrices, (b) wide-band front-end receivers, and (c) passive base-station antennas. ©2013 IEEE. Reprinted, with permission, from [33]

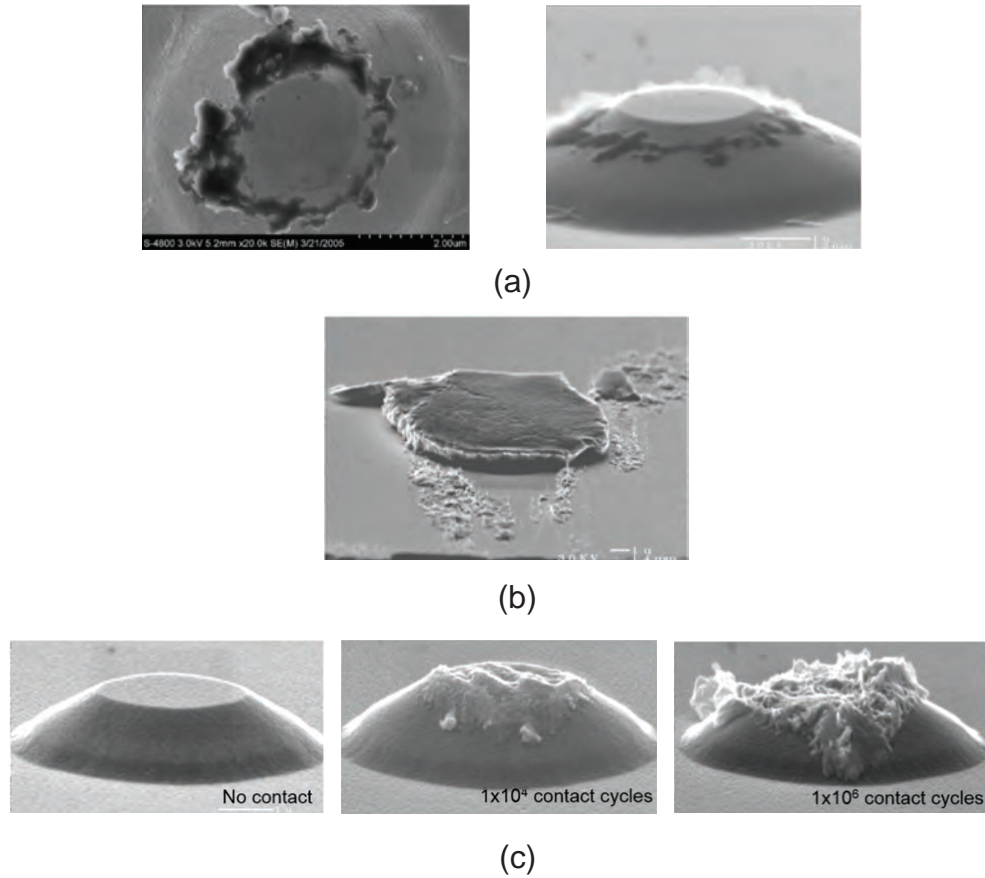


Figure 1.5. (a) Frictional polymer formation in a Ru contact; (b) adhesion failure with Au contact material being removed when switch is forced open; (c) excessive material transfer and reshaping of the contacts. ©2016 IOPScience. Reprinted, with permission, from [26].

dielectric charging problem can be minimized by using silicon dioxide as dielectric layer rather than silicon nitride. (b) Use of bipolar actuation. The net charge injection from both positive and negative bias voltage combined can be much lesser than unipolar charge injection, improving the reliability of the switch. (c) Use of different designs. Without exposing the dielectric film from DC biasing electric directly, the dielectric film can face less charging.

There are a number of failure modes associated with metal-contact RF-MEMS switches. The failure modes include (1) contact bouncing [37]; (2) contamination/frictional polymer formation [38], shown in Fig. 1.5 (a); (3) contact fretting [39]; (4) contact pitting [39]; (5) contact stiction [40], shown in Fig. 1.5(b); (6)

Cantilever creep; (7) material transfer mechanisms caused by hot-switching [41], shown in Fig. 1.5(c).

Contact bouncing happens when the switch is closed. The contact bouncing can affect the lifetime of the switch [37, 42, 43]. Different actuator and biasing waveform were proposed to eliminate bouncing phenomenon [44, 45]. The bouncing phenomenon was investigated using an AFM-based test-setup and a nano-indenter based test-setup [46]. The two methods aimed to actuate a MEMS switch at a well-controlled low velocity to observe the force interaction at nano-scale. The experiments show that surface force leads to multiple bounces when the contact-gap is in the range of nano-meters. The bouncing phenomenon is shown to be a product of competition between the restoring force of the MEMS cantilever beam and adhesion force. The Casimir force, which comes from vacuum fluctuations due to quantified field between two parallel plates separated by a short distance, was only the dominant force in the last few nanometers and second order effect. The adhesion force was believed to include capillary force, Van Der Waals forces and hydrogen bonding [40].

Frictional polymer contamination is observed in both MEMS switch and traditional switch [37, 38]. Polymers are easily formed in platinum group metal contact and any other catalytically active metal [37]. Thin film polymers form around metal contact over the time and act as an insulating film. The contact resistance will increase. The film deposits on the contact materials when there is organic vapor around the micro-contact. During the fabrication of the switch, polymer layer is often used as sacrificial layer [18]. The frictional polymer can be found after fabrication [38]. By using a process without polymer sacrificial layer and less catalytically active metal as contact material, frictional polymer problem was resolved [47].

When the switch is actuated repeatedly without applying RF signal, the condition is called "cold switching". When the switch is cold-switched, fretting and pitting can happen on the contact surface. Fretting is a time-related and acceler-

ated contact resistance degradation process due to the accumulation of wear debris and oxides in the contact area [37]. The wear debris and oxides are caused by small oscillatory movements at the interface of contacting metals. By increasing the contact force, the contact resistance can drop. However, after large amount of wear debris and oxide form, the contact resistance cannot be dropped by applying more contact force.

Pitting is caused by repeated actuating a switch. The repeated actuation cause a confined damage spot on the contact material. The spot is irregularly shaped and with corrosion products [37]. The contact resistance at the spot increases, leading high temperature when current passes through. The high temperature will cause material transfer between top and bottom electrode.

Stiction between top and bottom contact electrode directly causes RF-MEMS switch failure. The switch will remain ON state no matter biased or not. The stiction problem is caused by capillary, electrostatic, chemical and Van Der Waals forces [40]. The primary cause of stiction is capillary force. The surface of the metal contact becomes hydrophilic in ambient air. Water vapor across the switch gap will generate attractive capillary force. The capillary force can be avoided by using low-energy surface coating to form a hydrophobic contact surface layer [48]. The problem can also be avoided by packing the switch in inert gases [18]. Top electrode design can also address stiction problem in low sprint constant RF-MEMS switches in which the restoring force is small [49].

The mechanical structure of RF-MEMS switch will be under prolonged mechanical stress after actuation. The plastic deformation will cause relaxation of the mechanical structure, which is called creep. The permanent deformation of the mechanical structure will lead to changes in actuation voltage or permanent switch failure. Creep does not normally happens in crystalline brittle solids, such as silicon. However, in RF-MEMS switch, the beam structure is usually made of high-conductivity metals, like aluminum, gold, or copper. Creep behavior is observed in those materials [50]. The creep problem can be solved by using creep-

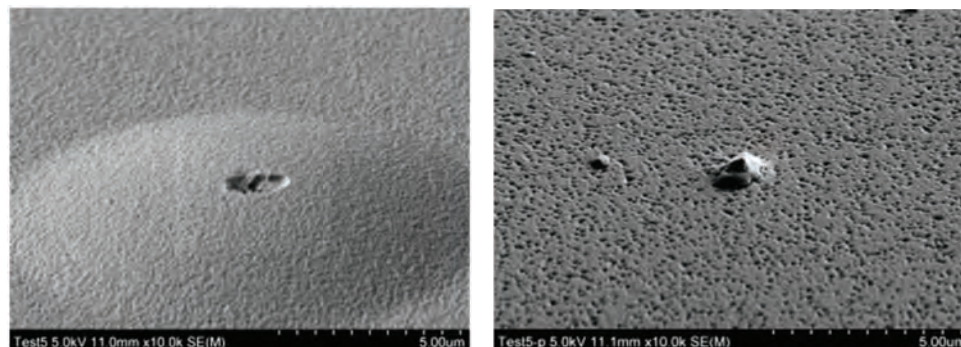


Figure 1.6. Material transfer phenomenon under hot-switching voltage. ©2016 IOPScience. Reprinted, with permission, from [26].

resistant materials [51].

When the switch is actuated repeatedly with applying RF signal, the condition is called "hot-switching". Hot-switching causes other damage mechanisms. The damage mechanisms will be discussed in detail in following section.

1.3 Hot-switching Damage of RF-MEMS Metal Contact Switch

Hot-switching can dramatically shorten the life-time of RF-MEMS switch. For example, the Radant MEMS switch can be cycled up to 1.5 trillion times [23], and the Sandia MEMS switch was cycled up to 10 billion times [47], both characterized under cold-switching condition. However, under hot-switching conditions, in which switches are turned on and off while the RF power is kept on, the reliability of these switches degrades quickly with a sharp increase in contact resistance and insertion loss after a few tens of thousands of cycles. For applications where hot-switching is needed [52], improving the hot-switching reliability of RF-MEMS switches has been a significant challenge for improve the reliability of RF-MEMS switches.

The reliability problems associated with hot-switching are described in [41, 53–55]. The common damage mechanisms include (1) material transfer through soften/adhesion/cold-welding in low voltage hot-switching; (2) material transfer after melting in high voltage hot-switching; (3) Field emission; (4) Field evapora-

tion; (5) Electro-migration; (6) Thomson effect; (7) Arc Discharge. Fig. 1.6 shows the SEM picture of material transfer under 3.5 V hot switching voltage [26].

Material transfer through soften/adhesion/cold-welding happens when the hot-switching power is low. In this case, the heating, melting and softening of the contact spot due to the switching power leads to contact adhesion. When opening the contact, the adhesion breaks. Material may transfer to the top electrode from bottom electrode, or the other way around. In high voltage hot-switching, significant contact melting can happen [54]. The melting can cause contact adhesion. Additional material transfer can happen when opening the contact.

During the hot-switching cycle, the gap between the top and bottom electrode can be very small. The electric field will become strong. Under strong electric field, both field emission and field evaporation can happen. Field emission is the emission of electrons induced by the strong electric field. The induced electrons will bombard the other contact surface. The material on the other surface will be transferred. The bombardment will also cause irregularity on the other surface. The current level of the emission electrons is in the range of μA [56] just before the switch contacts closed. If contact contamination exists, the field emission can happen at larger contact separation due to that the effective work function of the surface is lowered by the contaminations [56].

Field evaporation occurs when top and bottom electrodes have small separations and atoms tunnel from one surface to another [57, 58]. The induced transient heat can also cause contact degradation. The field evaporation was observed in RF-MEMS switches in hot-switching cycles as a damage mechanism [53].

Electro-migration is another mechanism that causes material transfer. The voltage potential drop between top and bottom electrode can generate large electrostatic force. The force can move the atoms on the contact metal directly to the other contact metal. Also, the collision of electrons with the atoms can cause transfer of energy. The electro-migration is a polarity dependent mechanism that happens particularly in small effective contact area. The phenomenon has been

observed in different contact materials [59].

The Thomson effect is another reason of material transfer. During separation of the contacts a molten bridge is formed. The bridge has a thermal gradient. The direction of the thermal gradient depends on the Thomson coefficient. The Thomson effect shifts the hottest point to one end of the bridge. When the bridge breaks during switching, the rupture will happen on the hottest point. This process will add more material to the contact surface of the cooler end of the bridge [26].

Arcing discharge happens when a current flow through an insulating gaseous medium. The insulating gaseous medium become conductive only when the electric field is high enough to ionize the medium. The arcing discharge happens in a RF-MEMS switch when it is not package in vacuum condition and the local electric field is high during hot-switching condition. The discharge can happen both during either contact opening or closing [60]. Molten metal droplets and metallic vapor are formed and deposited on the contact surface during discharge, causing material transfer. Discharge is difficult to be ignite in the ultrahigh vacuum condition [61]. However, when the switch is not package in vacuum or the electric field is high, discharge may be ignited and leads to damage on electrode [62].

Several methods to improve the hot-switching reliability of RF-MEMS switches have been reported. One way is to use dissimilar contact materials (Au/Ru) rather than (Au/Au). Dissimilar contact materials will have less material transfer between each other than between the same material. The switch can be cycled up to 100 million cycles under 100 mW [63]. Another design uses a ball grid array (BGA) dimple design [64]. The contact dimple has a ball shape, and high electric fields that could cause arcing only happen near the tip of the contact dimple. Because of the high packing density, the BGA design could suppress the arcing-induced contact failure with field screening as well as the local mechanical deformation of each dimple. The fabricated switch can be cycled up to 100 million cycles under 1 W.

The primary purpose of this dissertation is to address hot-switching damage

problem in RF MEMS metal contact switch. Two methods are presented to improve the reliability of RF MEMS switches under hot-switching condition. Novel cantilever designs are proposed to integrate the methods in a compact way. The chapters layout as following:

Chapter 2 largely reprints the paper "Extension of the Hot-Switching Reliability of RF-MEMS Switches Using a Series Contact Protection Technique" published on IEEE Transactions on Microwave Theory and Techniques, which the dissertation author is the first author of the paper. In this chapter, series protection technique is discussed and experimentally verified. A novel mechanical design is proposed.

Chapter 3 largely reprints the paper "High-Power High-Isolation RF-MEMS Switches with Enhanced Hot-switching Reliability Using A Shunt Protection Technique" submitted to IEEE Transactions on Microwave Theory and Techniques, at the time of writing this thesis, which the dissertation author is the first author of the paper. In this chapter, shunt protection technique is discussed and experimentally verified, which the dissertation author is the first author of the paper.

Chapter 4 largely reprints the paper "Single-actuator shunt-series RF-MEMS switch" published on 2014 IEEE MTT-S International Microwave Symposium (IMS), which the dissertation author is the first author of the paper. In this chapter, a novel mechanical design is proposed to realize shunt-series contacts in a very compact way.

Appendix A documents the detailed fabrication steps used to fabricate the RF-MEMS switch in CNM2 cleanroom facilities at UC Davis.

Chapter 2

Extension of the Hot-Switching Reliability of RF-MEMS Switches Using A Series Contact Protection Technique

2.1 Introduction

In this chapter, a methodology for drastic improvement of RF-MEMS switches' hot-switching reliability was demonstrated. In particular, by employing a protective contact in parallel with a series RF-MEMS switch, the hot-switching lifetime can be extended by more than two orders of magnitude while maintaining excellent RF performance. Theoretical analysis of the performance and design trade-offs of the proposed hot-switching reliability improvement methodology for RF-MEMS switches are also shown. A novel mechanical design is introduced that allows the correct protection actuation sequence to be realized using a single actuator. A robust copper sacrificial layer process was also introduced to ensure the reliability and yield of the switch fabrication. The fabrication process will be discussed.

2.2 Device concept

Fig. 2.1 and Fig. 2.2 shows the proposed switch design and its working principles. Fig. 2.1 (b) shows the top view of the switch, and Fig. 2.1 (c) shows the side view of the switch. The movable part of the switch is a rectangular-shaped cantilever beam

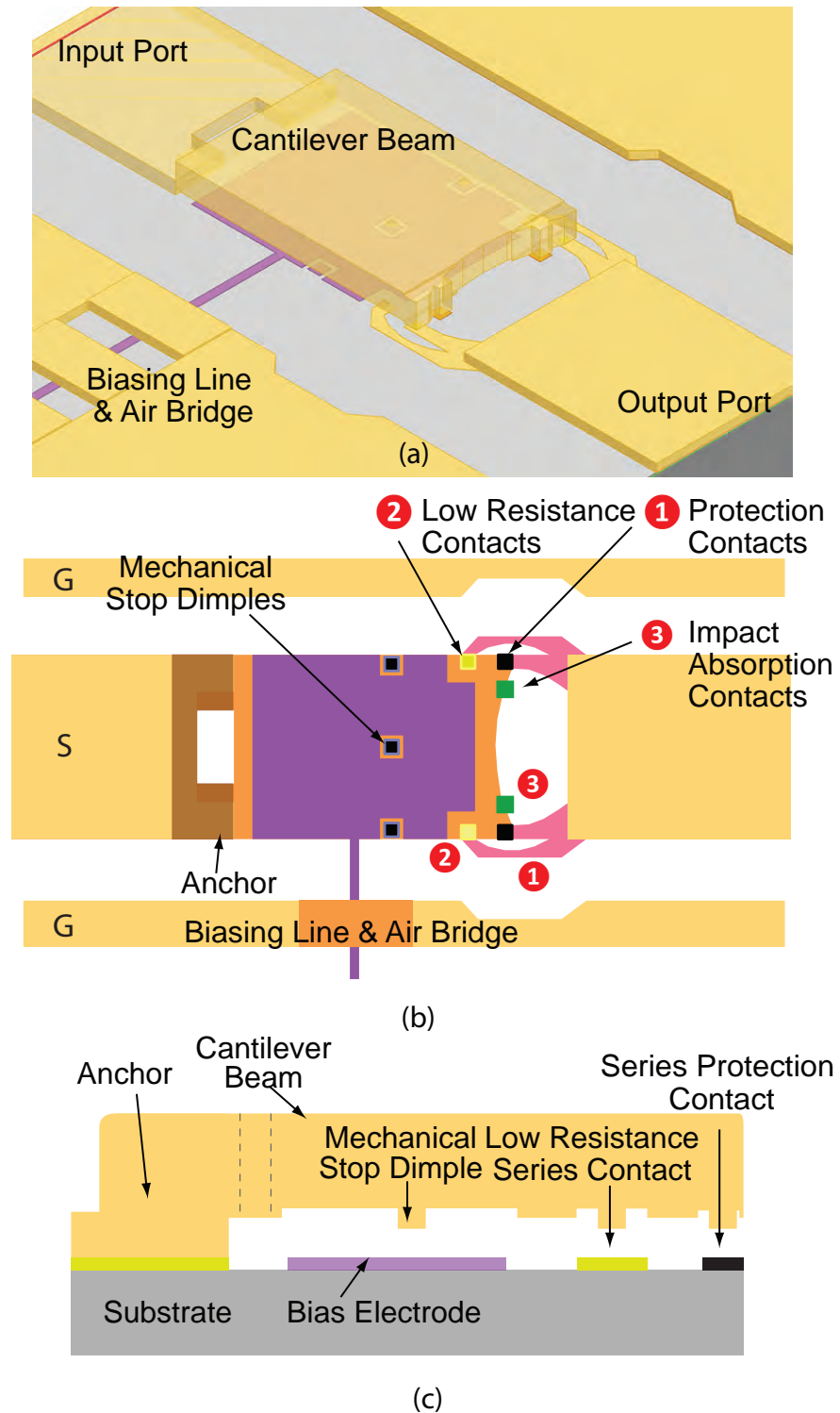


Figure 2.1. Concept of RF-MEMS switch with series protection contact : (a) 3-D view; (b) Top view; (c) Profile view;

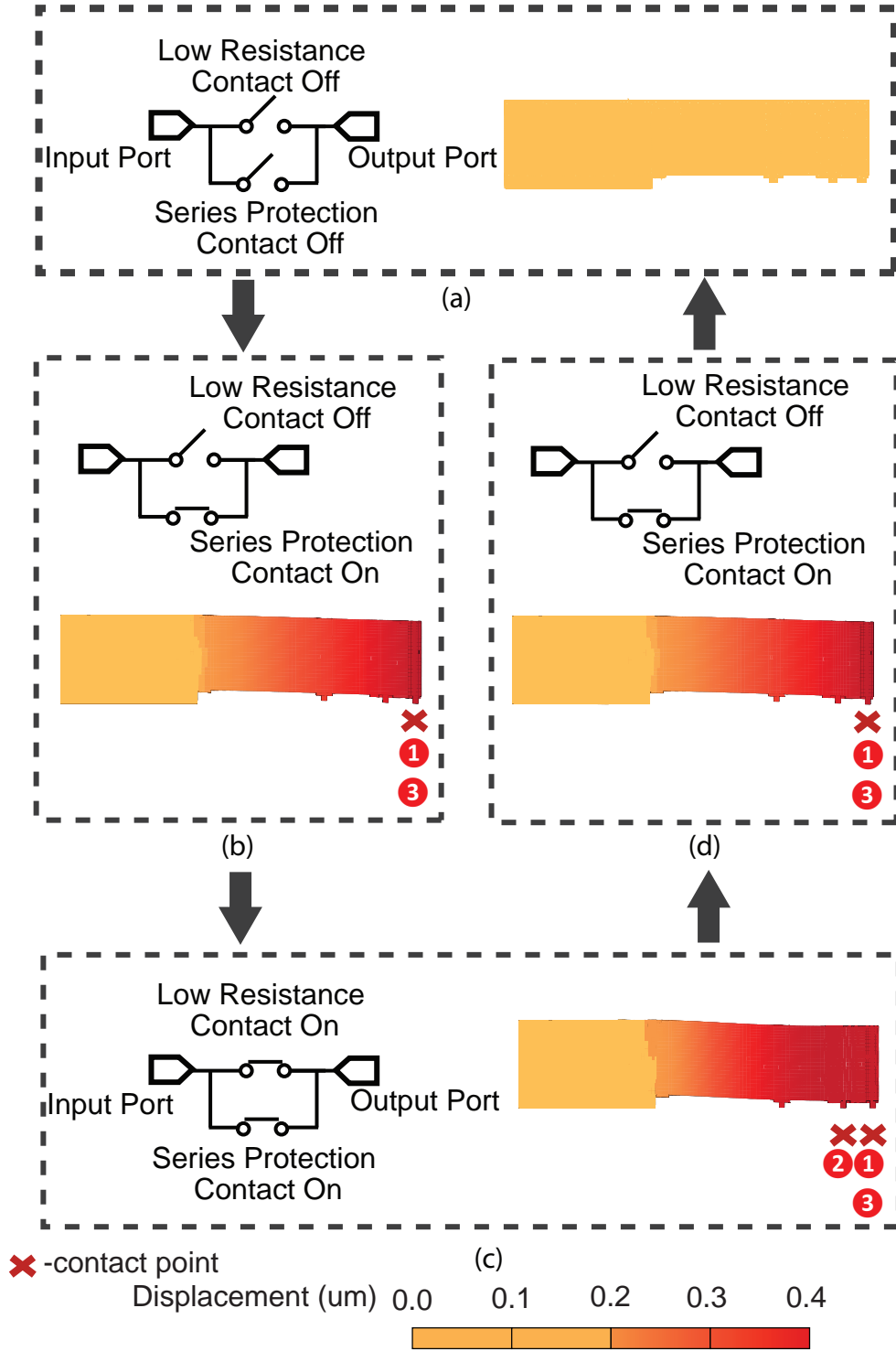


Figure 2.2. Switching sequence of the device: (a) Off-state; (b) Transition-state from off-state to on-state; (c) On-state; (d) Transition-state from on-state to off-state.

placed in series between the input and output signal lines. There are three groups of contact dimples towards the tip of the cantilever. The first group of contacts (labeled number 1) are placed at the very tips of the cantilever and serves as protection contacts that will be degraded during hot-switching events. The second group of contacts (labeled number 2), which are placed a distance away from the tip of the cantilever, provide low series on-state resistance. Both group 1 and 2 connect the input and output signal lines. The third group of contacts (labeled number 3) provide additional mechanical impact absorption and are not connected to the signal lines. In addition, three mechanical stopper contacts are placed in the middle of the biasing electrode only to prevent catastrophic contact between the cantilever and the electrode as there is no dielectric on top of the biasing electrode to prevent charging issues. These stopper contacts are not normally touched during switching cycles. The contact force will be concentrated on the conducting contacts to achieve lower contact resistance.

2.2.1 OFF-state to ON-state

In one switching cycle, the switch is initially in the off-state [Fig. 2.2 (a)]. As the bias voltage increases, the switch will close the protection contacts ① and impact absorption contacts ③ first [Fig. 2.2 (b)]. At this stage, most of RF power will pass through the protection contacts ① and the voltage difference between the low-resistance contacts ② and the output signal line is significantly lower than that in the case of no protection.

To see the protection mechanism quantitatively, the equivalent circuit modeling of the switch is used. Fig. 2.3 (a) shows the equivalent circuit of a series contact switch *without protection*. Before contact is made, the switch can be modeled as a series connected capacitor whose capacitance C_s is dependent on the overlap area A and separation d between the tip of the cantilever and the opposing RF electrode. To simplify the model, the series inductance and parasitic (mostly fringing-field) capacitance are omitted. We also assume that the contact dimple area is far less than A and contribute little to C_s .

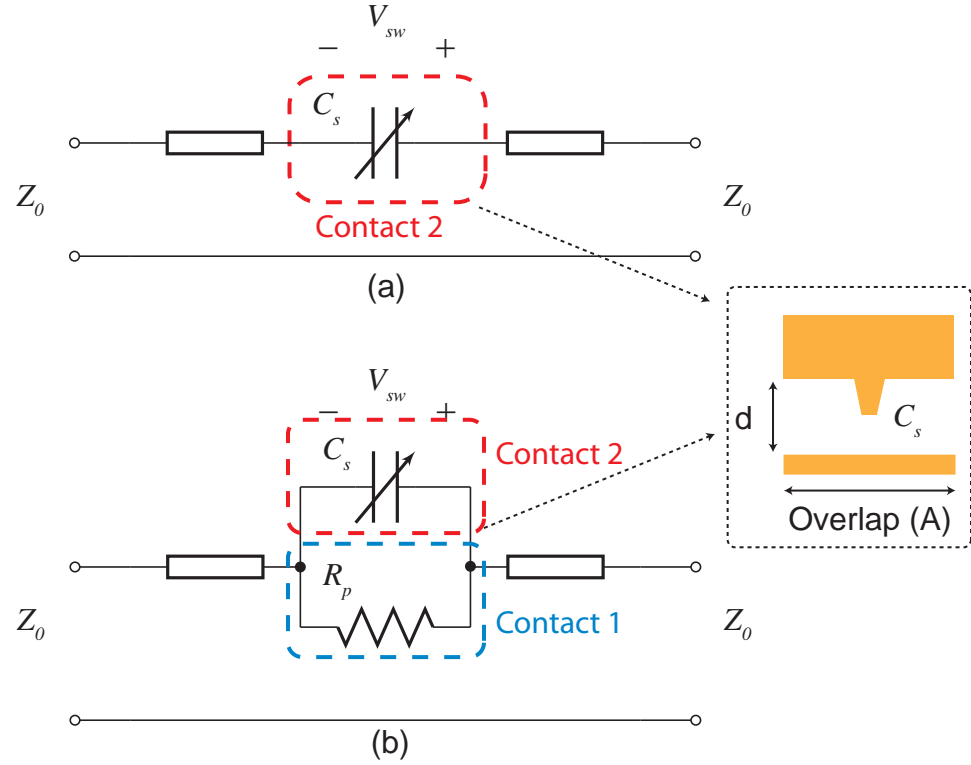


Figure 2.3. Equivalent circuit model of switches (a) without protection and (b) with protection.

The S-parameters for Fig. 2.3 (a) are

$$S_{11} = S_{22} = \frac{1}{1 + 2j\omega Z_0 C_s}, \quad (2.1)$$

$$S_{12} = S_{21} = \frac{2j\omega Z_0 C_s}{1 + 2j\omega Z_0 C_s}, \quad (2.2)$$

where ω is the angular frequency of the RF signal, and Z_0 is the characteristic impedance of the transmission line.

The voltage across the switch contacts with an input power of P is

$$V_{sw} = V_1^- + V_1^+ - V_2^- = (S_{11} + 1 - S_{12})V_1^+, \quad (2.3)$$

where $V_1^+ = \sqrt{2PZ_0}$ is the amplitude of the incident wave (from the input port), V_1^- the amplitude of the reflected wave, V_2^- the amplitude of the transmitted wave, and P is the input power.

Therefore, the voltage $V_{sw,u}$ across the unprotected switch is

$$V_{sw,u} = \sqrt{\frac{8PZ_0}{4Z_0^2\omega^2C_v^2 + 1}}. \quad (2.4)$$

The electric field intensity will be:

$$E_{sw} = \frac{V_{sw,u}}{d} = \sqrt{\frac{8PZ_0}{4Z_0^2\omega^2\epsilon_0^2A^2 + d^2}}. \quad (2.5)$$

Fig. 2.3 (b) shows the equivalent circuit of the *protected* switch with the protection contacts which are modeled as a resistor R_p in parallel with the switch capacitance C_s . The contact resistance is assumed to be constant even though the resistance will drop as the biasing voltage increases. Following the same procedure as in (2.1)–(2.5), the voltage across the *protected* switch contact is calculated.

$$V_{sw,p} = \sqrt{\frac{8PZ_0}{4Z_0^2\omega^2C_s^2 + \left(\frac{2Z_0}{R_p} + 1\right)^2}}. \quad (2.6)$$

The electric field intensity will be:

$$E_{sw} = \frac{V_{sw}}{d} = \sqrt{\frac{8PZ_0}{4Z_0^2\omega^2\epsilon_0^2A^2 + d^2 \left(\frac{2Z_0}{R_p} + 1\right)^2}}. \quad (2.7)$$

To evaluate the difference between (2.5) and (2.7), actual device dimensions (Section 2.3.1) are used to illustrate the model. The area A is $56.25 \mu\text{m}^2$ and d varies from $0.9 \mu\text{m}$ to $0.5 \mu\text{m}$ when contact is made between the dimples.

Fig 2.4 illustrates the modeled electric field intensity between contacts ② with respect to d under 1 W input power and various R_p values. The unprotected switch has the highest electric field intensity of $39.9 \text{ V}/\mu\text{m}$. The switch with 2Ω R_p has the lowest electric field intensity of $0.78 \text{ V}/\mu\text{m}$, representing a more than 50 times reduction in electric field intensity and making the switch much less prone to hot-switching damages. The electric field intensity tends to go up as the R_p increases so it is preferable to achieve a low R_p . In essence, a local cold switching condition is created by shorting the low-resistance contacts out with the protection contacts.

During the lifetime of the switch, the protection contacts ① will be degraded by hot-switching and R_p will increase and gradually provide less protection for the contacts ①. However, even if R_p increases to $50\ \Omega$ the electric field intensity would still be only one fourth of that of the unprotected switch (Fig.2.4 (a)). Therefore, in practice, failure mechanisms like stiction may occur long before the protection contacts lose their efficiency.

Fig. 2.5 compares the electric field across the low-resistance contacts ② with [Fig. 2.5-(b)] and without [Fig. 2.5-(a)] the protection contacts. The calculations show that even for a relatively large protection contact resistance of $50\ \Omega$, the electric field across the low-resistance at 10 W RF power is at the same level as that of an unprotected contacts at 1 W.

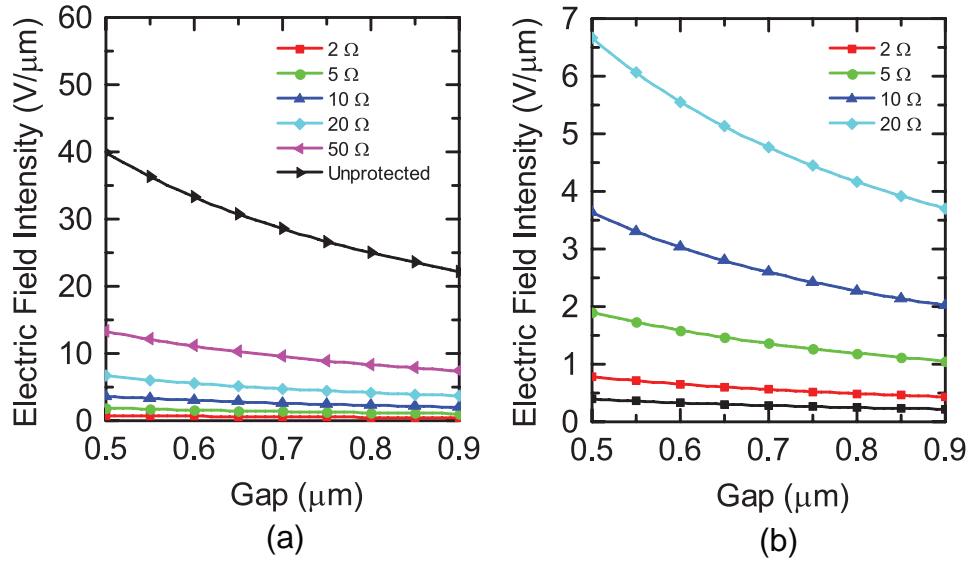


Figure 2.4. (a) Calculated electric field intensity of unprotected switch and switches with different protection contact resistances (at RF frequency of 2.4 GHz). (b) Zoom-in view of (a) for low protection contact resistance.

As the biasing voltage increases, the low-resistance contacts are closed. The switch transitions to the on-state. RF power will be distributed between contacts ① and ②. However, contacts ② are designed to have low resistance so that most of the RF power will pass through them, achieving low insertion loss.

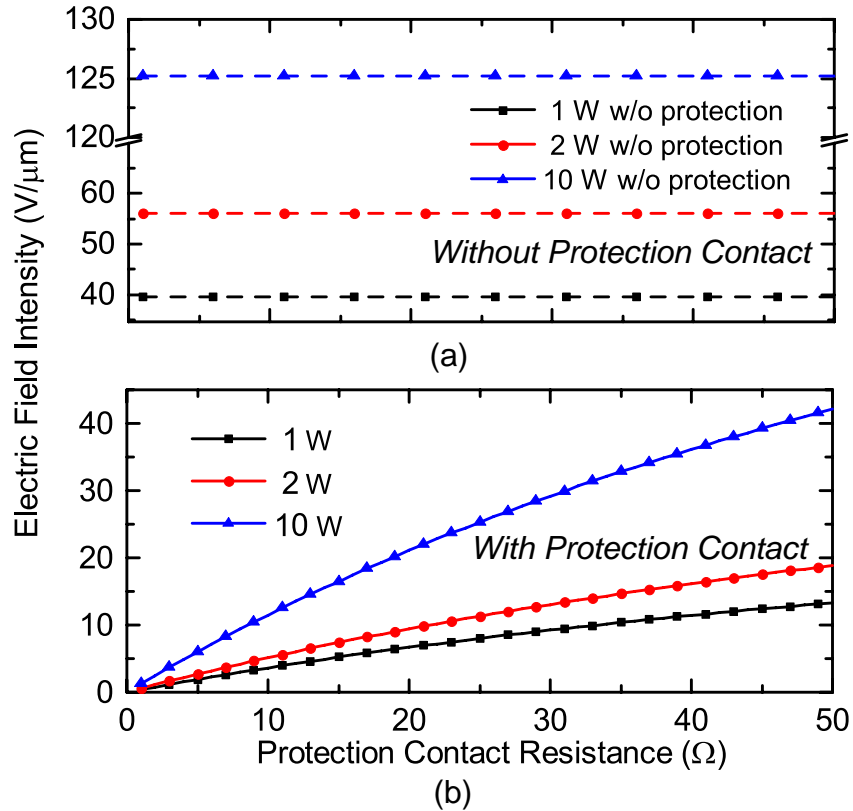


Figure 2.5. (a) Calculated electric field intensity under different input power levels without the protection contacts at 2.4 GHz at the closest gap ($0.5\ \mu\text{m}$); (b) Calculated electric field intensity under various input power levels with the protection contacts at 2.4 GHz at the closest gap ($0.5\ \mu\text{m}$) with respect to different protection contact resistances.

2.2.2 ON-state to OFF-state

When toggling from the on-state to off-state, the low resistance contacts will still be protected from high, and potentially damaging, electric fields. When reducing the electrostatic bias, the beam will release in a way that will allow the low resistance contacts to detach before the high resistance/protective contacts. This results in safely transferring the RF power to the protection contacts, thereby allowing the low resistance contacts to open in a nearly cold-switch condition. In the on-state the cantilever is largely bent, so the restoring force is relatively high to prevent contact adhesion. As the biasing voltage further decreases, the protection contacts will detach and the switch will transition to the off-state. The electric field change

Table 2.1. Geometry parameters of the switch

Geometry parameter	Symbol	Value (μm)
CPW line width	w_s	100
CPW line gap	w_g	60
Beam width	w_b	100
Dimple width	w_d	2.5
Contact width	w_c	7.5
Air bridge width	w_a	20
Beam length	l_b	150
Electrode length	l_e	120
Air bridge length	l_a	60
Protection and low-resistance contact separation	l_{s1}	20
Stopper and low-resistance contact separation	l_{s2}	40
Beam thickness	t_b	5
Dimple thickness	t_d	0.5
Biasing electrode thickness	t_e	0.15
Cantilever to electrode gap	g_0	0.9
Dimple to contact gap	g_1	0.4

of the connecting line of the low-resistance contacts. The separation between the low-resistance contacts and the series protection contacts is chosen such that the actuation voltages of the two types of contacts are largely different. In this case the protection contacts will have enough time to settle and protect the low-resistance contacts. There is a trade-off, however, between the difference of the actuation voltages and the restoring force of the protection contacts. We will discuss the trade-off in the mechanical analysis section. There is no biasing electrode

from series protection contacts to low-resistance contacts. This configuration will distribute more contact force on low-resistance contacts to achieve lower contact resistance at on-state. Finally, to facilitate dc biasing of the switch and to reduce undesired RF leakage, air bridges are formed to allow the biasing line to pass through the ground plane.

2.3.2 Mechanical Design and Simulation

The cantilever beam of the switch can be analyzed using the Euler-Bernoulli beam equation [65]

$$\frac{M}{EI} = -\frac{d^2v}{dx^2}, \quad (2.8)$$

$$I = \frac{w_b t_b^3}{12}, \quad (2.9)$$

where $E = 79$ GPa is Young's Modulus of gold, I is the moment of inertia of the beam, and v is the deflection of the beam in z direction. The biasing electrode puts an even load on part of the beam. The load distribution (N/m) q can be expressed as [18]

$$q = \frac{\epsilon_0 w_b V_a^2}{g_0^2}, \quad (2.10)$$

where ϵ_0 is the vacuum permittivity, V_a is the applied bias voltage, and g_0 is the gap between the beam and the electrode.

In the following analysis, it is assumed that the load distribution q is constant across the cantilever neglecting the bending of the cantilever to get a simplified analytical solution of the beam profile. This assumption is valid when the biasing electrode is relatively far away from the cantilever and the change in the gap between the cantilever and the biasing electrode is small.

Before the protection contacts close, the boundary conditions are

$$\begin{aligned}
 v(x)|_{x=0} &= 0, \\
 \frac{dv(x)}{dx} \Big|_{x=0} &= 0, \\
 v(x)|_{x=l_e-} &= v(x)|_{x=l_e+}, \\
 \frac{dv(x)}{dx} \Big|_{x=l_e-} &= \frac{dv(x)}{dx} \Big|_{x=l_e+}.
 \end{aligned}$$

The displacement of the beam can then be calculated as:

$$v(x) = \begin{cases} \frac{qx^2}{24EI} (6l_e^2 - 4l_e x + x^2), & 0 < x \leq l_e \\ \frac{ql_e^3}{24EI} (4x - l_e). & l_e \leq x \leq l_b \end{cases} \quad (2.11)$$

When the protection contacts close, an additional boundary condition applies:

$$v(x)|_{x=l_b} = g_1. \quad (2.12)$$

In this case, the displacement can be solved as:

$$v(x) = \begin{cases} \frac{qx^2}{24EI} \left(6l_e^2 - 4l_e x + x^2 - \frac{12F_1 l_b}{q} + \frac{4F_1 x}{q} \right), & 0 < x \leq l_e \\ \frac{1}{24EI} (4F_1 x^3 - 12F_1 l_b x^2 + 4ql_e^3 x - ql_e^4). & l_e \leq x \leq l_b \end{cases} \quad (2.13)$$

We can also express the contact force F_1 on the protection contacts as:

$$F_1 = \frac{4ql_e^3 l_b - ql_e^4 - 24EI g_1}{8l_b^3}. \quad (2.14)$$

When the low-resistance contact is closed, the following boundary condition is applied

$$v(x)|_{x=l_e} = g_1. \quad (2.15)$$

The contact forces on both protection contacts F_1 and low-resistance contacts F_2 can be written as

$$F_1 = \frac{A_2 A_5 - A_4 A_3}{A_2^2 - A_1 A_3}, \quad (2.16)$$

$$F_2 = \frac{A_2 A_4 - A_1 A_5}{A_2^2 - A_1 A_3}, \quad (2.17)$$

where

$$A_1 = -8l_b^3,$$

$$A_2 = 4l_e^3 - 12l_b l_e^2,$$

$$A_3 = -8l_e^3,$$

$$A_4 = 24EIg_1 - 4ql_e^3 l_b + ql_e^4,$$

$$A_5 = 24EIg_1 - 3ql_e^4.$$

The displacement in this region can be calculated as:

$$v(x) = \begin{cases} \frac{1}{24EI} (6ql_e^2 x^2 - 4ql_e x^3 + qx^4 \\ \quad - 12F_2 l_e x^2 + 4F_2 x^3 \\ \quad - 12F_1 l_b x^2 + 4F_1 x^3), & 0 < x \leq l_e; \\ \frac{1}{24EI} (4F_1 x^3 - 12F_1 l_b x^2 + 4ql_e^3 x \\ \quad - 12F_2 l_e^2 x + 4F_2 l_e^3 - ql_e^4), & l_e \leq x \leq l_b. \end{cases} \quad (2.18)$$

The calculated beam profile is plotted in Fig 2.7. The geometry parameters used in the calculations are the same as used in switch design. By increasing the voltage, the beam is bent making contacts sequentially. The actuation voltage for the first contact is 29.5 V and for the second contact is 74.9 V.

The contact sequence can also be understood from the contact forces (Fig. 2.8). Because there is no biasing electrode between contacts ① and ②, the contact force is concentrated on the contacts ② to achieve lower contact resistance. It can be seen Fig. 2.8 that the protection contacts experience the largest contact force just

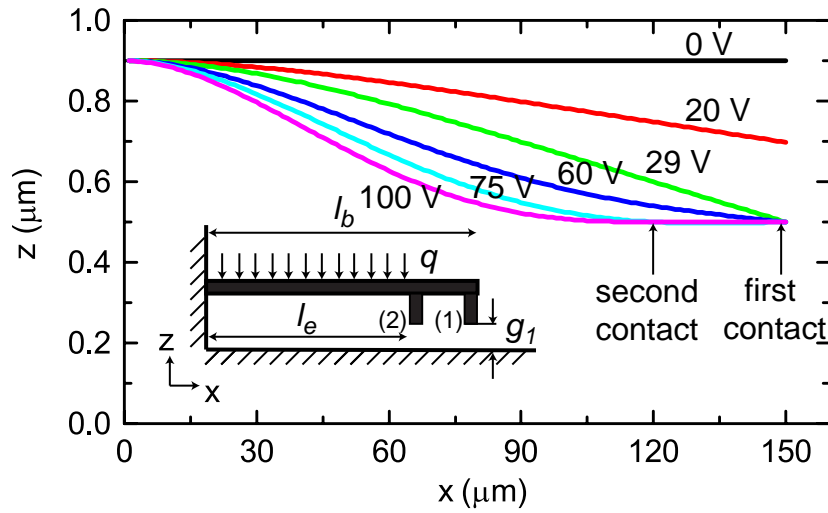


Figure 2.7. Beam profile predicted by theoretical model under different biasing voltages.

before the low-resistance contacts close when the actuation voltage increases, the contact force on the protection contacts gradually decreases and is transferred to the low-resistance contacts. If the bias voltage further increases, the protection contacts will detach leaving the low-resistance contacts as the only contacts for the switch. This will give a way to open the protection contact to recover the switch from stiction on the protection contacts.

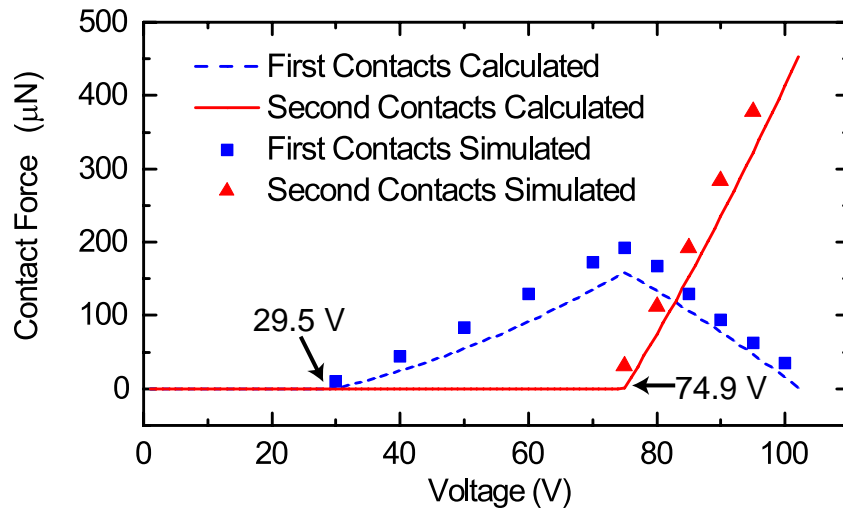


Figure 2.8. Calculated and simulated contact force under different biasing voltages.

When qualitatively designing the switch actuator, the protection contact dimple always will be positioned closest to the free end of the cantilever (please refer to Fig. 2.1(b) and (c)). The low resistance contact will always be offset further back from the cantilever free end, in the direction of the anchor. In this configuration, the protection contacts will always close first. The restoring force on the protection contact is dependent on distance between the protection contact to low-resistance contact by

$$F_r = \frac{24EIg_1}{3l_e^3 + 4l_e^3x_d} \quad (2.19)$$

where x_d is the distance from the protection contacts to the low-resistance contacts. Fig. 2.9 shows restoring forces for different protection contact positions. The restoring force is the highest when the protection contact are placed next to the low-resistance contacts and the force decreases as the distance increases. High restoring force can counteract stiction, but the time interval between forming protection contacts and forming low-resistance contacts will be shorter if the two contacts are placed closer to each other. If the protection contacts are not mechanically damped, some settling time is needed before they reach a steady state. If the actuation interval between the protection contacts and the low-resistance contacts is not long enough, the low-resistance contacts may still see high RF power before the protection contacts settle and hot-switching damage is likely to happen on the low-resistance contacts. In this design the protection contacts 30 μm is placed away from the low-resistance contacts.

The induced stress in the MEMS structure also needs to be studied and controlled to ensure reliable operation. Due to viscoelasticity and creep effects the material properties will drift during actuation [66]. This effect will lead to unexpected biasing voltage changes and reduce the reliability of the switch. Since the switch will be operating with a large degree of bending, the induced stress has to be kept minimum. The induced stress at the beam anchor has been minimized with an opening which also serves as a release hole for sacrificial layer removal. Fig.2.10 shows the simulated Von Mises stress for the switch under 90 V actuation

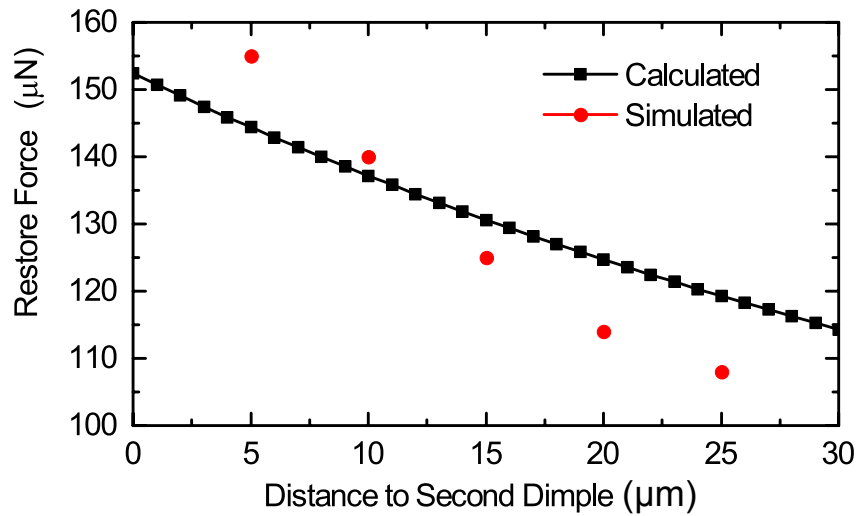


Figure 2.9. Calculated and simulated restoring force of protection contact for different dimple positions.

voltage using the Coventorware [67] FEM solver. The maximum stress is 60 MPa at the switch anchor.

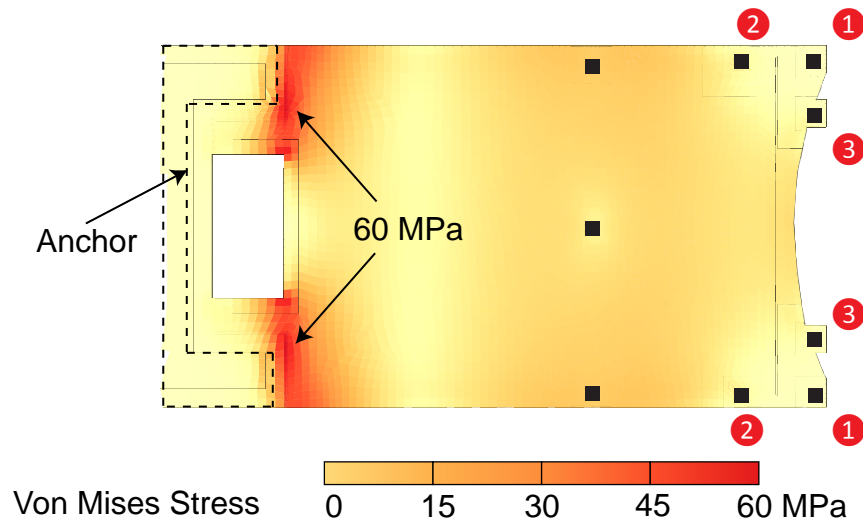


Figure 2.10. Simulated Von Mises Stress under 90 V actuation voltage.

Cantilever based MEMS switches are highly susceptible to stress gradients. Stress gradients can result in undesired beam deflections, which typically leads changes in the actuation voltage (beam bending up) and sometimes a completely unusable device (beam bending in down position and touching the bottom electrode

right after releasing). The axial stress in the beam before release is

$$\sigma = \sigma_0 - \frac{\sigma_1}{t_b/2}z, \quad (2.20)$$

where σ_0 is the average compressive stress in the beam and σ_1 is the stress difference through the thickness of the beam. A linear stress gradient is assumed here. The internal momentum due to stress gradient can be calculated as

$$M_x = \int_{-t_b/2}^{t_b/2} w_b z \sigma dz = -\frac{1}{6} w_b t_b^2 \sigma_1. \quad (2.21)$$

By solving the Euler-Bernoulli beam equation, the beam deflection due to the stress gradient is

$$v(x) = \frac{1}{12} \frac{w_b t_b^2 \sigma_1 x^2}{EI}. \quad (2.22)$$

Then, the total beam deflection is

$$v(x) = \begin{cases} \frac{qx^2}{24EI} (6l_e^2 - 4l_e x + x^2) + \frac{1}{12} \frac{w_b t_b^2 \sigma_1 x^2}{EI}, & 0 < x \leq l_e; \\ \frac{ql_e^3}{24EI} (4x - l_e) + \frac{1}{12} \frac{w_b t_b^2 \sigma_1 x^2}{EI}, & l_e \leq x \leq l_b. \end{cases} \quad (2.23)$$

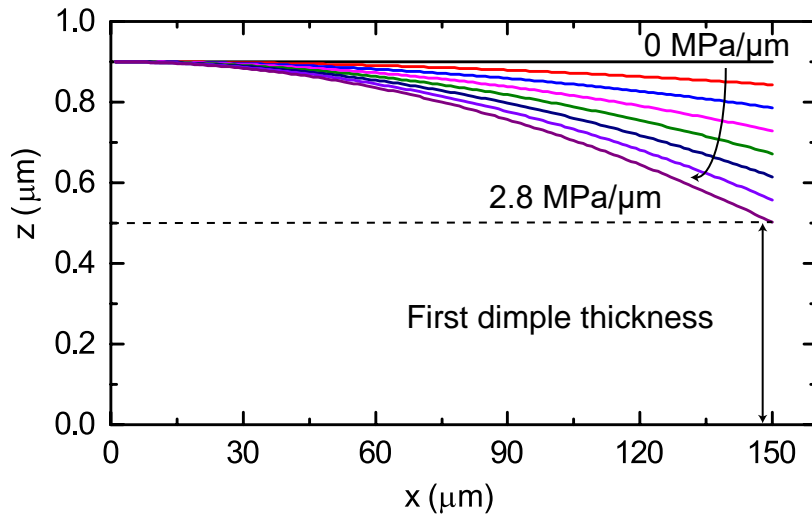


Figure 2.11. Beam deflection due to positive stress gradient.

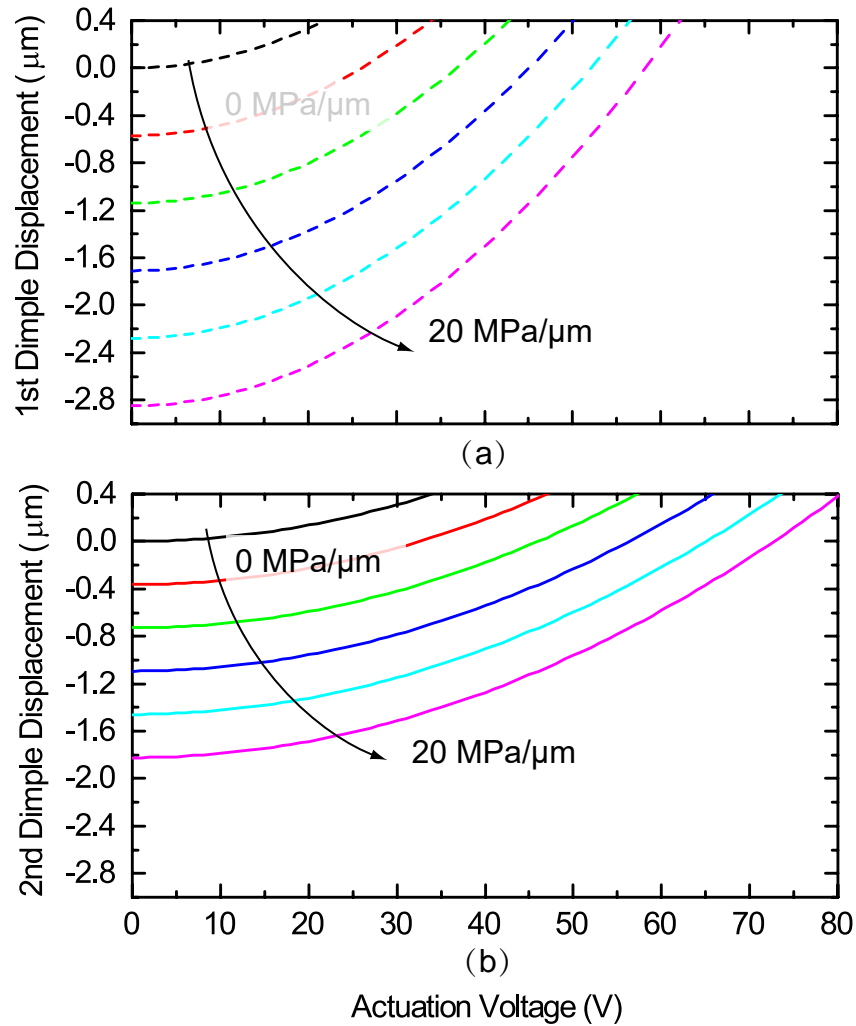


Figure 2.12. First (a) and second (b) contact dimple movement under different actuation voltage with different negative stress gradient.

Fig. 2.11 shows the deflection due to positive stress gradient when there is no biasing voltage. The first contact dimple will touch the bottom electrode when the stress gradient is larger than $2.8 \text{ MPa}/\mu\text{m}$. The switch will be constant ON, leading to a permanent device failure. Fig. 2.12 plots the first and second contact dimple displacement under different actuation voltage with different negative stress gradient. With negative stress gradient, the beam will bend up and the first contact dimple will always have larger displacement upward than the second contact dimple. However, when the actuation is applied the first contact dimple will always travel $0.4 \mu\text{m}$ to make contact with the bottom electrode first. The

sequence that the protection contact will close first can be achieved even with a negative stress gradient up to 20 MPa/ μm . In our fabrication process the stress gradient was kept low and the beam is an intrinsic layer of plated gold. As shown in Fig. 2.16(b)(right), the gap between the tip of the cantilever beam and the bottom electrode is almost exactly 900 nm as designed, which means the stress gradient of the beam is low. Neither permanent ON nor change of actuation sequence was observed in the experiment.

2.3.3 EM Analysis

The RF performance of the switch geometry is analyzed and optimized in Ansys HFSS [68] (Fig. 2.13). The isolation is 23 dB at 6 GHz in the off-stage. Because the protection contacts introduce additional overlap area between the cantilever and the bottom RF electrodes, the isolation performance is compromised for hot-switching protection. The insertion loss of the switch is 1.31 dB at 6 GHz when only the protection contacts are closed and is lowered to 0.04 dB when the low-resistance contacts are closed. To demonstrate the RF power redistribution, Fig. 2.14 compares the simulated current distributions of the two stages. It is clear that the current is concentrated on the protection contacts in the protection stage and transfers to the low-resistance contacts when they close.

2.4 Device Fabrication

Fig. 2.15 shows the fabrication process for the switch, modified from [69]. The switch is fabricated on a high resistivity ($\sim 10 \text{ k}\Omega\text{-cm}$) oxidized silicon substrate. A 150 nm thick high resistance ($\sim 1 \text{ k}\Omega/\square$) silicon chrome (SiCr) dc bias line is first patterned by lift-off [Fig. 2.15 (a)]. Next, a second lift-off is used to pattern the 150 nm thick bottom gold (Au) contacts with a titanium (Ti) adhesion layer [Fig. 2.15 (b)]. The protection contacts are patterned using a lift-off process. The 100 nm thick protection contacts are made of platinum (Pt) with Ti as the adhesion layer [Fig. 2.15 (c)]. A 400 nm thick copper (Cu) sacrificial layer with chromium (Cr) as the adhesion metal is sputtered and patterned with a liftoff

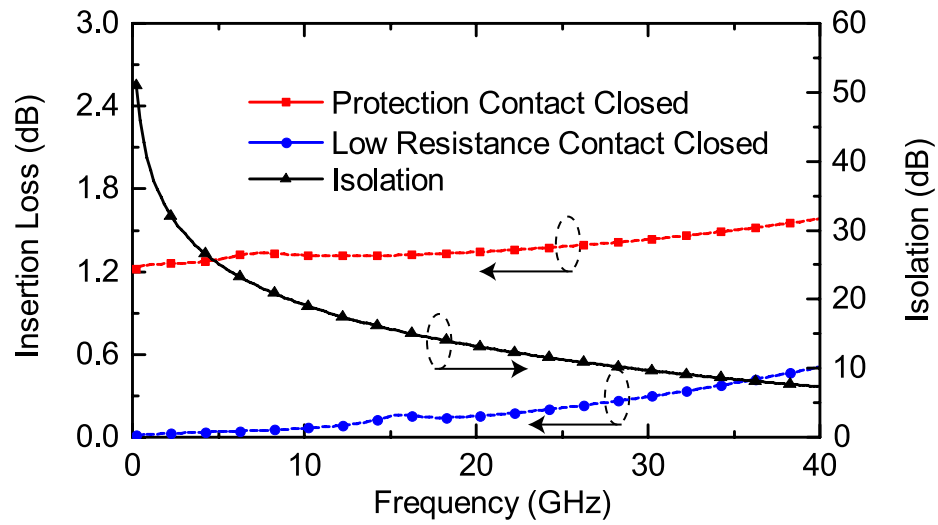


Figure 2.13. Simulated insertion loss and isolation for different switching stages.

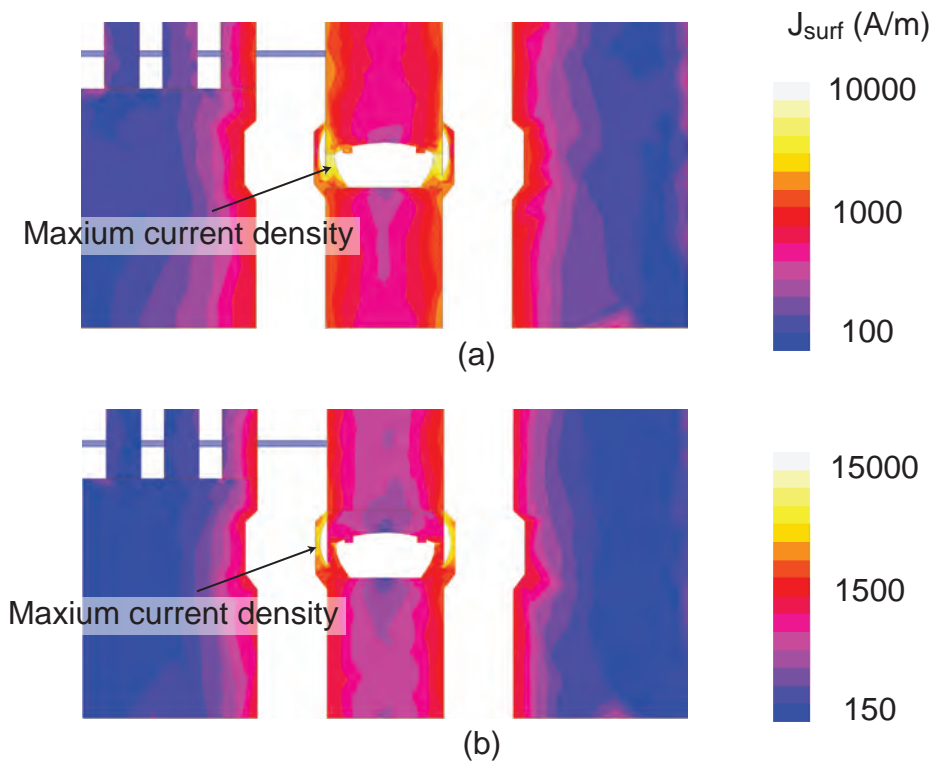


Figure 2.14. Simulated surface current distribution (a) when the protection contacts are closed, and (b) when the low-resistance contacts are closed.

process [Fig. 2.15(d)]. A second 500 nm thick Cr/Cu sacrificial layer is deposited and patterned to form the cantilever dimple mold [Fig. 2.15 (e)]. A 50/150 nm

Cr/Au is sputtered as the seed layer for the subsequent electroplating. Positive photoresist is spin-coated to 6 μm and patterned to form the electroplating mold for the cantilever. The cantilever is then electroplated to 5 μm thick [Fig. 2.15 (g)]. The contact dimples are also electroplated and formed in gold in this step. The electroplating mold and gold seed layer are removed in their respective dedicated etchants before the devices are released in the chromium etchant and dried in the critical point dryer [Fig. 2.15 (f)]. The chromium etchant is used to etch away all the copper sacrificial layers and chromium adhesion layers at the same time. The Cu sacrificial process avoids using any polymer as the sacrificial layer to minimize potential carbon contamination [38].

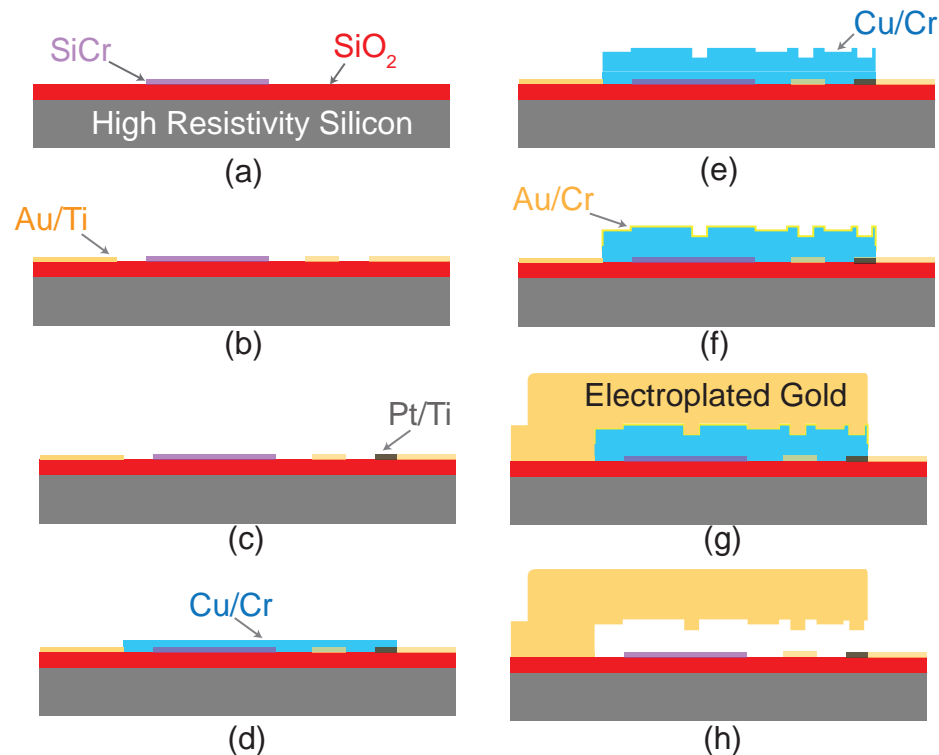


Figure 2.15. Fabrication process of the switch.

Fig. 2.16 shows optical and scanning electron microscopy (SEM) images of the fabricated switch. Fig. 2.16(a) shows images of a protected switch and an unprotected switch used as a control device. The unprotected switch is essentially the same as the protected switch except that the protection contacts are not connected

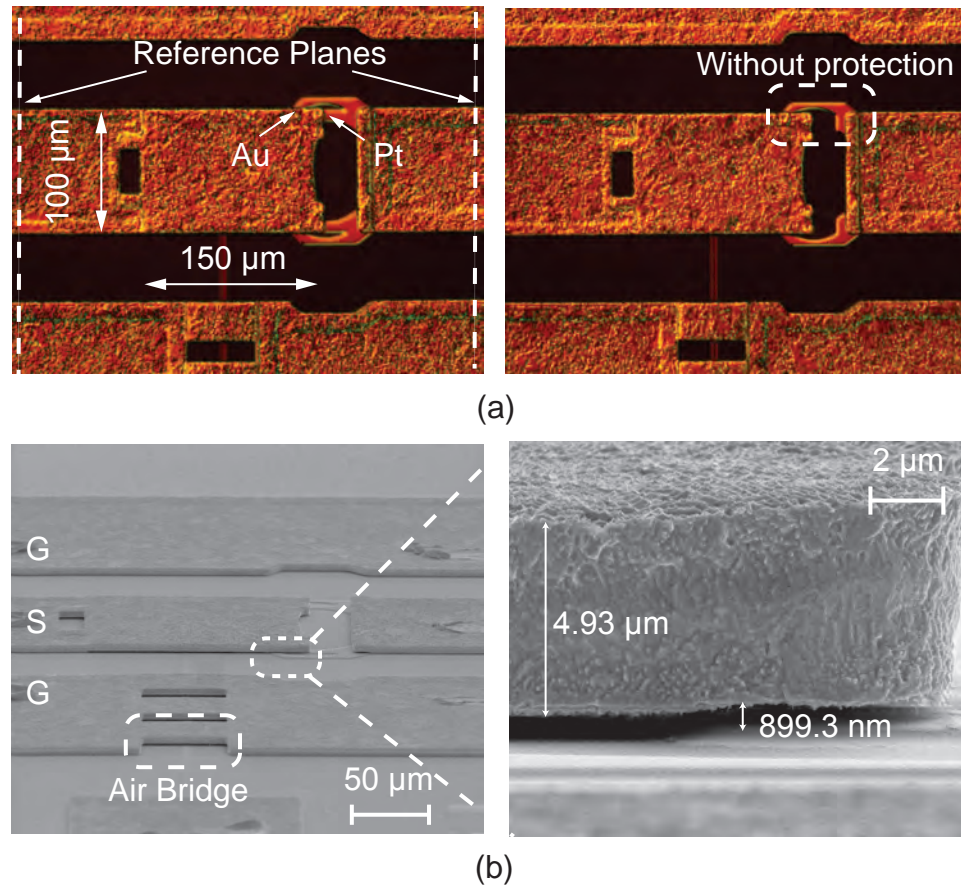


Figure 2.16. (a) Optical images of a pair of protected (left) and unprotected switch (right), (b) Scanning electron microscope (SEM) image of the fabricated switch (left) and zoom-in picture (right).

to the signal line.

2.5 Measurement and discussion

2.5.1 Actuation voltage

The protected switch has two actuation stages. The actuation voltage of one protected switch is measured. The actuation voltage for the protection contacts is 29 V and for the low-resistance contacts is 82 V. This result is in good agreement with the modeling (29.5 V and 74.9 V, respectively).

2.5.2 S-parameters

The small-signal RF performance of the fabricated switches was measured using an HP 8722D network analyzer with Ground-Signal-Ground (GSG) microwave probes. On-wafer Through-Reflection-Line (TRL) standards were used for calibration to the reference planes indicated in Fig. 2.16 (a). One switch with protection contacts and another without protection contacts were measured for comparison.

The S-parameter measurement results are shown in Fig. 2.17. The transition-state data are taken when the protection contacts are closed on the protected switch. The insertion loss is 1.46–2.65 dB in the 0–40 GHz range. The on-state data are taken when the low-resistance contacts are actuated at 90 V. The insertion loss decreases to 0.11–0.62 dB in the 0–40 GHz range. The insertion loss for the unprotected switch, actuated at 90 V, is 0.32–0.74 dB in the 0–40 GHz range. The protected switch has lower insertion loss in general due to additional conducting contacts. The isolation for the protected switch is 36.8–8.1 dB, and for the unprotected is 38–9.6 dB, both measured in the 0–40 GHz range. The protected switch has poorer isolation due to more overlap between actuator and contact electrode because of the additional protection contacts. The measured and simulated isolation has a 3 dB discrepancy due to an unintended expansion of contacts and dimple sizes in the device fabrication.

2.5.3 Linearity

The linearity of the MEMS switch was measured at a center frequency of 2.4 GHz. Fig. 2.18 shows the test setup for the two-tone measurement. The two tones were 25 MHz offset from the center frequency. The input power level varied from 12 dBm to 16 dBm. The spectrum analyzer is set to 20 dB input attenuation to ensure that the nonlinearity of the equipment does not introduce appreciable measurement errors. The third-order inter-modulation intercept point (IIP3) of the device is 64.1 dBm. The IIP3 of a through line was also measured and is 68.3 dBm. The IIP3 is limited by the passive inter-modulation caused by the interface between the probe tips and CPW line and the substrate. The linearity limitation is typically

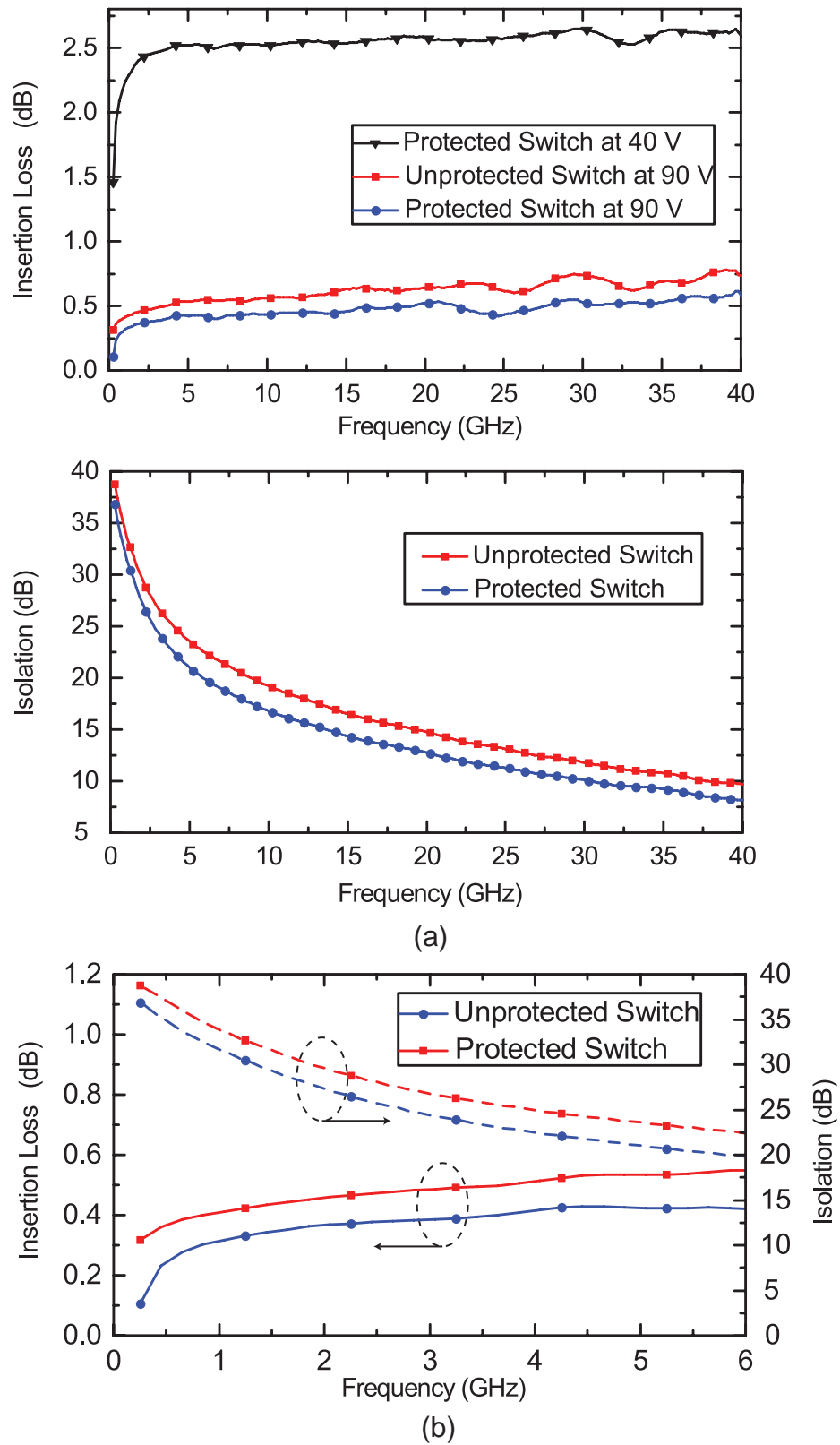
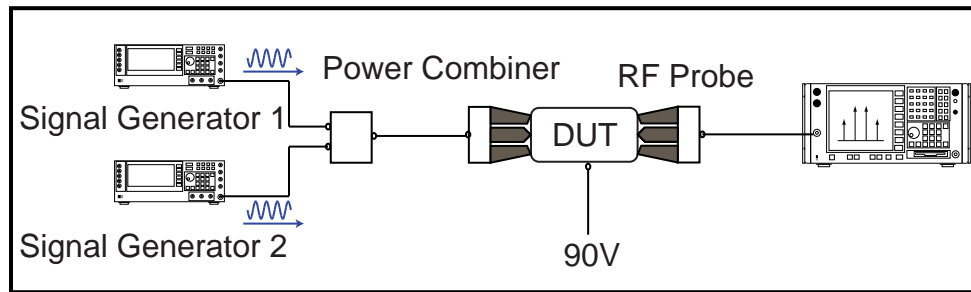
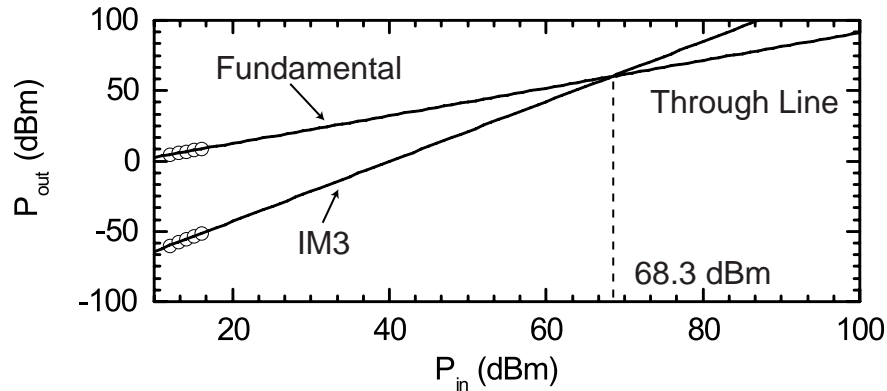


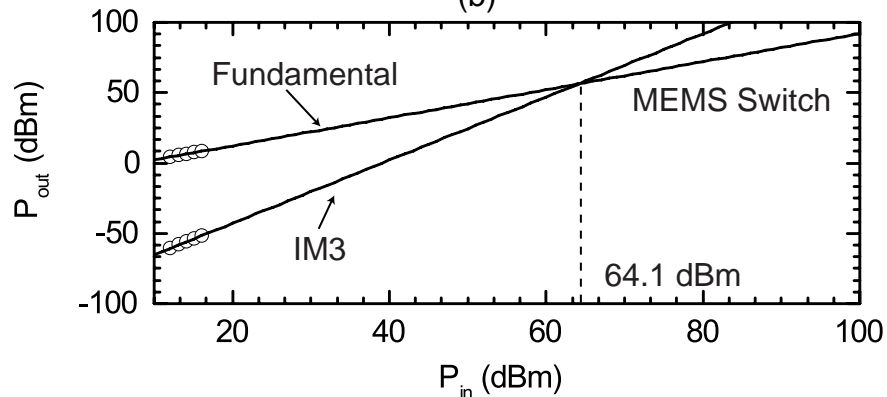
Figure 2.17. (a) Measured S-parameters, (b) Zoom in of (a) from 0 GHz - 6 GHz



(a)



(b)



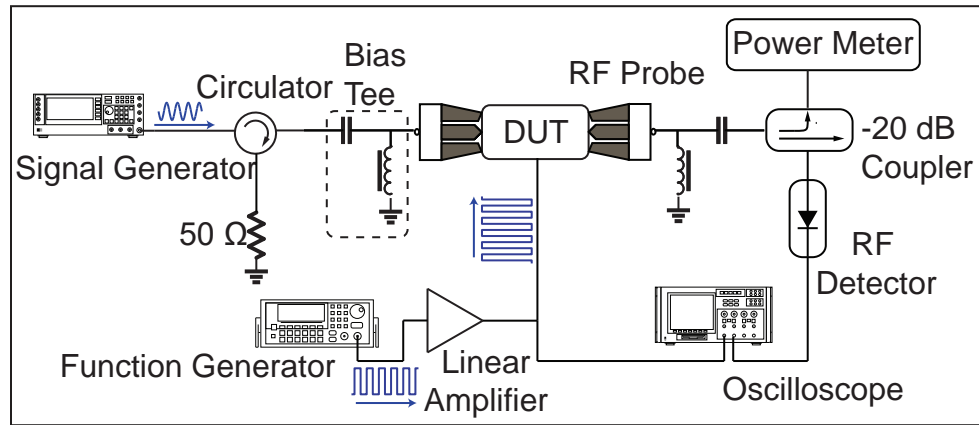
(c)

Figure 2.18. (a) Linearity test setup schematics, and measured IIP3 for both (b) through line and (c) MEMS switch.

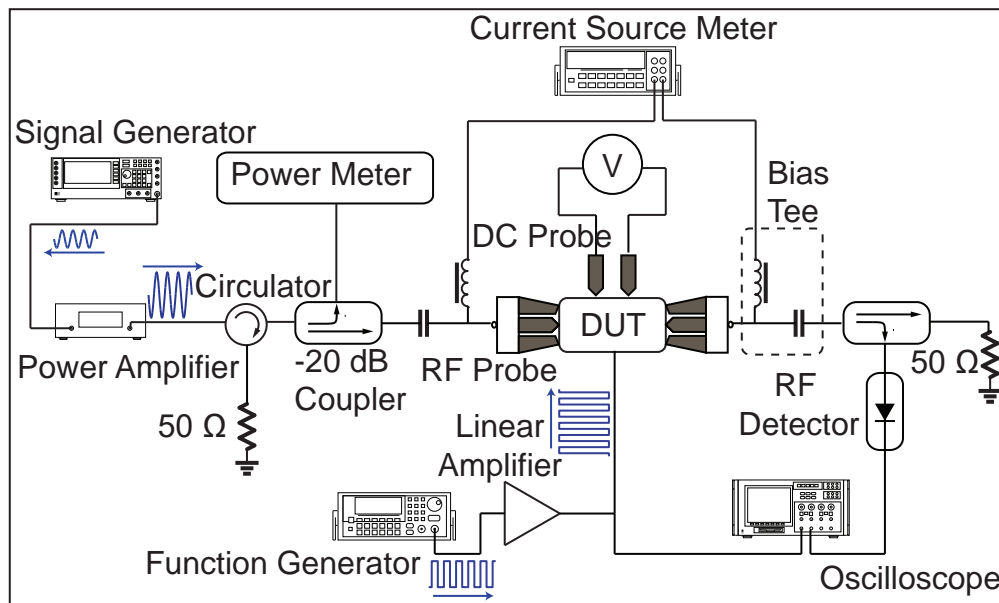
found in probing RF MEMS switches [63].

2.5.4 Switching time

The switching time was measured in order to set up the cycling frequency of the lifetime measurements. The test setup [Fig. 2.19(a)] consists of an RF signal generator, a circulator to block the reflected power, a function generator to generate



(a)



(b)

Figure 2.19. (a) Test setup schematics for switching time measurement, (b) test setup schematics for hot-switching lifetime characterization.

the actuation waveform, a linear amplifier to amplify the waveform, an RF detector to convert the RF signal to dc signal, and an oscilloscope to capture the detected waveforms. When the switch is opened, the RF power is reflected and circulated to the $50\ \Omega$ load. Once the switch is closed, the RF power passes through the switch and is converted to dc voltage by the RF detector. The actuation waveform and detected waveform are compared in the oscilloscope to determine the switching time. The RF signal was set to 5 dBm at 2.4 GHz. A square waveform of 500

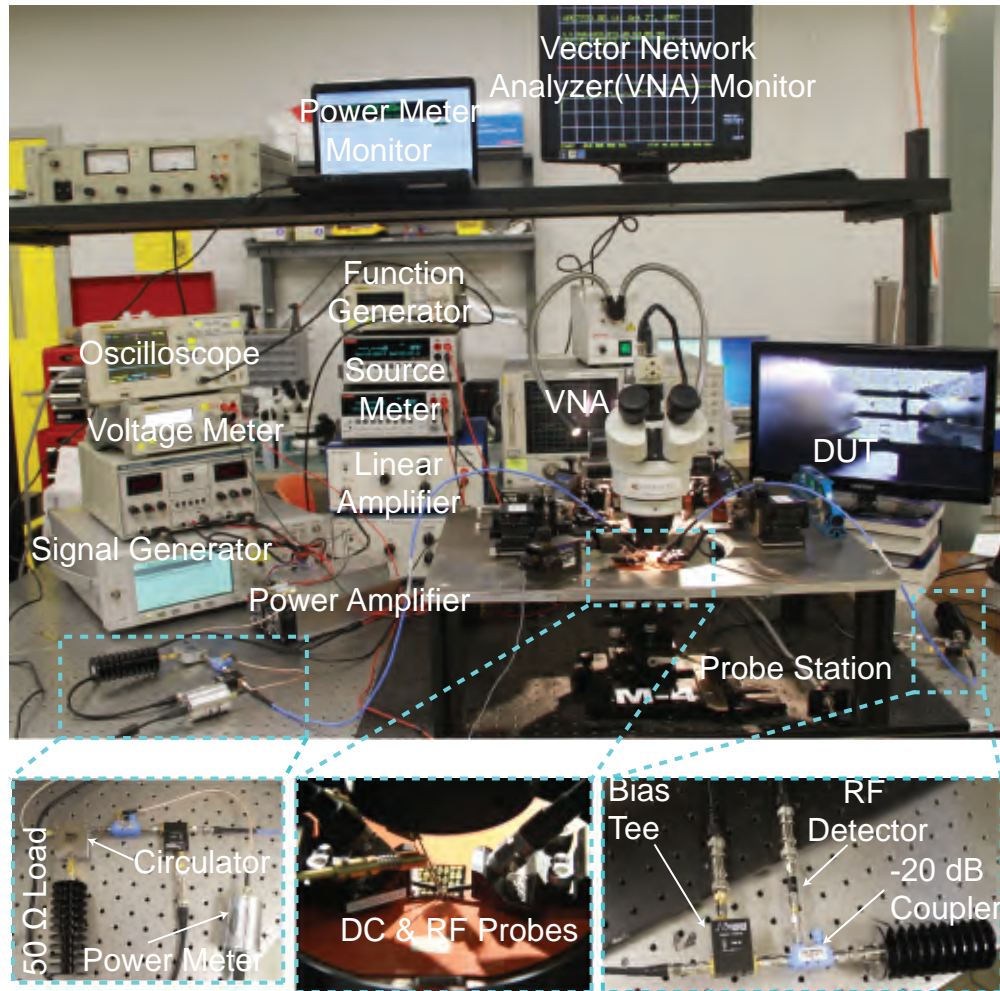


Figure 2.20. Test bench photo for S-parameters, switching time and reliability measurement.

Hz, 5V peak to peak voltage, with a 20% duty cycle is supplied by the function generator. The waveform was amplified 20 times by a linear amplifier.

A protected switch and an unprotected switch were measured in open air lab environment at room temperature. The protected switch has a switch-on time of 45.1 μs and a switch-off time of 17.4 μs [Fig. 2.21 (a&b)]. The unprotected switch has on and off switching time of 49.7 μs and 9.6 μs [Fig. 2.22 (a&b)]. From the waveform, it can be seen that the switch has no bouncing when switching on or off.

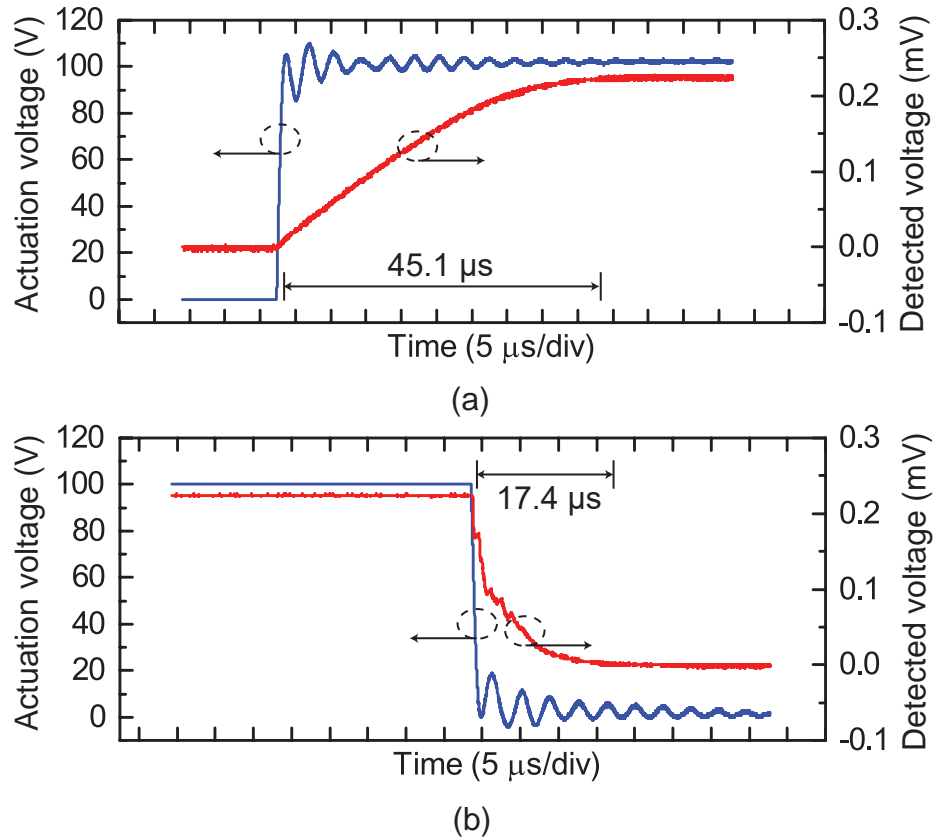


Figure 2.21. (a) Switching-on time of protected switch, (b) switching-off time of protected switch.

2.5.5 Mechanical cycle test

To further isolate the failure mechanisms that are unique to electrical and mechanical phenomena, a switch with no RF power passing through was toggled to 500 million cycles to examine the mechanical impact damage of the dimple to the bottom electrode. A four-point resistance measurement setup was used to measure the change of the contact resistance for both contacts. Fig. 2.23 shows the contact resistance changes over 500 million cycles. The contact resistance remained low up to 200 million cycles ($9.52\ \Omega$ for protection contact and $1.87\ \Omega$ for low-resistance contact) and greatly increased after 500 million cycles ($26.8\ \Omega$ for protection contact and $16.4\ \Omega$ for low-resistance contact). The increase of the contact resistance is due to the impact damage of the dimples on the bottom electrode.

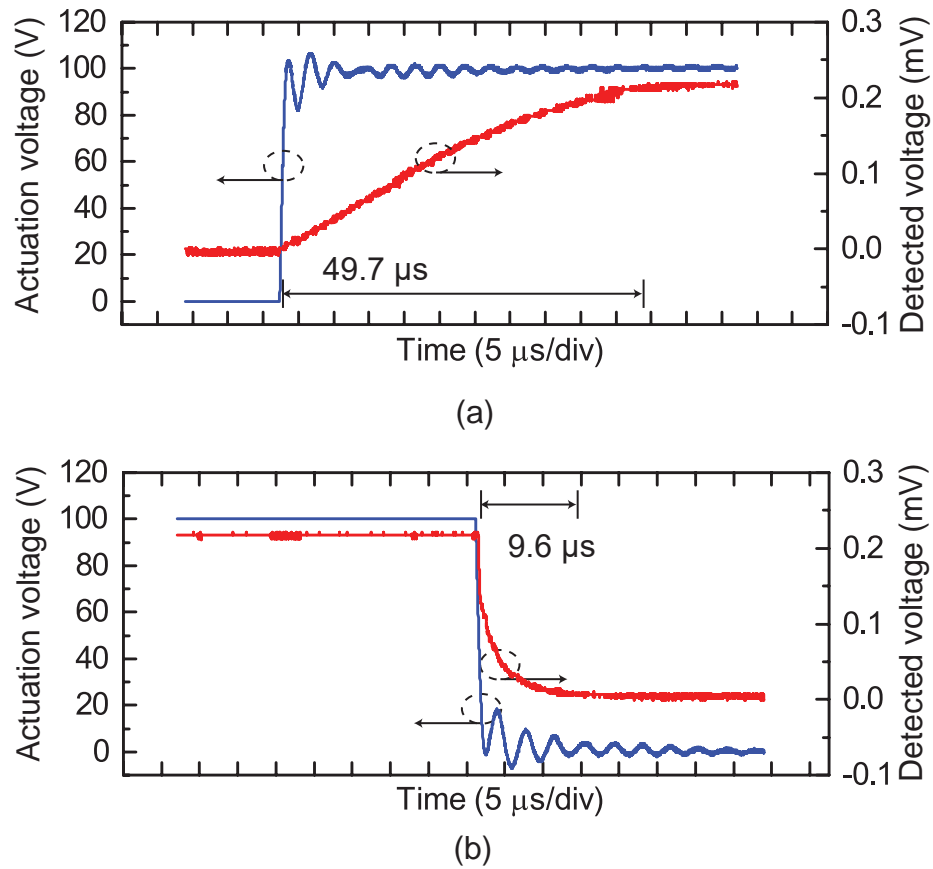


Figure 2.22. (a) Switching-on time of unprotected switch, (b) switching-off time of unprotected switch.

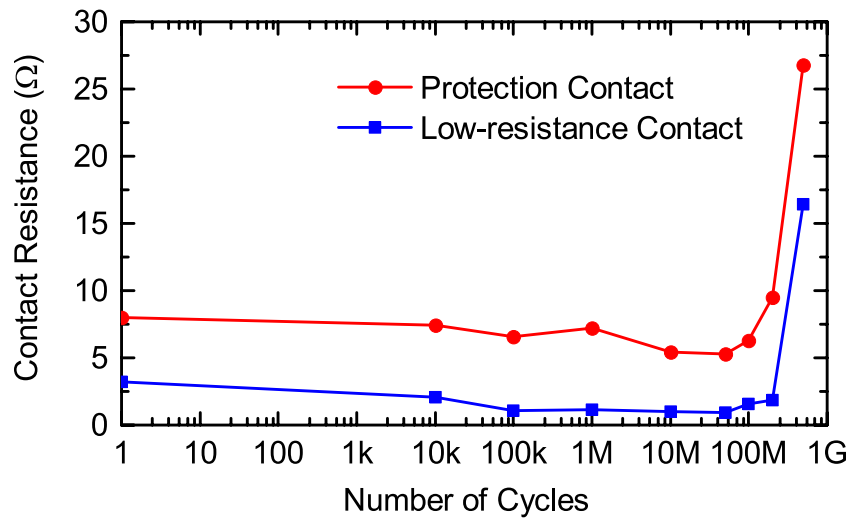
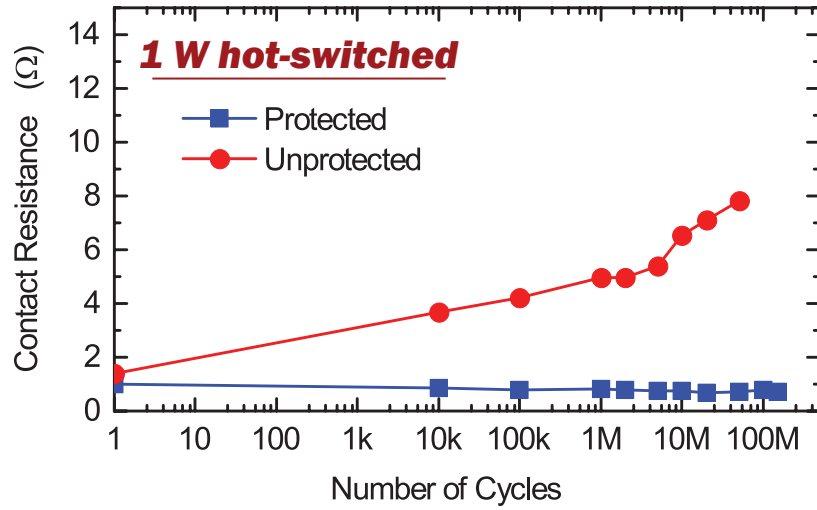


Figure 2.23. Contact resistance changes of the protection contact and low-resistance contact over 500 million mechanical cycles.

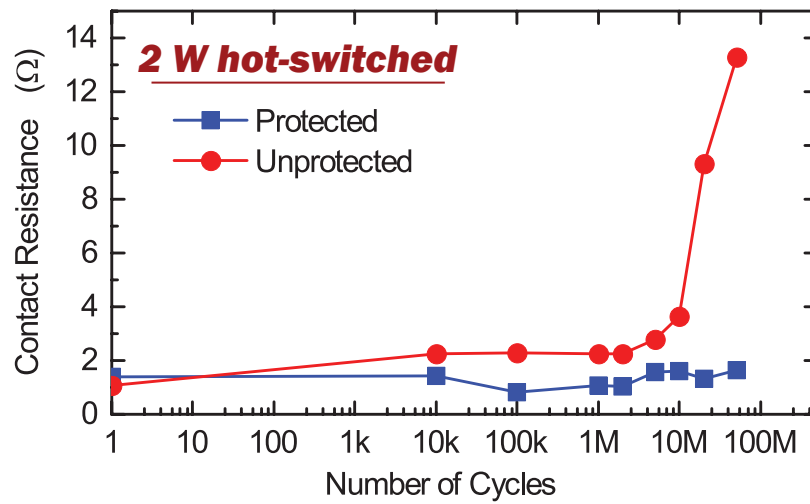
2.5.6 Hot-switching lifetime

The hot-switching lifetime test setup is shown in Fig. 2.19(b). In addition to the switching time test setup, a power amplifier is included to amplify the input RF signal, a power meter is added to monitor the exact power level sent into the switch and a four-point resistance measurement setup is connected through bias-Tee to consistently monitor changes in the contact resistance. The RF frequency used in the cycling test is 2.4 GHz. The RF probes are used as the current source and two additional dc probes are used to measure the voltage drop across the switch. The contact resistance is measured by actuating the switch at 90 V using a dc voltage source (not shown in the figure). The dc probes do not touch the switch during cycling test and only touch the switch when resistance measurement is taken in order to isolate the potential RF signal leak from dc probes. The oscilloscope and the RF detector are used to detect the switching behavior changes. A total of six pairs of protected and unprotected switches are tested. Three pairs are tested under 1 W RF power and the other three 2 W, all under the hot-switching condition. Again, switches are tested under open air lab environment and room temperature conditions. The protected switches can all cycle up to 100 million cycles at 1 W and 50 million cycles under 2 W. Four pairs of protected and unprotected switches were measured continuously at 3 kHz and 50% duty cycle, while the other two pairs were measured at 1 kHz and 50% duty cycle and stopped at different cycle numbers to record the changes in contact resistance. All the contact resistance values were measured by the four-point resistance measurement setup and the current source-meter was set to 5 mA for all resistance measurements. It takes 9 hours and 27 hours to cycle a switch to 100 million cycles at 3 kHz and 1 kHz respectively. Due to time constraint, only two pairs (total four switches) were measured with contact resistance changes recorded.

Fig. 2.24 (a) shows the contact resistance changes under 1 W hot-switching. The resistance of the low-resistance contacts was protected and remained below 1 Ω up to 100 million cycles, whereas that of the unprotected one increased beyond



(a)



(b)

Figure 2.24. (a) Measured contact resistances of switches pair under 1 W of different cycling numbers, (b) contact resistances of switches pair under 2 W of different cycling numbers.

1 Ω after approximately 10,000 cycles. Fig. 2.24(b) shows the contact resistance change under 2 W hot-switching. The same measurement setup was used. The low-resistance contacts on the protected switch remained below 1 Ω up to 50 million cycles, whereas the resistance of the unprotected one increased beyond 1 Ω after approximately 10,000 cycles.

Both of the protected switches failed due to stiction at the protection contacts. The stiction failure was observed between 100 million to 150 million cycles under 1 W and 50 million to 100 million under 2 W. The stiction may be attributed to the local heating and melting of the contact material as the protection contact resistance increased. To alleviate the stiction problem, high contact force and restoring force actuator design can be used [63]. From the calculation in the mechanical design section, the cantilever tip will bend up if the biasing voltage keeps increasing. The bending of the tip can pull the protection dimple away from the bottom electrode. The switch can be actuated under higher biasing voltage to have the protection contact lifted up, in this case the protection contact will not participate in conducting current, leading to less local heating and melting problem and may also alleviate the stiction problem. Table 2.2 compares the lifetime of the proposed switch against recent demonstrations of hot-switching RF-MEMS switches. The switch shows state of the art reliability under hot-switching power of 1 W and great promise for the reliability under hot-switching power beyond 1 W.

2.6 Conclusion

A RF-MEMS switch with series protection contact achieving high reliability under high power, hot-switching condition has been demonstrated. The series protection technique can boost hot-switching lifetime up to 100 times, compared with switches without series protection contacts. To further improve the reliability of the proposed switches, future work includes optimization of the structural design and contact materials.

Table 2.2. Comparison of switch lifetime under hot-switching condition

Design	Frequency Range (GHz)	Switching Power (W)	Cycling number
[63]	0–40	0.1	100 000 000
[64]	0–40	1	100 000 000
[70]	DC	0.1	100 000
[71]	DC	0.25	100 000
[23]	0–40	0.1	1000
This work	0–40	1	100 000 000
This work	0–40	2	50 000 000

Chapter 3

High-Power High-Isolation RF-MEMS Switches with Enhanced Hot-switching Reliability Using A Shunt Protection Technique

3.1 Introduction

In previous chapter, a series protection technique has proposed and experimentally validated to improve the hot-switching reliability by connecting the input port and output port with a secondary protective contact to lower the voltage potential difference before the main contact turns on and off. However, since the protection contact and the main contact are in parallel, the total OFF-state capacitance increases, leading to a decrease in the OFF-state isolation. In this paper, a shunt protection technique is proposed to remedy this shortcoming. Fig. 3.1 and Fig. 3.2 shows the working principle of the shunt protection technique by comparing it with the series protection technique proposed in previous chapter.

The switch goes through three states to transition from the initial state to ON state. Fig. 3.2(a) shows the initial state of the switch when both the shunt protection contact and main contact are open. By closing the shunt protection switch, the device enters the HIGH-ISOLATION state shown in Fig. 3.2(b). In

this state, the switch remains OFF. Because the incoming RF power is shunted to ground by the protection switch, the OFF-state isolation significantly improves. The shunt switch also lowers the RF voltage swing on the main contact, therefore protecting it from hot-switching damage.

In the next step, the device enters the TRANSITION state by closing the main contact [Fig. 3.2(c)]. Both the shunt protection contact and main contact are closed in this state. Then, the shunt switch opens, and the device enters the ON state [Fig. 3.2(d)]. To switch from the ON state to the HIGH-ISOLATION state, the process is reversed, and the main protection contact remains protected.

The effectiveness of the proposed protection scheme stems from the low electric field on the main contact as a result of the short circuit created by the shunt contact. Although the shunt contact will experience hot-switching damage, it can be designed specifically to withstand such damage. For example, the shunt contact may be made from refractory metals that exhibit much higher hardness and therefore better immunity to hot-switching damage. Alternatively, the shunt contact may also be realized as with a solid-state switch using a high-voltage process for even better life-time enhancement.

Compared to the series protection scheme [Fig. 3.1(a)-(c)], the shunt-protection scheme offers improved isolation without significantly affecting the protection effectiveness. The following sections analyze in detail the RF and lifetime performances of the proposed shunt protection scheme.

3.2 Analysis and Design

3.2.1 Comparison Between Shunt Protected Switch and Unprotected Switch (From OFF to ON/ ON to OFF)

The shunt protection contact can significantly lower the electric field intensity on the main contact during hot-switching. Fig. 3.3 shows the equivalent circuit model of an unprotected switch and a switch with shunt protection when the main contacts transit from open to close (or from close to open) (step B1, B4). R_p models

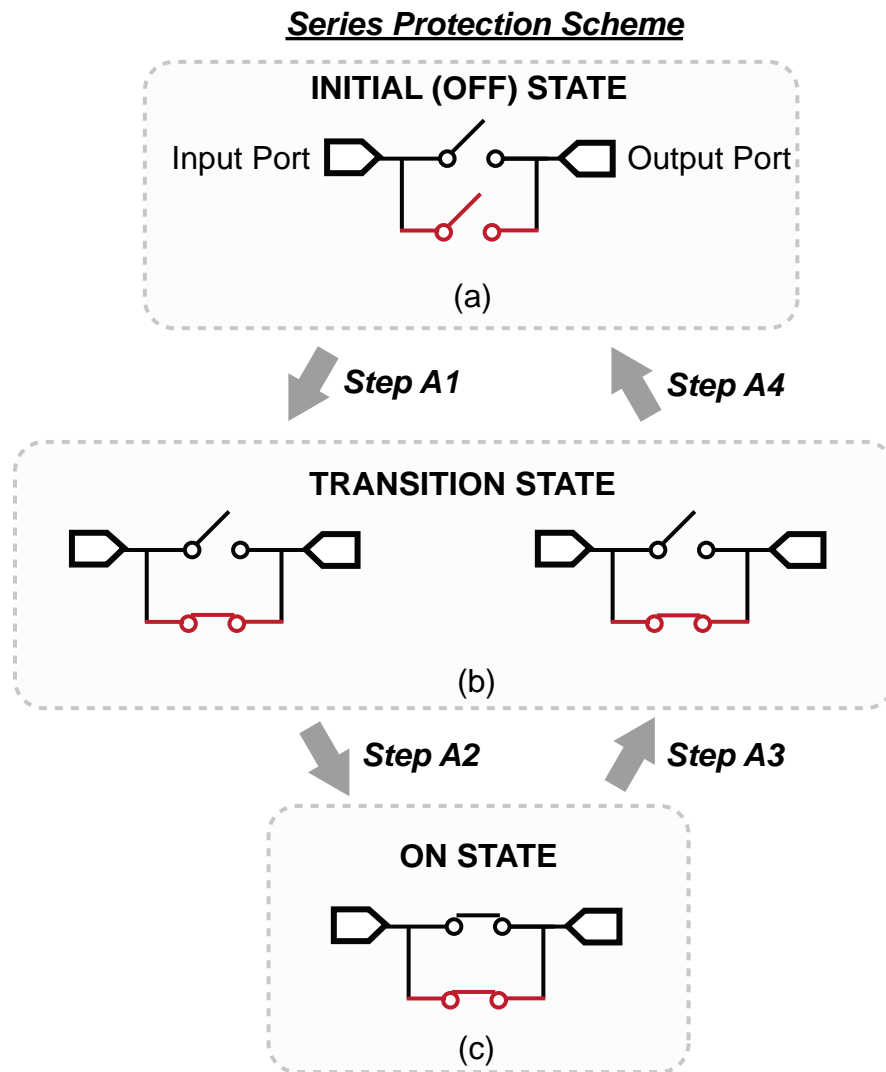


Figure 3.1. Concepts of (a)-(c) series-protection scheme for hot-switching life-time enhancement.

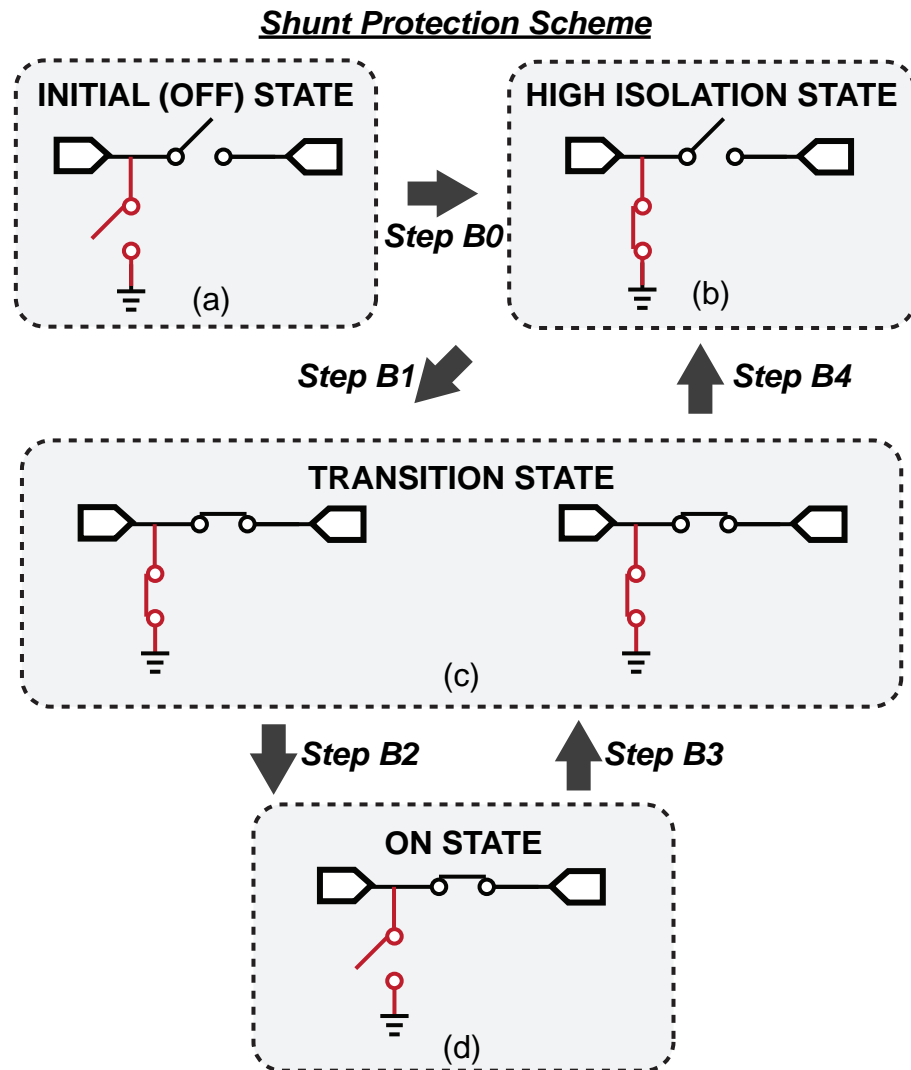


Figure 3.2. Concepts of (a)-(c) the proposed shunt-protection scheme for hot-switching life-time enhancement.

the contact resistance of the shunt protection contact. The main contact on the unprotected switch and the protected switch can be modeled as a variable parallel plate capacitor C_m with a varying gap d between the top and bottom electrode. The protection contact of the shun-protected switch can also be modeled as variable parallel plate capacitor C_p

$$\begin{aligned} C_m &= \epsilon \frac{A_m}{d}, \\ C_p &= \epsilon \frac{A_p}{d}, \end{aligned} \quad (3.1)$$

where ϵ is the permittivity of the air, A_m and A_p are the overlap between top and bottom electrode, and d is the gap between the top electrode and the bottom electrode. The series inductance and parasitic capacitance are omitted for simplicity. The dimple area is much smaller than the overlap, so the dimple is also omitted in the total capacitance calculation of the contact area.

The S-parameters of the unprotected switch [Fig 3.3(a)] are [72]

$$S_{11} = \frac{1}{1 + 2j\omega Z_0 C_m}, \quad (3.2)$$

$$S_{12} = \frac{2j\omega Z_0 C_m}{1 + 2j\omega Z_0 C_m}, \quad (3.3)$$

where ω is the angular frequency of the RF signal, and $Z_0 = 50 \Omega$ is the characteristic impedance of the transmission line.

The voltage (peak voltage) across the switch contacts with an input power of P coming into the switch is

$$V_{sw} = V_1^- + V_1^+ - V_2^- = (S_{11} + 1 - S_{12})V_1^+, \quad (3.4)$$

where $V_1^+ = \sqrt{2PZ_0}$ is the amplitude of the incident wave (from the input port), V_1^- the amplitude of the reflected wave, V_2^- the amplitude of the transmitted wave.

The voltage $V_{sw,u}$ across the unprotected switch can then be calculated

$$V_{sw,u} = \sqrt{\frac{4}{4Z_0^2\omega^2 C_v^2 + 1}} \cdot \sqrt{2PZ_0}. \quad (3.5)$$

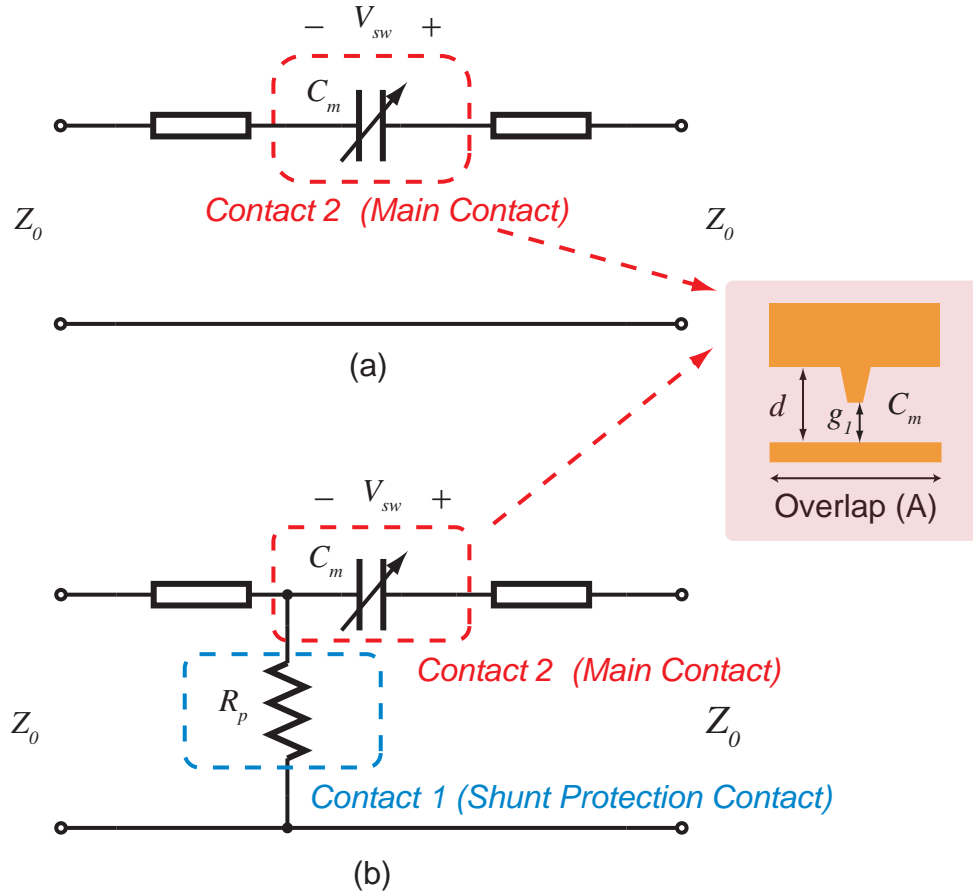


Figure 3.3. Equivalent circuit of (a) switch without protection at the moment of hot-switching; (b) switch with shunt protection at the moment of hot-switching (step B1, B4).

In comparison, the S-parameters of the protected switch [Fig 3.3(b)] are

$$S_{11} = \frac{R_p - Z_0^2 j\omega C_m - Z_0}{2Z_0 R_p j\omega C_m + R_p + Z_0^2 j\omega C_m + Z_0}, \quad (3.6)$$

$$S_{12} = \frac{2Z_0 R_p j\omega C_m}{2Z_0 R_p j\omega C_m + R_p + Z_0^2 j\omega C_m + Z_0}, \quad (3.7)$$

The voltage across the main contact can be found using the same equation 3.4

$$V_{sw,m} = \sqrt{\frac{4}{\left(1 + \frac{Z_0}{R_p}\right)^2 + \left(2Z_0 + \frac{Z_0^2}{R_p}\right)^2 \omega^2 C_m^2}} \cdot \sqrt{2PZ_0}, \quad (3.8)$$

where R_p is the contact resistance of the shunt switch.

The electric field between the dimple area and the bottom electrode is

$$E_0 = \frac{V_{sw}}{g_1}, \quad (3.9)$$

where g_1 is the gap distance between the dimple area and the bottom electrode.

Fig. 3.4 shows a comparison of the maximum electric field intensity E_0 between the unprotected switch and shunt protected switch for several R_p values and gaps under 1 W power input. The calculation used device geometry parameters listed in Table 3.1. The RF frequency used was 2.4 GHz. As the gap between the top contact dimple and the bottom contact electrode gets closer, the electric field intensity will increase for both switches. However, the electric field intensity of the main contact of the protected switch is significantly lower than that of the main contact of the unprotected switch.

The ratio (α) between the electric field intensity on the main contacts of the protected switch and the unprotected switch can be expressed as

$$\alpha = \frac{E_{maxsw,m}}{E_{maxsw,u}} = \sqrt{\frac{4Z_0^2\omega^2C_v^2 + 1}{(1 + \frac{Z_0}{R_p})^2 + (2Z_0 + \frac{Z_0^2}{R_p})^2\omega^2C_m^2}}. \quad (3.10)$$

Fig. 3.5 plots the ratio over different protection contact resistances. When the protection resistance is smaller than 20 Ω , the electric field intensity on the protected one is one third of that on the unprotected one. Thus, the main contact in the protected switch will have less damages caused by strong electric field during hot-switching. If the shunt protection resistance is smaller, more RF power will be reflected, making the electric field intensity on the main contact much smaller.

3.2.2 Comparison Between Shunt-protected Switch and Series-protected Switch

Both the series protection [14] and shunt protection technique can provide hot-switching damage protection by lowering the electric field intensity on the main contact. Comparison between the two techniques will be discussed in this section.

Fig. 3.6 shows the circuit schematic of a series-protected switch and a shunt-protected switch at the moment when the main contact is closing (or opening)

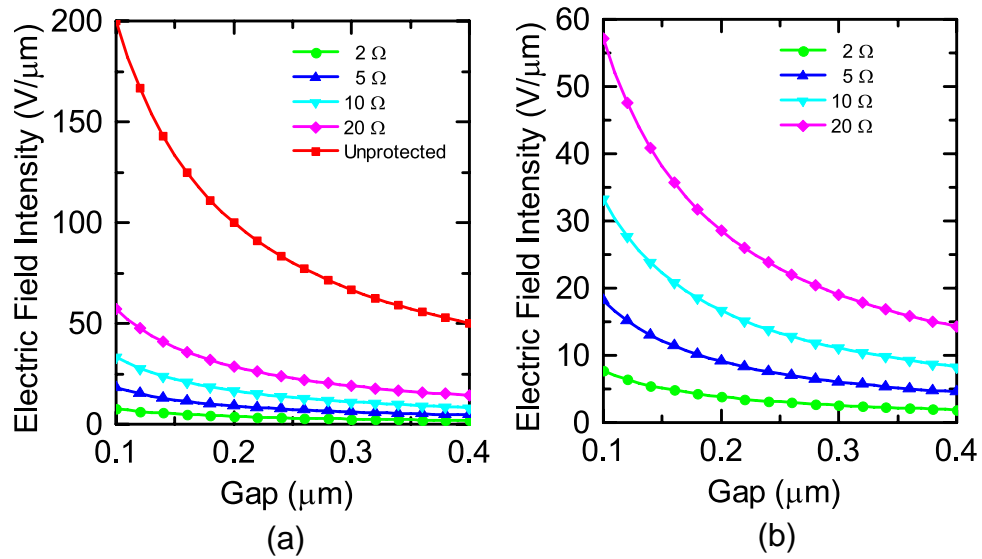


Figure 3.4. (a) Calculated electric field intensity of unprotected switch and switches with different shunt protection contact resistances; (b) zoom in of (a) for low shunt protection resistance.

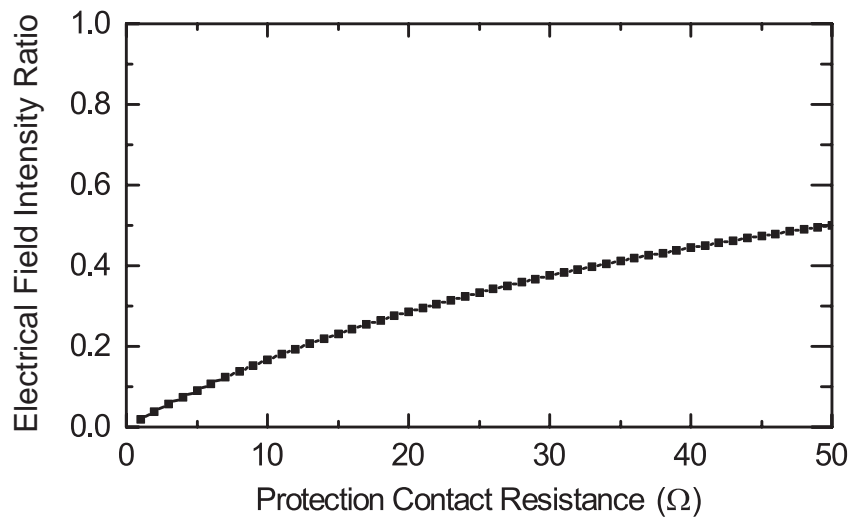


Figure 3.5. Ratio between the electric field intensity on the main contacts of the protected switch and the unprotected switch.

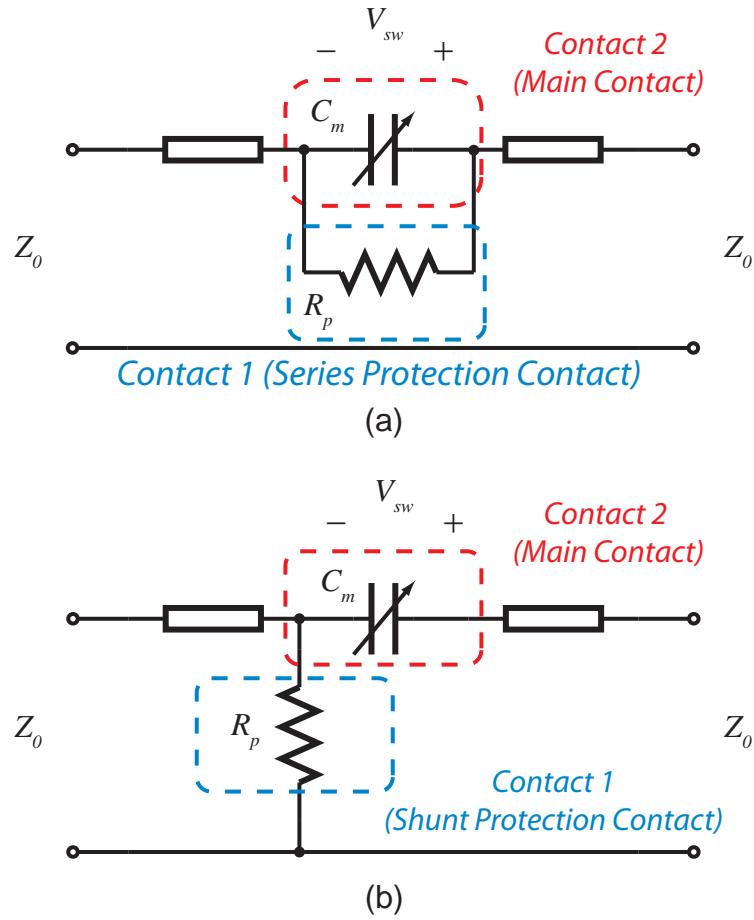


Figure 3.6. Equivalent circuit of (a) switch with series protection at the moment of hot-switching (step A2, A3); (b) switch with shunt protection at the moment of hot-switching (step B2, B3).

(step A2, A3, B2, B3). The protection contacts of both switches are closed.

The voltages across the main contacts of both in Fig 3.6(a) and (b) are

$$V_{sw,mseries} = \sqrt{\frac{8PZ_0}{\left(1 + \frac{2Z_0}{R_p}\right)^2 + 4Z_0^2\omega^2C_m^2}}, \quad (3.11)$$

and

$$V_{sw,mshunt} = \sqrt{\frac{8PZ_0}{\left(1 + \frac{Z_0}{R_p}\right)^2 + \left(2Z_0 + \frac{Z_0^2}{R_p}\right)^2\omega^2C_m^2}}, \quad (3.12)$$

respectively.

Fig. 3.7 shows the comparison between the calculated electric field intensity

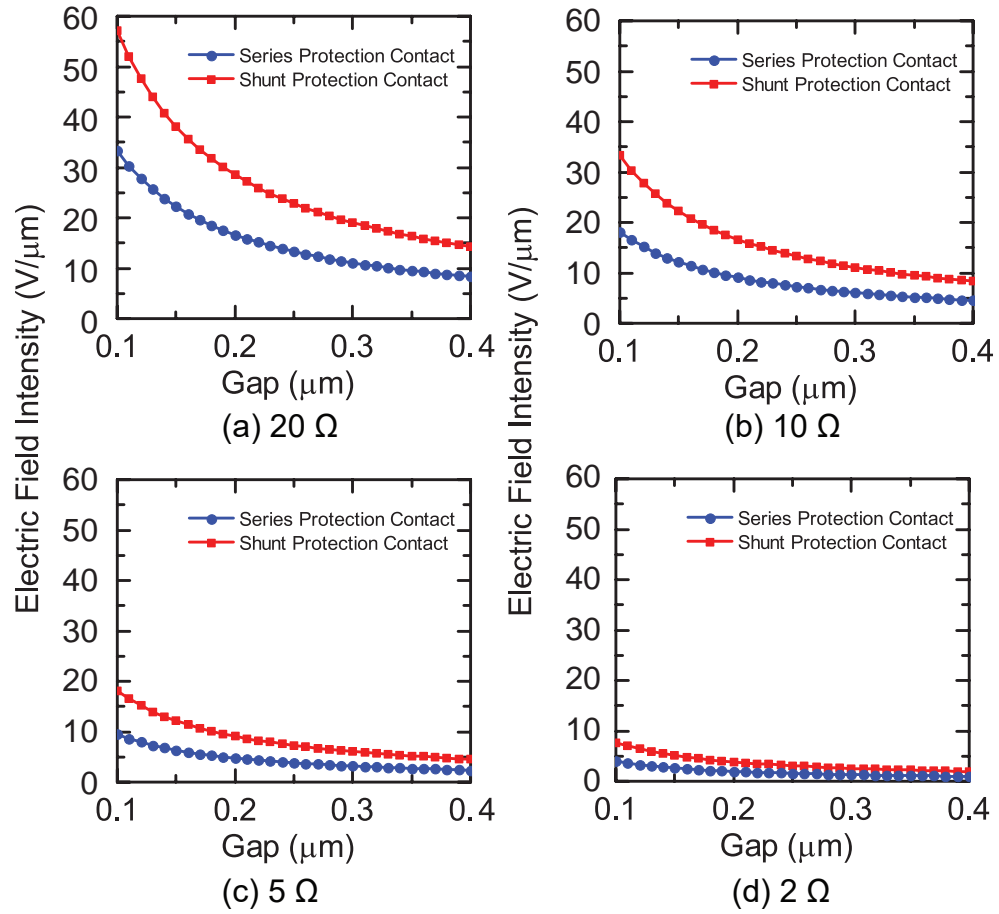


Figure 3.7. Comparison between the calculated electric field intensity of the main contacts of the series-protected and shunt-protected switches when the protection contact resistances are (a) $20\ \Omega$; (b) $10\ \Omega$; (c) $5\ \Omega$; (d) $2\ \Omega$. The calculation assumes a center frequency of 2.4 GHz.

of the main contacts of the series-protected and shunt-protected switches as the contact gap is closing (opening), for different protection contact resistances. The electric field intensity on the main contact of series-protected switch is approximately half of that on the shunt-protected switch.

The electric field intensity on the protection contact before the protection contact is closed (or open) can also significantly affect the overall lifetime of the switch (Step A1, A4, B0). With directly exposed to higher electric field intensity, the protection contact could be worn out sooner. The contact resistance could increase faster over hot-switching cycles. High contact resistance of the protection contact

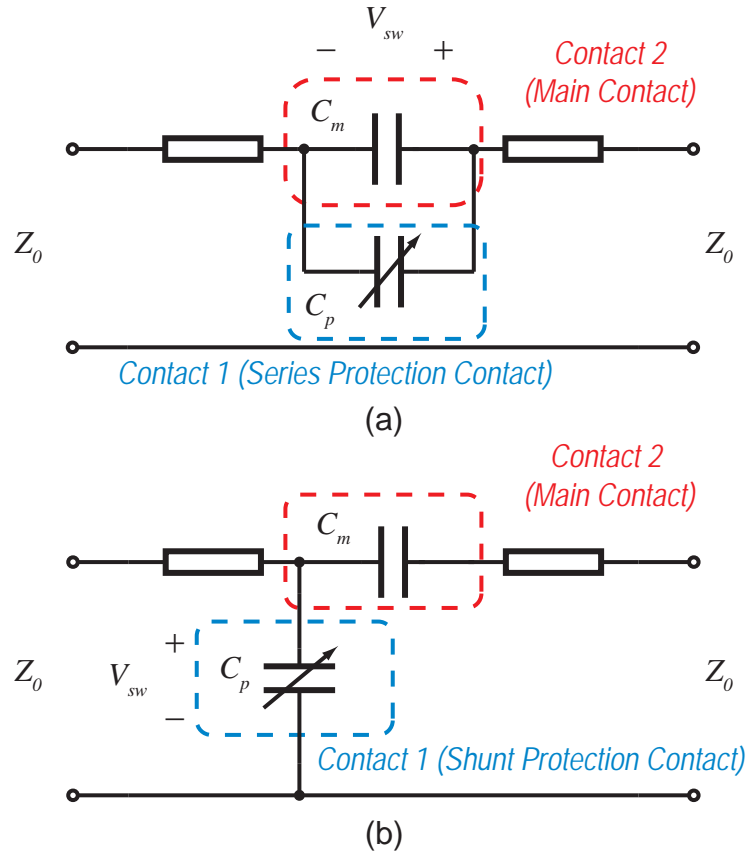


Figure 3.8. Equivalent circuit of (a) switch with series protection before the protection contact is closed (open) (step A1, A2); (b) switch with shunt protection before the protection contact is closed (open) (step B0).

will give less protection for the main contact. Fig. 3.8 shows the equivalent circuit of a series-protected switch and a shunt-protected switch before their protection contacts are closed.

For the series-protected switch in Fig. 3.8 (a), the S-parameters are

$$S_{11} = \frac{1}{2Z_0 j\omega(C_m + C_p) + 1}, \quad (3.13)$$

$$S_{12} = \frac{2Z_0 j\omega(C_m + C_p)}{2Z_0 j\omega(C_m + C_p) + 1}. \quad (3.14)$$

The voltage across the series protection contact is

$$V_{sw,pseries} = V_1^- + V_1^+ - V_2^- = (S_{11} + 1 - S_{12})V_1^+ \quad (3.15)$$

$$= \sqrt{\frac{4}{4Z_0^2\omega^2(C_p + C_m)^2 + 1}} \cdot \sqrt{2PZ_0}, \quad (3.16)$$

For the shunt-protected switch in Fig. 3.8(b), the S-parameters are

$$S_{11} = \frac{1 + \omega^2 C_m C_p Z_o^2 - Z_0 j \omega C_p}{2Z_0 j \omega C_m + 1 - Z_0^2 \omega^2 C_m C_p + Z_0 j \omega C_p}, \quad (3.17)$$

$$S_{12} = \frac{2Z_0 j \omega C_m}{2Z_0 j \omega C_m + 1 - Z_0^2 \omega^2 C_m C_p + Z_0 j \omega C_p}. \quad (3.18)$$

The voltage across the shunt protection contact is

$$V_{sw,pshunt} = V_1^- + V_1^+ = (S_{11} + 1)V_1^+ = \sqrt{2PZ_0} \cdot \frac{\sqrt{(2 + 4Z_0^2\omega^2 C_m^2)^2 + 4\omega^2 Z_0^2 (Z_0^2\omega^2 C_m^2 C_p + C_m + C_p)^2}}{(1 - Z_0^2\omega^2 C_m C_p)^2 + (2Z_0\omega C_m + Z_0\omega C_p)^2}. \quad (3.19)$$

The overlap between the top contact dimple and the bottom electrode is small. Thus, the capacitance is in the range of femto farad. When the device is operating in GHz range, it can be assumed that

$$Z_0\omega C_p \ll 1, \quad (3.20)$$

$$Z_0\omega C_m \ll 1, \quad (3.21)$$

$$Z_0\omega(C_p + C_m) \ll 1. \quad (3.22)$$

In this case, equation 3.16 and 3.19 can be simplified to

$$V_{sw,pseries} = V_{sw,pshunt} = 2\sqrt{2PZ_0}. \quad (3.23)$$

Essentially, the protection contacts on both series-protected and shunt-protected will have the same electric field intensity damage during steps. The protection contacts on the series-protected switch will undergo this amount of high electric field intensity twice from OFF state to TRANSITION state and from TRANSITION state to OFF state (step A1, A4). The shunt protected contacts, however, can remain in close to leave the switch in HIGH-ISOLATION state (The switch does

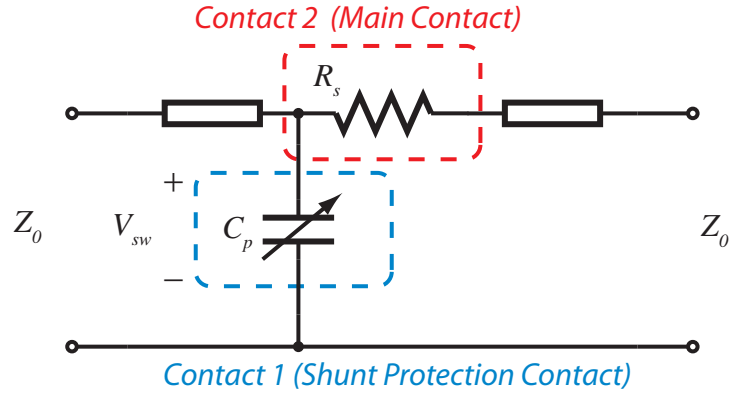


Figure 3.9. Equivalent circuit model of the shunt-protected switch when the protection contact is about to open (close) while the main contact is closed (step B2, B3).

not necessarily go back to INITIAL state.). Thus, the shunt-protected switch will only have one time TRANSITION from INITIAL state to HIGH-ISOLATION state (step B0). The transition can also happen in cold-switching condition to avoid any damage. However, the RF current will pass through shunt-protection contact at HIGH-ISOLATION state when the shunt-protection contact is prolongedly actuated, which makes the switch susceptible to adhesion problem at HIGH-ISOLATION state.

From TRANSITION state to ON state (From ON state to TRANSITION state) (step B2, B3), the protection contact will be open (close) and undergo addition hot-switching damage. Fig. 3.9 shows the equivalent circuit model of the shunt-protected switch when the protection contact is about to open (close), while the main contact is closed.

The S_{11} of the equivalent circuit is

$$S_{11} = \frac{R_s - Z_0 j\omega C_p - R_s Z_0 j\omega C_p}{2Z_0 + R_s + (Z_0^2 + Z_0 R_s) j\omega C_p}. \quad (3.24)$$

Then, the voltage across the shunt protection contact is

$$\begin{aligned} V_{sw,ushunt} &= V_1^- + V_1^+ = (S_{11} + 1)V_1^+ \\ &= \sqrt{\frac{(2Z_0 + 2R_s)^2}{(2Z_0 + R_s)^2 + (Z_0^2 + Z_0 R_s)^2 \omega^2 C_p^2}} \cdot \sqrt{2PZ_0}. \end{aligned} \quad (3.25)$$

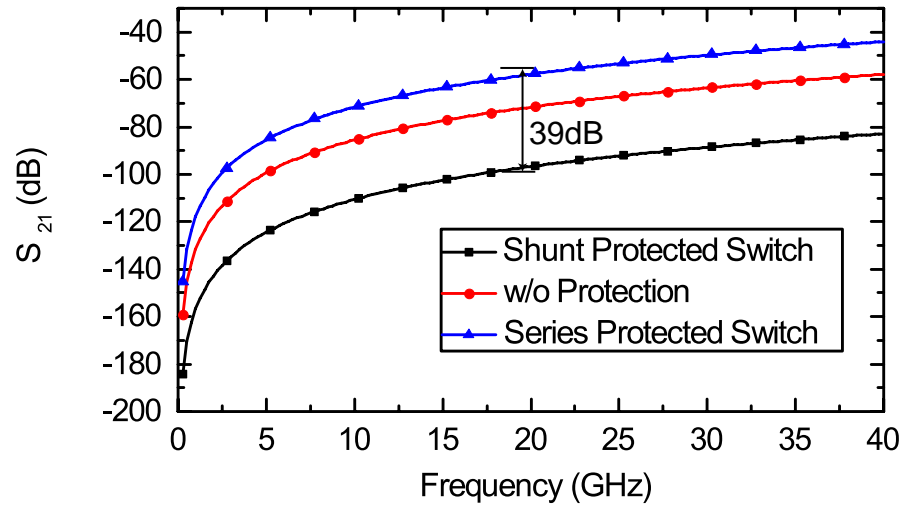
Since $R_s \ll Z_0$ and $Z_0^2 \omega^2 C_p^2 \ll 1$, the equation can be simplified as

$$V_{sw,ushunt} = \sqrt{2PZ_0}. \quad (3.26)$$

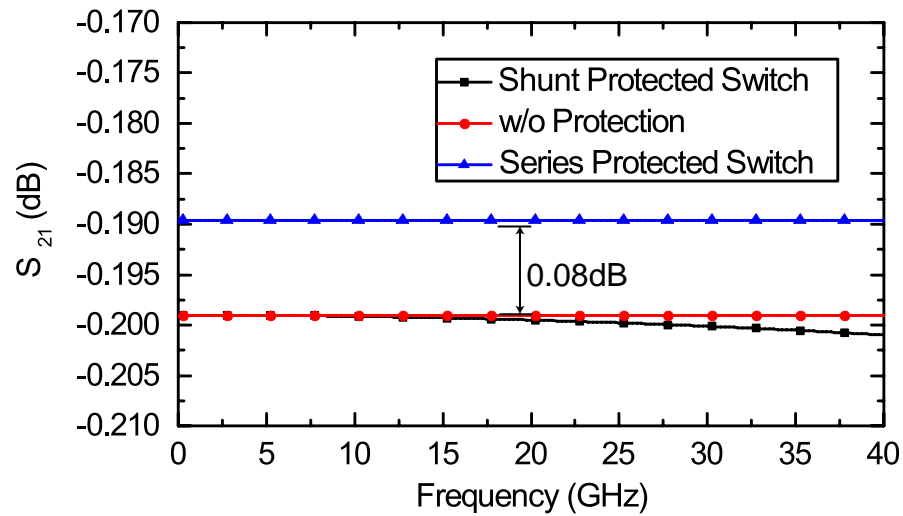
Comparing equation (3.23) and (3.26), the electric field intensity during the hot-switching at step B2 is half of the electric field intensity seen by the protection contact on series-protected switch during hot-switching. From ON state back to TRANSITION state (step B3), the shunt protection contact will undergo the same hot-switching damage with the same electric field intensity. Overall, the electric field intensity during hot-switching on the protection contact of shunt-protected switch is half of the one on series-protected switch.

Fig. 3.10 plots the calculated S-parameter of a shunt-protected switch, a series-protected switch and an unprotected switch. The protection contact resistances is assumed to be $5\ \Omega$ for both shunt and series case in the calculation. $1\text{-}\Omega$ contact resistance is assumed for all main contacts. In the OFF state, it is assumed that the shunt protection contact is closed. In the ON state, it is assumed that the series protection contact is closed. All other parasitic capacitance and inductance are ignored. It can be seen that in the OFF state the shunt-protected switch has better isolation, and the series-protected switch has worse isolation than the unprotected one because of the additional RF coupling of the capacitor formed in series protection contact. In the ON state the shunt-protected switch has slightly worse insertion than the unprotected one since there is a small capacitor in shunt. The series-protected switch has better insertion because of the additional series protection contact.

In summary, the hot-switching electric field intensity on the main contact of shunt-protected switch is twice of that of the series-protected switch. The hot-switching electric field intensity on the protection contact of shunt-protected switch is half of that of the series-protected switch. Based on these two observations, we expect approximately similar lifetime enhancement from the series- and shunt-protection schemes. The advantage of the shunt-protected switch lies in its much better OFF-state isolation due to the series-shunt configuration.



(a) Switch OFF state



(b) Switch ON state

Figure 3.10. Calculated S-parameter for a shunt-protected switch, a series-protected switch and an unprotected switch.

3.2.3 Switch Design and EM Analysis

Fig. 3.11 and Table 3.1 show the design parameters of the switch. The device consists of three cantilever beams. The shunt protection switch beam length is slightly shorter than the main switch beam length to achieve faster switching speed. The main contact is made of gold to lower the contact resistance, and the shunt protection contact is made of refractory metal to withstand hot-switching damage. Mechanical stop dimple is designed to prevent the cantilever accidentally touching the biasing pad which can cause catastrophic failure of the switch. Dielectric film is not used within the biasing electrostatic field line to avoid any dielectric charging. An air bridge is formed to let the high-resistance biasing line pass through the ground plane.

The proposed switch design is simulated in ANSYS HFSS. Fig 3.12 shows the current distribution of the switch before and after the main switch is closed. The RF current is blocked by the shunt protection contact, and the main contact will meet less RF power and have less hot-switching damage. Fig. 3.13 shows the simulated S-parameters of the proposed design. According to the simulation results, the switch has better than 40 dB isolation in high-isolation state up to 40 GHz and better than 0.9 dB insertion loss in ON state up to 40 GHz. The simulated S-parameter is very close to measurement results.

3.3 Experimental Validation

3.3.1 Device Fabrication

The all-metal process [14] was used to fabricate the switch. The process was similar with the process used in previous chapter only with slight changes. The copper sacrificial layer was changed to chromium sacrificial layer. The chromium layer can withstand gold etchant in the following steps to ensure a cleaner process and higher fabrication yield. The use of the chromium layer also shrinks the total types of metal used in the all-metal process to four: gold, platinum, titanium and chromium. The fabricated devices are shown in Fig. 3.14. Both protected switch

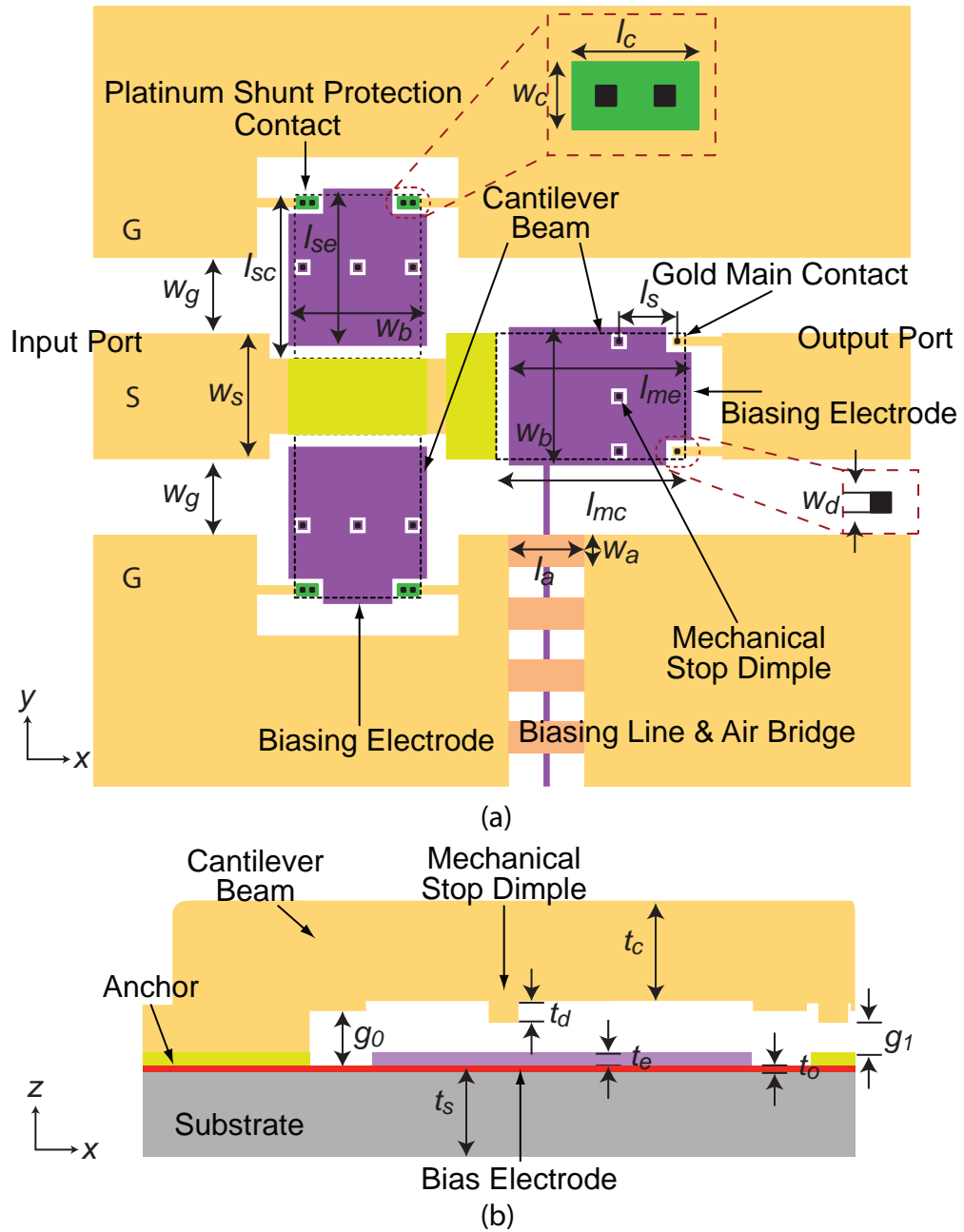


Figure 3.11. (a) Top view of the shunt-protected switch; (b) side view of the cantilever.

Table 3.1. Geometry parameters of the switch

Geometry parameter	Symbol	Value (μm)
CPW line width	w_s	100
CPW line gap	w_g	60
Beam width	w_b	100
Dimple width	w_d	2.5
Electrode width	w_d	110
Shunt contact width	w_c	8.5
Air bridge width	w_a	25
Main switch beam length	l_{mc}	150
Shunt protection switch beam length	l_{sc}	130
Main switch electrode length	l_{me}	145
Shunt protection switch electrode length	l_{se}	125
Air bridge length	l_a	60
Stopper and main contact separation	l_s	45
Shunt contact width	l_c	16
Beam thickness	t_b	5
Dimple thickness	t_d	0.5
Biasing electrode thickness	t_e	0.15
Thermal oxide thickness	t_o	0.5
Substrate thickness	t_s	500
Cantilever to electrode gap	g_0	0.9
Dimple to contact gap	g_1	0.4

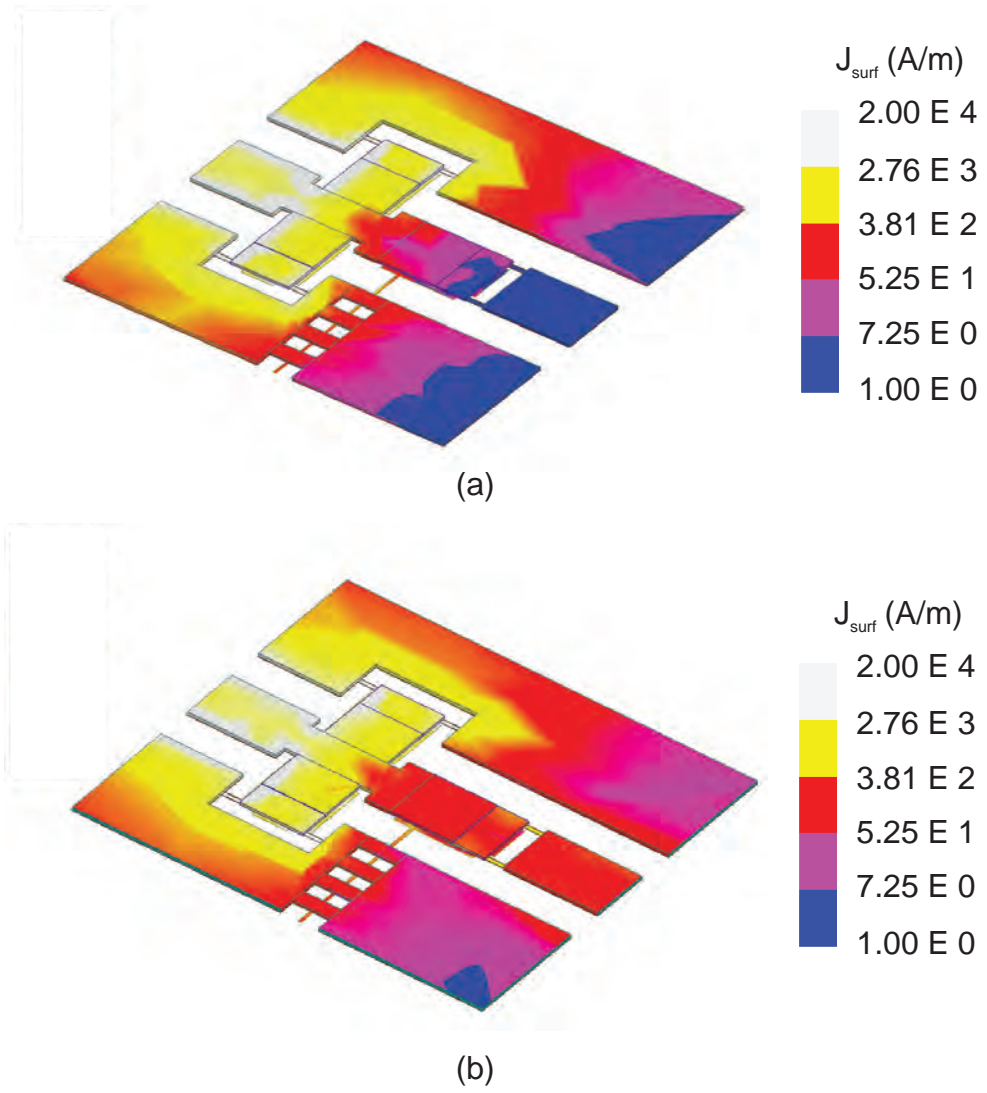


Figure 3.12. (a) Current distribution of the switch before the main switch closed; (b) current distribution of the switch after the main switch closed.

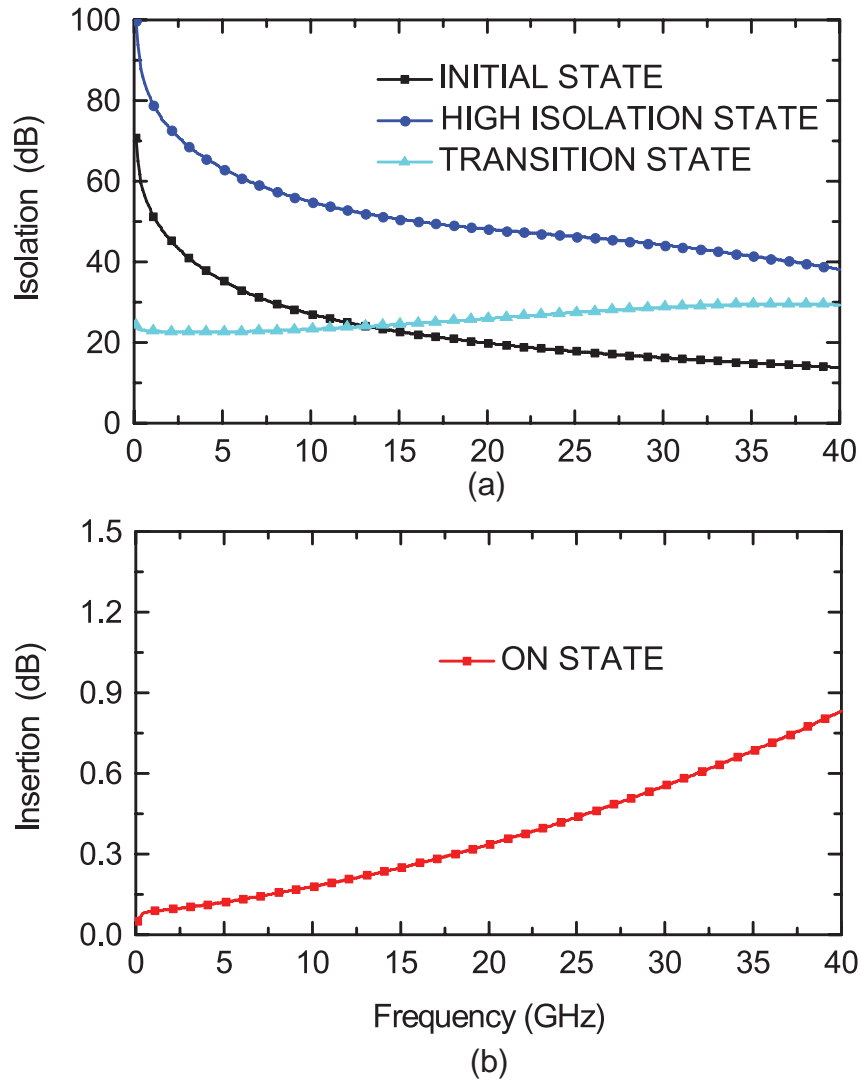


Figure 3.13. Simulated (a) isolation of the switch in INITIAL state, HIGH ISOLATION state, and TRANSITION state; (b) insertion loss of the switch in the ON state.

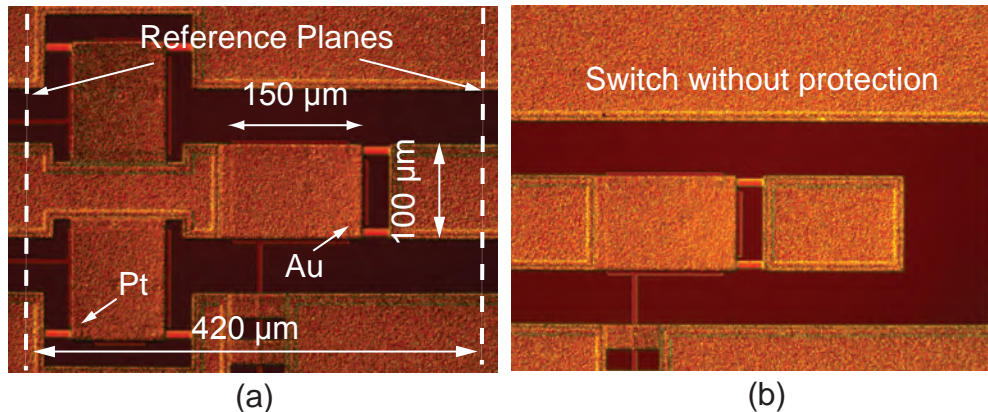


Figure 3.14. Pictures of the (a) protected switch and (b) unprotected switch.

(Fig. 3.14(a)) and unprotected switch (Fig. 3.14(b)) are fabricated in parallel for comparison in tests later.

3.3.2 S-Parameters

The S-Parameters of the switch was measured by a Keysight 8722D network analyzer with Ground-Signal-Ground (GSG) microwave probes. The probes was calibrated to the reference line in Fig. 3.14(a) using Through-Reflection-Line (TRL) technique. The calibration kit was fabricated along side with the MEMS devices on the same wafer using the same process. The measured S-parameters, shown in Fig. 3.15, is close to the simulation results, and the switches were biased at 60 V. For the shunt-protected switch the isolation is 43.5 dB in the initial state, 72.3 dB in the high isolation state, and 25.8 dB in the transition state at 1.0 GHz. The isolation is 14.4 dB in the initial state, 36.0 dB in the high isolation state, and 22.1 dB in the transition state at 40 GHz. The isolation of the switch improves by 39.1 dB at 2.4 GHz. The insertion loss is 0.3 dB at 1 GHz and 0.48 dB at 40 GHz. For the unprotected switch, shown in Fig. 3.16, the isolation is 41.6 dB at 1 GHz and 14.1 dB at 40 GHz, and the insertion loss is 0.22 dB at 1 GHz and 0.25 dB at 40 GHz. The protected switch has significantly higher isolation (>30 dB) than the unprotected switch and similar insertion loss over 0–40 GHz range.

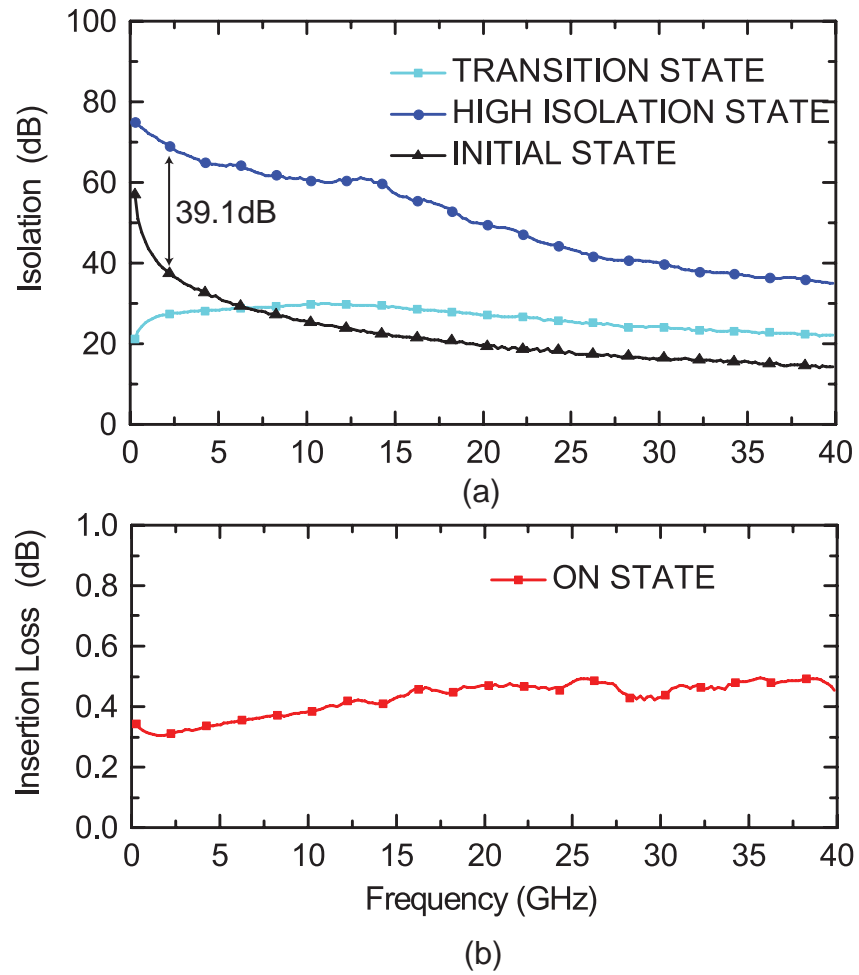


Figure 3.15. Measured S-parameter of shunt-protected switch: (a) isolation of INITIAL state, HIGH ISOLATION state, and TRANSITION state; (b) insertion loss of ON state.

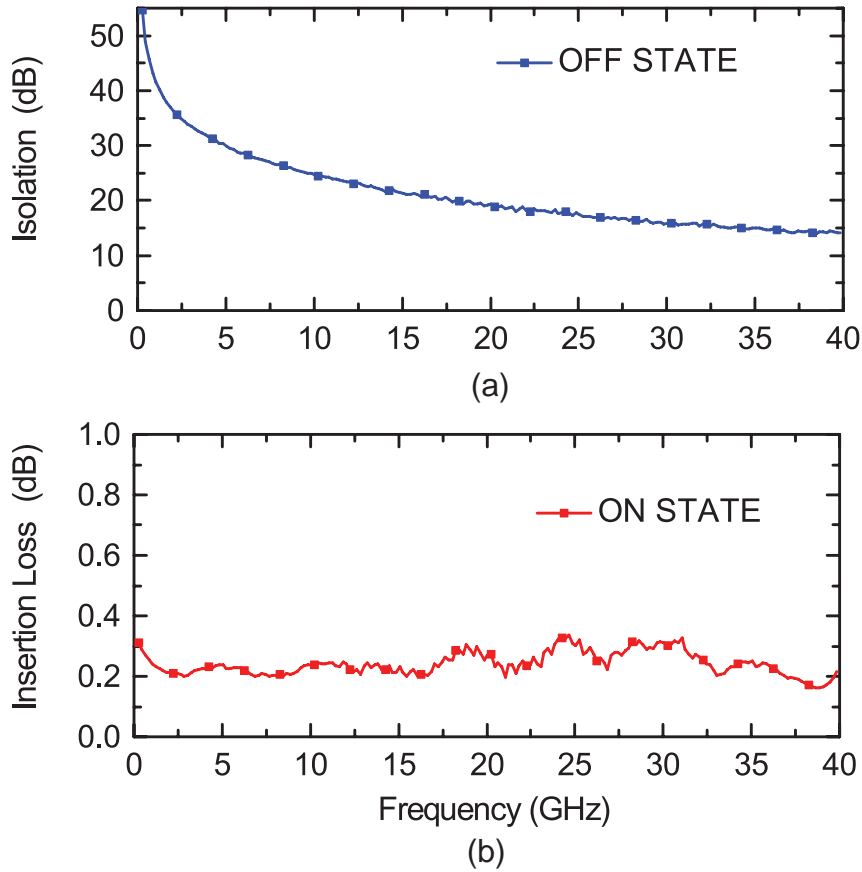


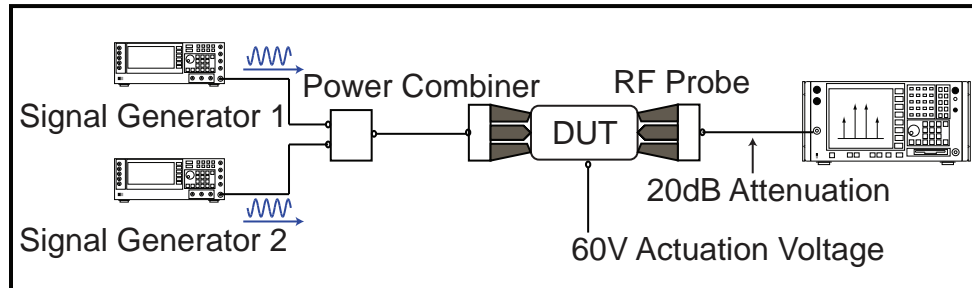
Figure 3.16. Measured S-parameter of unprotected switch: (a) isolation of OFF state; (b) insertion loss of ON state.

3.3.3 Linearity Test

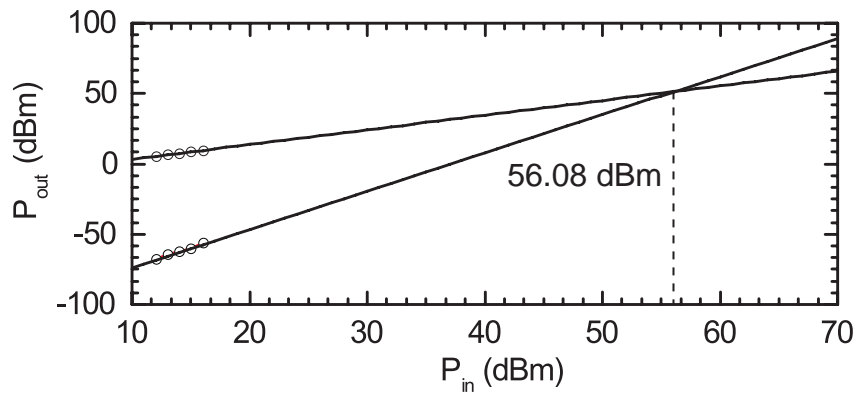
The linearities of a protected switch and a through line were measured. Two-tone measurement setup is shown in Fig. 3.17(a). Two tones were offset by 25 MHz at center frequency of 2.4 GHz. The resolution bandwidth is 20 kHz. The signal was attenuated by 20 dB before being sent into spectrum analyzer. The measured third order inter-modulation intercept point (IIP3) of the protected switch is 56.08 dBm, and that of the through line is 58.36 dBm.

3.3.4 Switching Time

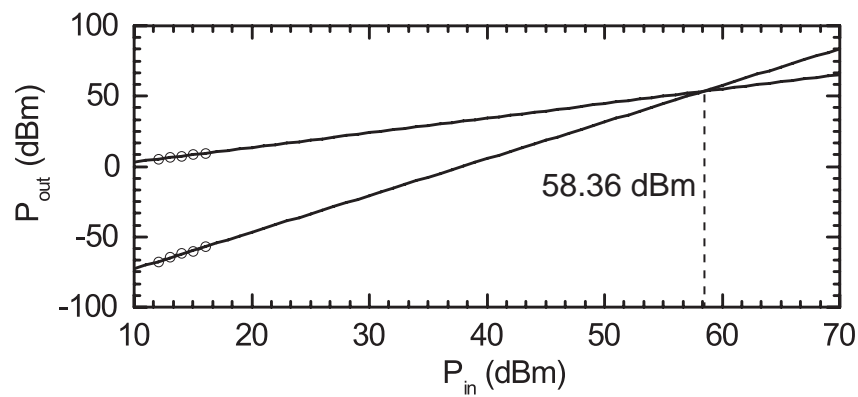
Switching time is measured before lifetime measurement in order to determine the appropriate cycling frequency. Test setup is shown in Fig 3.18. A 2.4-GHz signal was sent from an RF signal generator to the device through a bias tee.



(a)



(b)



(c)

Figure 3.17. (a) Linearity test setup; (b) IP3 of the shunt-protected MEMS switch; (c) IP3 of the through line.

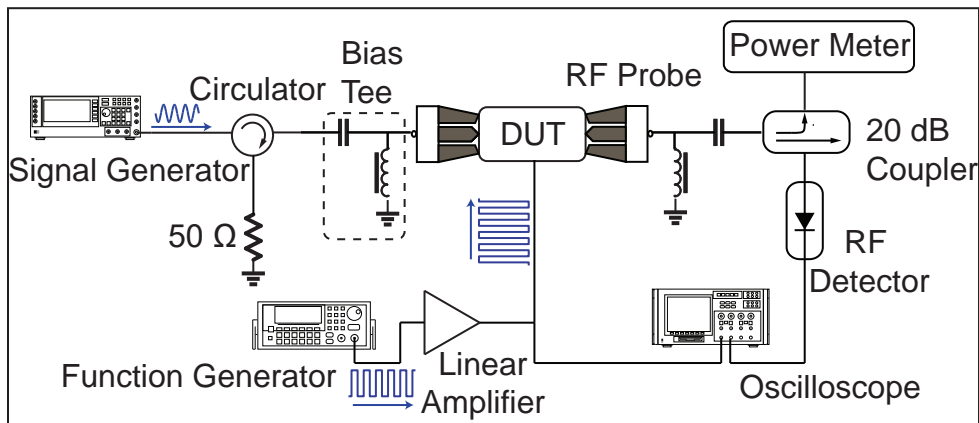


Figure 3.18. Setup schematics for switching time measurement.

The device was actuated by a square-wave biasing signal that was generated by a function generator and amplified by a linear amplifier. Peak-to-peak voltage is 50 V and frequency is 100 Hz. The output RF signal from the MEMS switch was detected and converted to dc voltage by a zero-biased RF detector. The DC voltage and the biasing signal were sent to oscilloscope to determine the switching time. The switching-on time is $30.4 \mu\text{s}$, and the switching-off time is $39.8 \mu\text{s}$, as shown in Fig. 3.19. The shunt protection cantilever is slightly shorter than the main cantilever, so the switching time for the shunt protection cantilever should be shorter.

3.3.5 Mechanical Cycle Test

Mechanical lifetime test was carried out first before electrical lifetime test in order to verify the mechanical life time of the fabricated switches. Two switches were test with no RF power passing through. The contact resistance was measured by 4-point resistance measurement setup during the switching cycles. The switches was biased using square wave with peak-to-peak voltage of 50 V and 50%. The frequency was set to 1 kHz before 10,000 cycles and 5 kHz till the test stopped. The two switches were cycled up to 1.5 billion times before the test stopped. The resistance changes during the cycling test is shown in Fig. 3.20. The resistances of both switches gradually increase over time due to mechanical wear and damage,

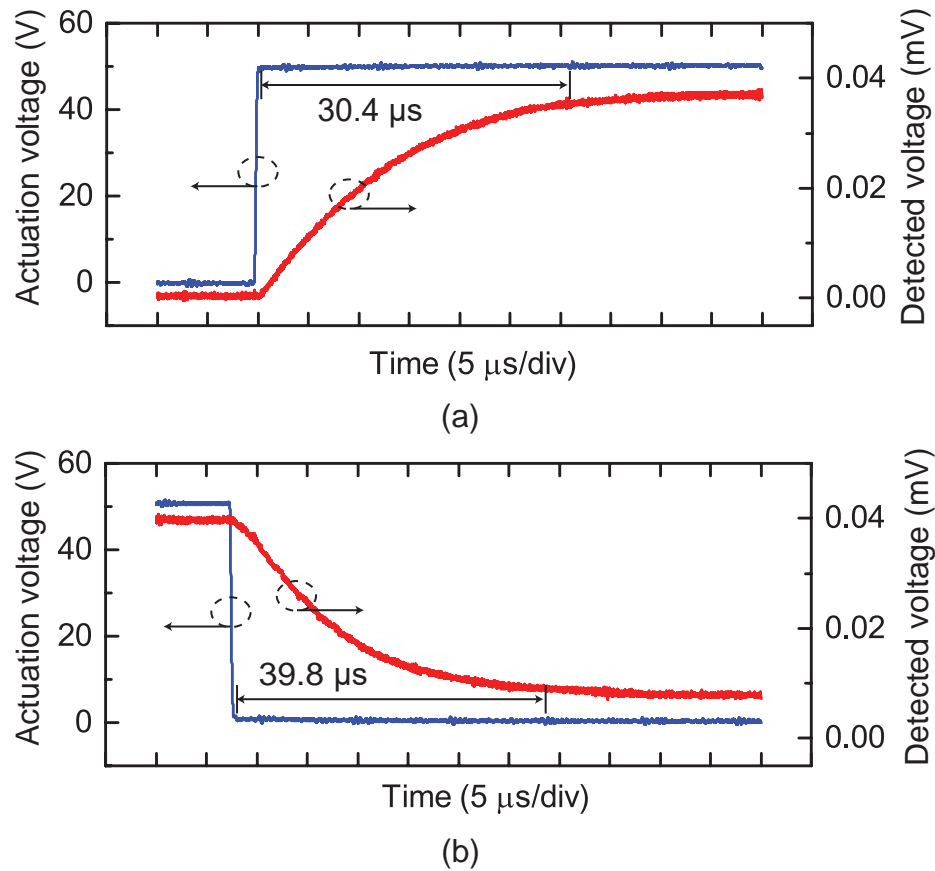


Figure 3.19. (a) Switching-on time; (b) switching-off time.

but are below $10\ \Omega$ after 1.5 billion cycles.

3.3.6 Hot-switching Lifetime Test

Hot-switching test setup is shown in Fig. 3.21. An amplified RF signal of 1 W at 2.4 GHz is sent to the device under test. A power meter was connected through a 20-dB directional coupler to monitor the power level of the incoming RF signal. A 4-point resistance measurement setup is connected through bias tees to monitor the contact resistance changes over lifetime. The output RF signal is connected through a directional coupler to RF detector. The dc voltage is sent into an oscilloscope to monitor the switching behavior.

In the first case, an unprotected switch was tested. The amplified square wave with duty cycle of 50% and peak-to-peak voltage of 50 V. The frequency of the

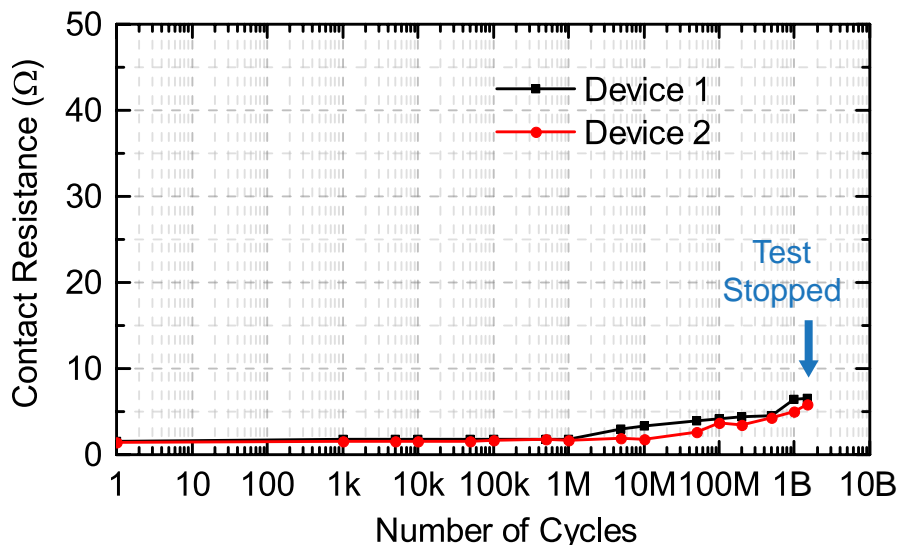


Figure 3.20. Mechanical cycling test for two RF-MEMS switch devices (Test stopped after the last data points were collected).

wave was set to 1 kHz before 10,000 cycles, and 5 kHz till the end of the test. Three unprotected devices were measured. Fig. 3.22 shows the resistance changes over the cycling period. The devices can be cycled up to 10 million cycles before failure. All switches failed as open circuit. The contact resistances became significantly large ($>200 \Omega$).

Next, the lifetime of the protected switches was measured under 1-W hot-switching condition. The shunt-protected switches are biased using the waveform (Fig. 3.23). The waveform consists of two identical sets of square waves which have a duty cycle of 66.7% and peak-to-peak voltage of 50 V. The phase of square wave that is used to bias the shunt protection contact has 180° lead on that used to bias the main contact to ensure that the shunt protect contact is closed when the main contact turns on and off, and that the shunt protect contact switches to open when the main contact is closed. The frequency of the biasing waveform was set to 333 Hz before 10,000 cycles, and 3,333 Hz till the end of the test. Three devices were test, and the lifetime of the switches increased to >100 million cycles. One of the switch lasted to 200 million cycles. The lifetime of the protected switch increases by at least 10 times than that of the unprotected switch.

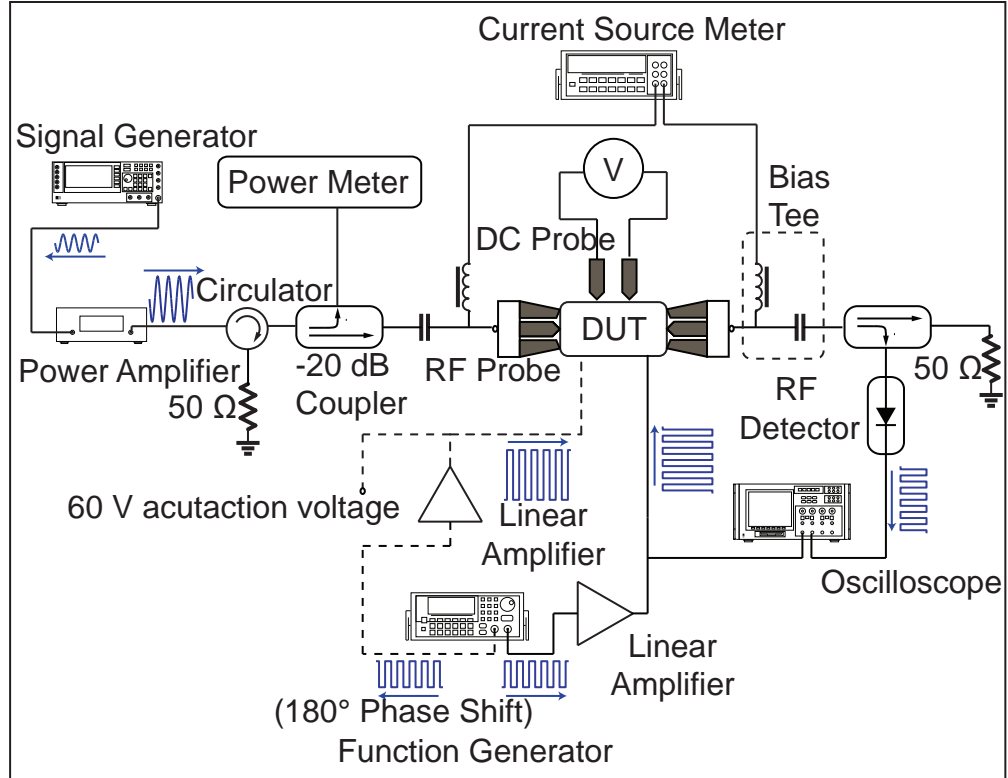


Figure 3.21. Test setup for hot-switching reliability characterization.

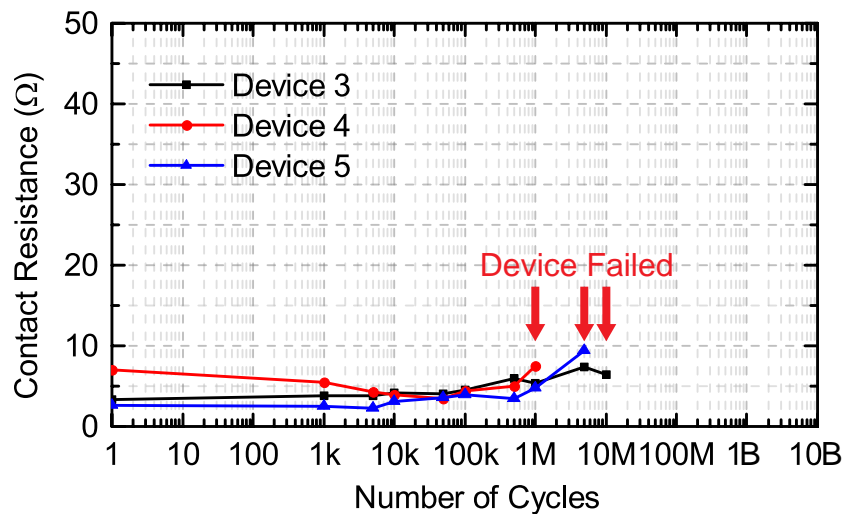


Figure 3.22. Contact resistances changes over cycling period of three unprotected switches under 1-W hot-switching condition (All devices failed as open circuit at the next data points collection).

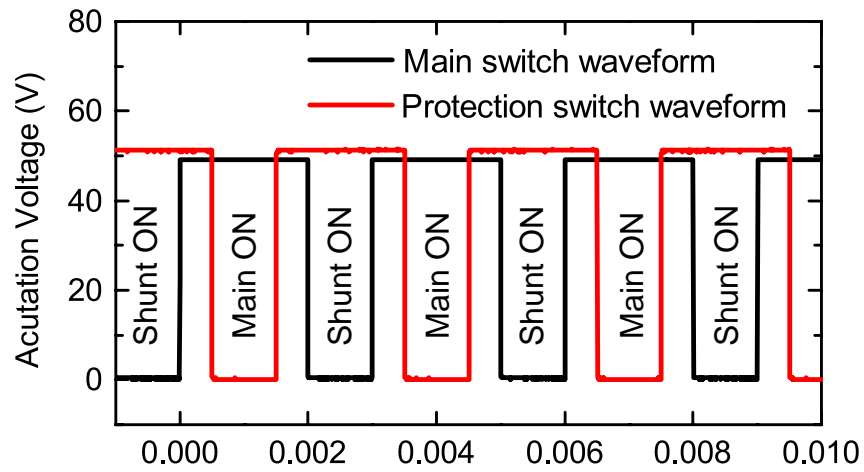


Figure 3.23. Actuation waveform for the shunt protected switches.

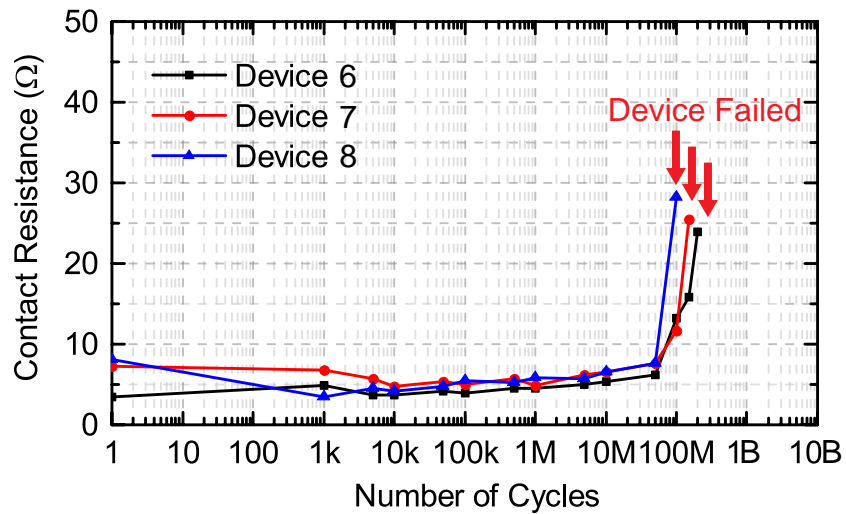


Figure 3.24. Contact resistances changes over cycling period of three protected switches under 1-W hot-switching condition (All devices failed as open circuit at the next data points collection).

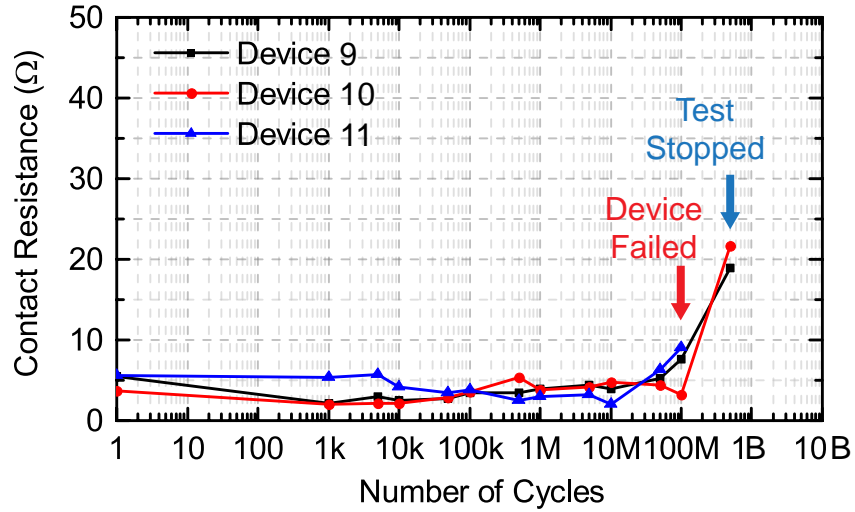


Figure 3.25. Contact resistances changes over cycling period of three continuous protected switches under 1-W hot-switching condition (One device failed as open circuit at the next data point collection, and for the other two devices test stopped after the last data points were collected).

The lifetime of the protected switches under 1-W hot-switching condition was also measured when the shunt protection contact was always closed. This test is done to understand the lifetime of the main contact excluding the impact from the protection contact. In the test the shunt protection contact was continuously biased at 60 V, and the square wave has a peak-to-peak voltage of 50 V and duty cycle of 50%. The frequency was set to 1 kHz before 10,000 cycles, and 5 kHz till the end of the test. Fig. 3.25 shows the lifetime characterization of the device when the shunt protection contact is continuously held down. The device can achieve >100 million cycles for all the three devices tested. Two of them reached >500 million cycles.

3.4 Conclusion

A shunt protection technique to improve hot-switching reliability and isolation of RF-MEMS metal contact switch is presented in this chapter. The comparisons between unprotected switch, shunt-protected switch and series-protected switch are theoretically analyzed. The experimental measurement shows both hot-switching

reliability and isolation improvement by utilizing shunt protection technique, making the technique a robust method to improve RF-MEMS metal contact switch performance.

Chapter 4

Single-Actuator Shunt-Series RF-MEMS Switch for Improved Hot Switching Performance and Isolation

4.1 Introduction

In the previous chapter, the shunt protection technique is presented to improve the hot-switching reliability. In this chapter, to further reduce the footprint of the switch and simplify the biasing circuit of the device a single actuator shunt-series RF MEMS switch with one biasing line is proposed and demonstrated to realize improved isolation and hot-switching performance together.

Fig. 4.1 shows the proposed switch structure. A single cantilever beam with multiple contact points is used to realize the shunt-series switch configuration by utilizing the bending mechanism of the beam. The switch goes through a high-isolation state to a low-insertion loss ON-state without relying on multiple biasing electrodes like the design in previous chapter.

4.2 Design

Fig. 4.2 presents the simulated mechanical characteristics of the cantilever switch. The simulation is carried out in CoventorWare [67]. The layout of the switch is shown in Fig. 4.1(a). The cantilever beam is assigned as Au, with an area of

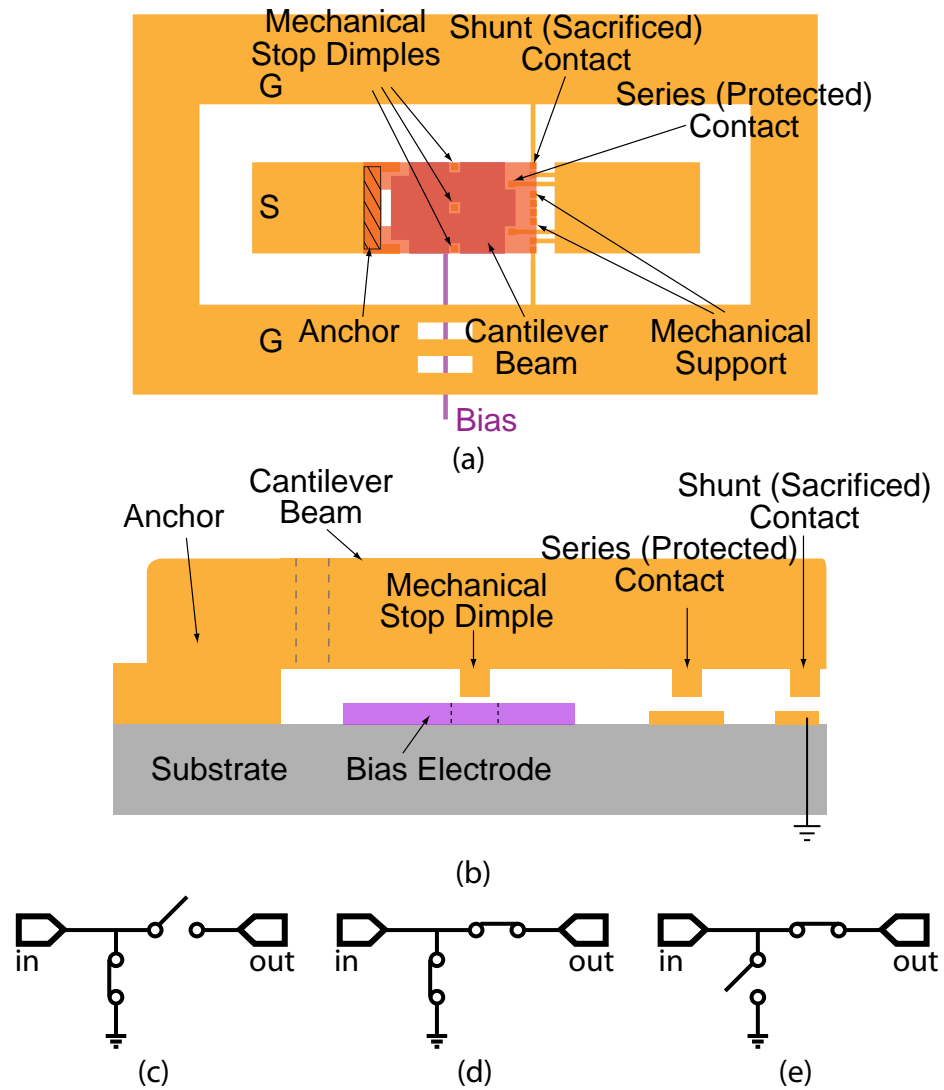


Figure 4.1. Concept of single-actuator shunt-series RF MEMS switch: (a) Top view; (b) Profile view; Equivalent circuits of (c) isolation state; (d) Equivalent circuit of transition state when both series and shunt contacts are closed; (e) Equivalent circuit of closed state.

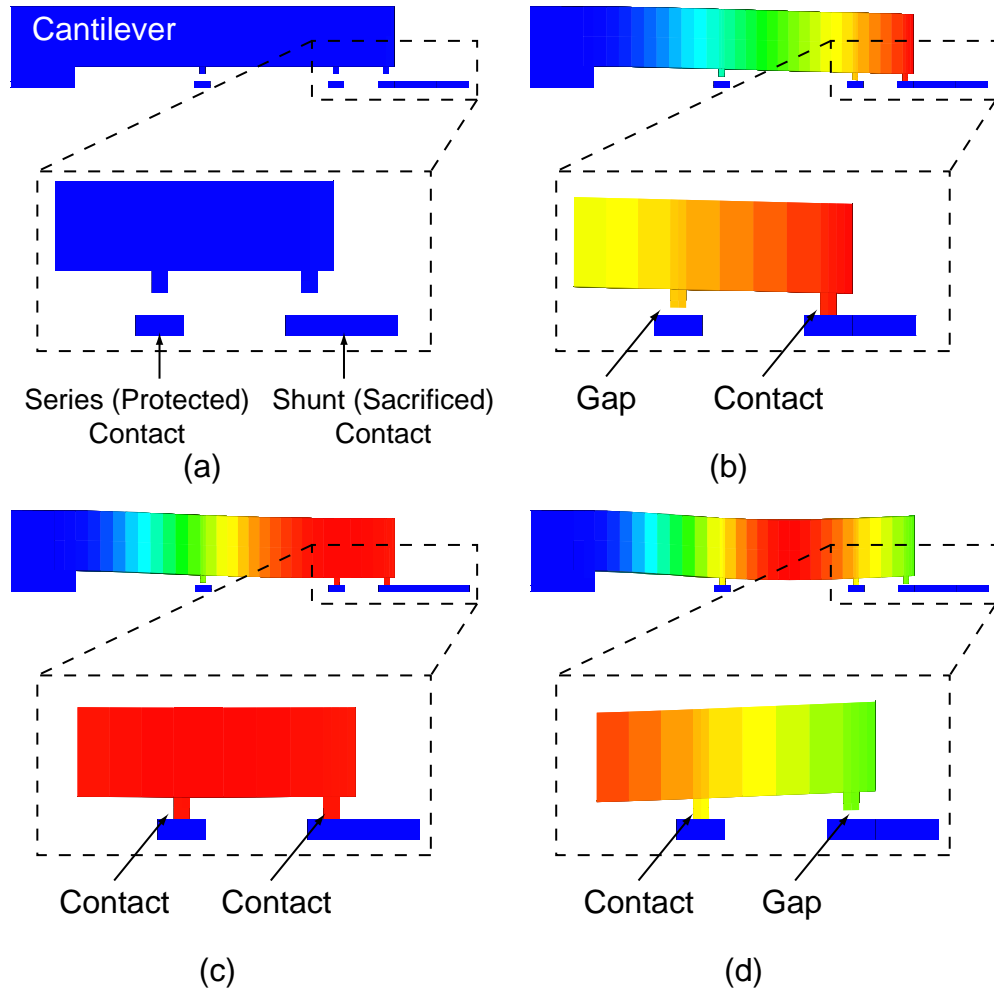


Figure 4.2. Simulated electromechanical and RF performances of the proposed shunt-series RF MEMS switch: (a) Off state; (b) High isolation state; (c) Transition state; (d) ON state.

$170 \times 100 \mu\text{m}^2$ and a thickness of $4.5 \mu\text{m}$. The dimple thickness is $0.6 \mu\text{m}$. The gap between dimple and bottom contact is $0.45 \mu\text{m}$. The gap and the dimple thickness configuration is to reduce pull-in instability to control the biasing voltage. An air bridge is constructed on top the biasing line passing through the ground plane. No dielectric material other than thermally grown oxide is deposited within the DC actuation field to reduce the charging problem. Additional mechanical supports are placed at the tip of the cantilever in case that the shunt contact dimples are destroyed during hot-switching to further improve the lifetime of the switch.

The movable part of the switch consists of a single cantilever beam with multiple

contacts. Two shunt contacts (dimples), which are connected to the ground plane of the coplanar waveguide (CPW), are placed at the outer tips of the cantilever beam. Two series contacts (dimples), which are connected to the signal line at the other end of the CPW, are placed inward the cantilever beam. When the cantilever beam is actuated, it first makes contact at the shunt dimples (Fig. 4.2(b)). This results in an improved isolation in the OFF state for low-power applications. As the actuation voltage is increased, the cantilever beams is pulled further down, resembling a zipping motion until it makes contacts at the series dimples (Fig. 4.2(c)). Upon further increasing the actuation voltage, the tip of the beam starts bending upwards (Fig. 4.2(d)), releasing the shunt contacts. In this state, the MEMS switch presents a low-loss ON-state. The beam profile before the beam starts to bending upwards is calculated in the previous chapter 2.18:

$$v(x) = \begin{cases} \frac{1}{24EI} (6ql_e^2x^2 - 4ql_ex^3 + qx^4 \\ \quad - 12F_2l_ex^2 + 4F_2x^3 \\ \quad - 12F_1l_bx^2 + 4F_1x^3), & 0 < x \leq l_e; \\ \frac{1}{24EI} (4F_1x^3 - 12F_1l_bx^2 + 4ql_e^3x \\ \quad - 12F_2l_e^2x + 4F_2l_e^3 - ql_e^4), & l_e \leq x \leq l_b. \end{cases} \quad (4.1)$$

From the beam profile, it can be shown that the contact forces on both series contact and shunt contact are:

$$F_1 = \frac{A_2A_5 - A_4A_3}{A_2^2 - A_1A_3}, \quad (4.2)$$

$$F_2 = \frac{A_2A_4 - A_1A_5}{A_2^2 - A_1A_3}, \quad (4.3)$$

where

$$\begin{aligned}
 A_1 &= -8l_b^3, \\
 A_2 &= 4l_e^3 - 12l_b l_e^2, \\
 A_3 &= -8l_e^3, \\
 A_4 &= 24EIg_1 - 4ql_e^3 l_b + ql_e^4, \\
 A_5 &= 24EIg_1 - 3ql_e^4.
 \end{aligned}$$

When the contact force on the shunt contact is zero, the dimple is about to start to leave the bottom contact. The condition is:

$$A_2 A_4 = A_1 A_5. \quad (4.4)$$

The proposed structure has the same advantage of the switch structure in previous chapter which is the protection of the electrical contact in hot switching conditions. It can reduce the contact degradation caused by gas discharge and breakdown. In the proposed design, the shunt contacts creates a local voltage minima (current maxima at the short circuit), thus significantly reducing the voltage difference between the series contact and the signal line. A local cold-switching condition is created for the series contacts. This allows the series contacts to be made of high-conductivity metals, such as Au, to reduce the on-state resistance of the switch. In the release of the switch, the above process is reversed. The series contact is first lifted off while the shunt dimples are still in contact. A similar cold-switching condition is presented.

In this configuration, the shunt contacts are subject to the same hot-switching-induced degradation as discussed in previous chapter. In a sense, the series contacts are protected in hot-switching conditions at the sacrifice of the shunt contacts. However, the degradation of the shunt contacts has little effect either the OFF-state (except that the improvement in isolation when the shunt contacts are is slightly degraded) or the ON-state (in terms of insertion loss). In addition, the shunt contacts can be made of refractory metals, such as Ru, Pt, and Re, whose much higher mechanical hardness makes the contacts more resistant to degradation.

Fig. 4.2 also shows simulated RF performances of the proposed switch in various states. Simulations are carried out in Ansys HFSS. The improvement in isolation can be clearly seen in Fig. 4.2(b).

4.3 Experimental Validation

4.3.1 Fabrication

Fig. 4.3 shows a summary of the key processing steps for the switch fabrication. The fabrication begins on a high resistivity (~ 10 k Ω -cm) oxidized silicon (0.5 μ m) substrate. The first layer uses liftoff to pattern a 150 nm thick high resistance (~ 1 k Ω/\square) SiCr DC biasline (Fig. 4.3a). Next, a second liftoff is used to pattern the 150 nm thick bottom gold contacts (Fig. 4.3b). A 450 nm thick copper sacrificial layer is sputtered and patterned with liftoff processing (Fig. 4.3c). Positive photoresist is spincoated to 600 nm thick and is used to pattern the cantilever dimple (Fig. 4.3d). A 50 nm chromium and 150 nm gold seed layer is sputtered for subsequent electroplating. Positive photoresist is spincoated to 6 μ m and patterned to form the electroplating mold for the cantilever (Fig. 4.3e). The cantilever is electroplated to 4.5 μ m thick. The electroplating mold, seed layer metals, and sacrificial layers are etched in their respective dedicated etchants. Finally, the devices are released and dried (Fig. 4.3f). Fig. 4.4 shows an SEM and optical image of the fabricated switch.

4.3.2 Measurement and Discussion

The RF measurements are performed with a E8364A network analyzer. Fig. 4.5 shows the measured operational states of the switch. When the switch is open (Fig. 4.5a) the isolation is -20 dB at 10 GHz and -14.7 dB at 20 GHz. A bias voltage of 33 V is applied to reach the high isolation state (Fig. 4.5a). In this state, the isolation improves to -33 dB at 10 GHz and -22.3 dB at 20 GHz. Fig. 4.5c shows the measurement at the transition state when both the shunt and series contacts are closed. This measurement is taken at a bias voltage of 100 V. Finally, Fig. 4.5d shows the on state of the switch. An insertion loss of -0.03 dB at 10 GHz

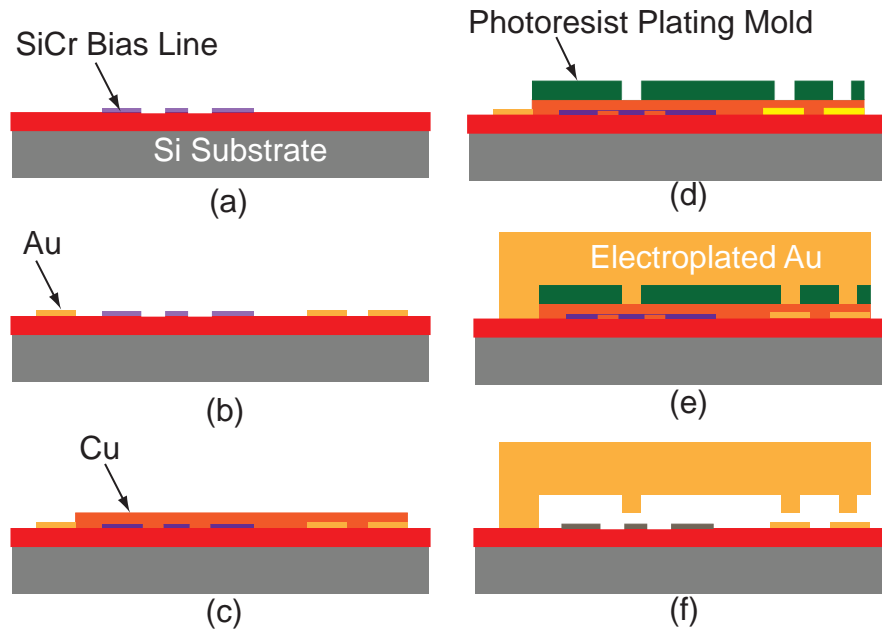


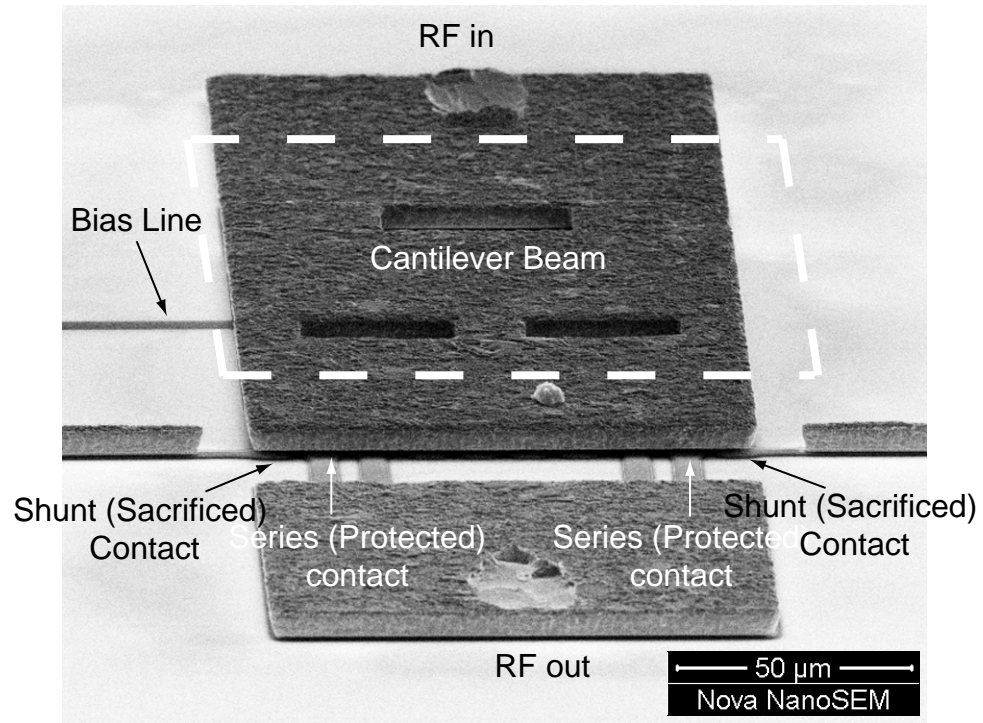
Figure 4.3. Summary of key fabrication process steps of high isolation MEMS switch: (a) SiCr biasline patterning; (b) Bottom gold contact layer; (c) Cu sacrificial layer; (d) Photoresist dimple patterning; (e) Au electroplating for cantilever beam; (f) Released cantilever beam.

and -0.1 dB at 20 GHz is achieved with a bias voltage of 168 V.

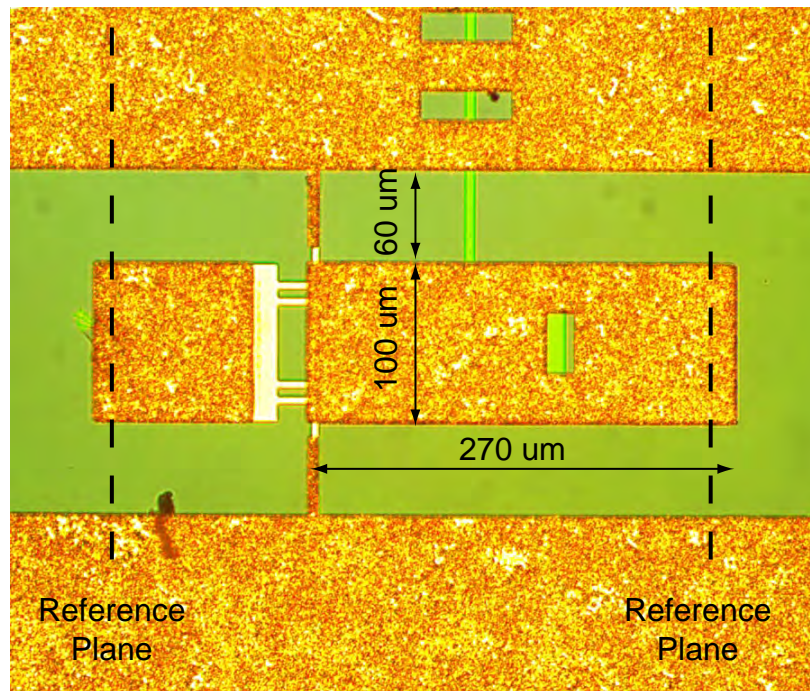
Compared to simulation, the measurement is in excellent agreement. The simulated OFF state isolation is -20.96 dB at 10 GHz and -14.86 dB at 20 GHz. The simulated insertion loss in the closed state is 0.1379 dB at 10 GHz and 0.1672 dB at 20 GHz for a 1Ω contact resistance. Due to the high voltage used to obtain the closed state of the switch, the mechanical force is close to or exceeds 1 mN. This high force facilitates the low on resistance (~ 10 s of $m\Omega$) that is observed in the measurement.

4.4 Conclusion

This chapter presents the design and experimental validation of a novel shunt-series RF MEMS switch with improved off-state isolation. By exploiting the bending mechanics of the MEMS cantilever beam, a high isolation, low insertion loss switch design is accomplished. The MEMS switch has an isolation of -20 dB at 10 GHz and -14.7 dB at 20 GHz in the open state. When the shunt connection is closed,



(a)



(b)

Figure 4.4. (a) SEM of the fabricated RF MEMS switch; (b) Optical image of the switch.

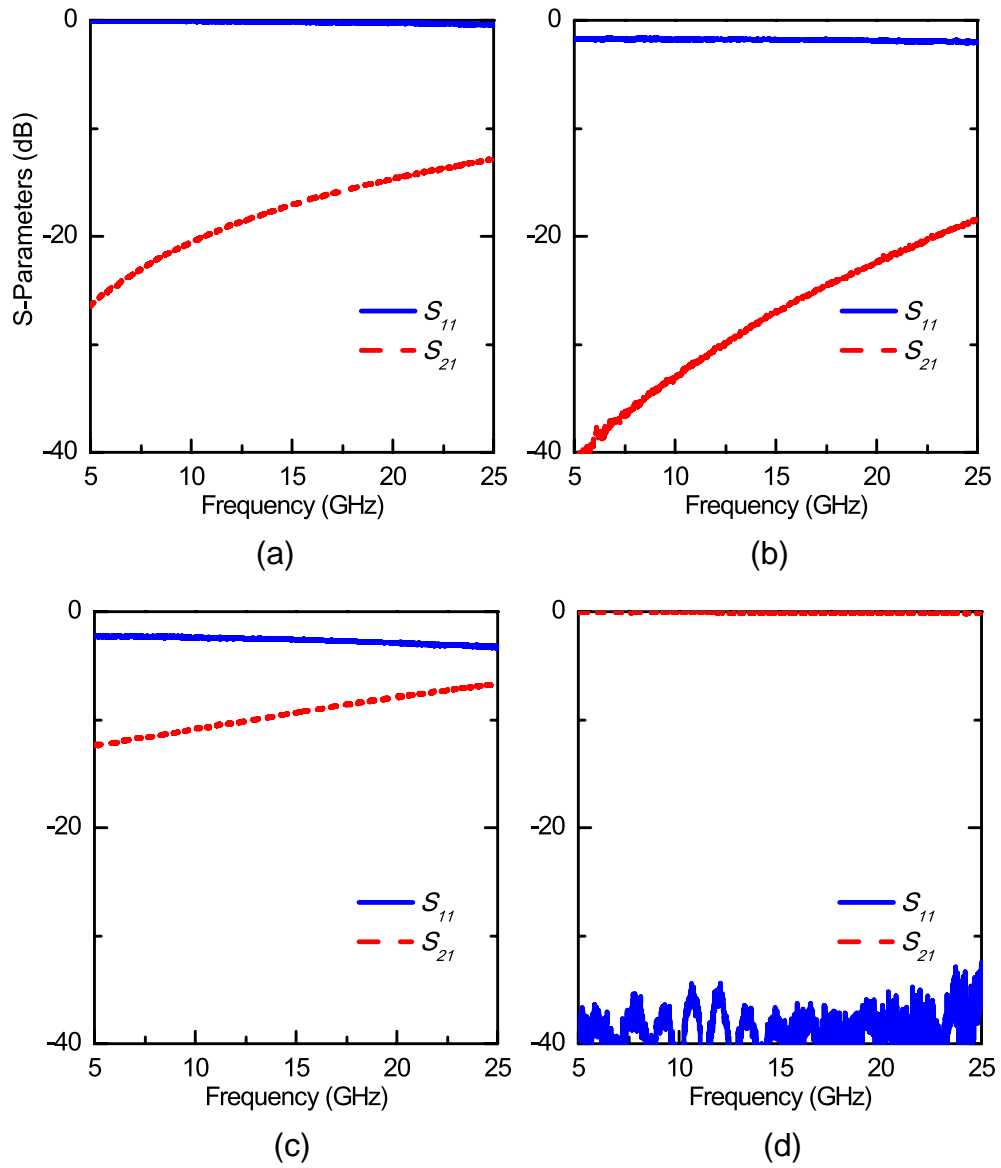


Figure 4.5. Measured performance of the shunt-series switch: (a) Off-state; (b) High isolation state; (c) Transition from high-isolation- to on-state; (d) On state.

the isolation improves to -33 dB at 10 GHz and -22.3 dB at 20 GHz. When series contact is closed and the shunt contact is opened the insertion loss is -0.03 dB at 10 GHz and -0.10 dB at 20 GHz. The proposed structure can replace the switch design in previous chapter to achieve high OFF-state isolation and hot-switching protection in a very compact way.

Appendix A

Metal Contact RF MEMS Switch Fabrication Process

A.1 Introduction

This appendix records the detailed fabrication process for the RF-MEMS switches discussed in chapter 2 and 3. The fabrication process was developed at the CNM2 cleanroom at the University of California Davis. The process is optimized to achieve better switch lifetime and yield than other process found in literatures. The substrate used is high-resistivity silicon wafer coated with thermally grown oxide to reduce the insertion loss and isolate DC current pass.

A.2 Fabrication Process

A.2.1 Wafer Preparation

- (1) Clean the glassware with IPA to remove contamination and particles.
- (2) Rinse the wafer twice with acetone and IPA in ultrasonic cleaner for 2 minutes each.
- (3) Dehydrate the wafer by baking the wafer on hotplate at 120 °for 2 minutes.

A.2.2 Silicon Chrome Biasing Line

- (1) Bake the wafer to dehydrate the surface for 2 minutes.
- (2) Spin PMGI SF6 lift-off photoresist at 4000 rpm for 45 seconds.

- (3) Bake the wafer to dry out the photoresist at 195 °for 2 minutes.
- (4) Spin S1805 photoresist at 3000 rpm for 45 seconds.
- (5) Bake the wafer to dry out the photoressit at 105 °for 2 minutes.
- (6) Pattern the first layer using EVG-620 contact aligner with a lamp intensity of 30 mw/cm².
- (7) Develop in MIF-319 for 17 seconds.
- (8) Inspect the wafer under microscope and descum in oxygen plasma for 30 seconds with low plasma power to remove any photoresist residues.
- (9) Sputter SiCr biasing lines using Lesker Sputterer with the following settings: RF power = 100 W, Pressure = 10 mT, Time = 30 mins on gun 3. The thickness of the biasing line should be around 100 nm.
- (10) Lift off in NMP-based solvent with ultrasonic cleaner for two twenty-minute cycles.

A.2.3 Gold Metal Contact Line

- (1) Bake the wafer to dehydrate the surface for 2 minutes.
- (2) Spin PMGI SF6 lift-off photoresist at 4000 rpm for 45 seconds.
- (3) Bake the wafer to dry out the photoresist at 195 °for 2 minutes.
- (4) Spin S1805 photoresist at 3000 rpm for 45 seconds.
- (5) Bake the wafer to dry out the photoressit at 105 °for 2 minutes.
- (6) Pattern the second layer using EVG-620 contact aligner with a lamp intensity of 30 mw/cm².
- (7) Develop in MIF-319 for 17 seconds.
- (8) Inspect the wafer under microscope and descum in oxygen plasma for 30 seconds with low plasma power to remove any photoresist residues.
- (9) Evaporate gold/titanium using CHA E-Beam Evaporator.
- (10) Lift off in NMP-based solvent with ultrasonic cleaner for two twenty-minute cycles.

A.2.4 Platinum Protection Contact

- (1) Bake the wafer to dehydrate the surface for 2 minutes.
- (2) Spin PMGI SF6 lift-off photoresist at 4000 rpm for 45 seconds.
- (3) Bake the wafer to dry out the photoresist at 195 °for 2 minutes.
- (4) Spin S1805 photoresist at 3000 rpm for 45 seconds.
- (5) Bake the wafer to dry out the photoressit at 105 °for 2 minutes.
- (6) Pattern the third layer using EVG-620 contact aligner with a lamp intensity of 30 mw/cm².
- (7) Develop in MIF-319 for 17 seconds.
- (8) Inspect the wafer under microscope and descum in oxygen plasma for 30 seconds with low plasma power to remove any photoresist residues.
- (9) Evaporate platinum/titanium using CHA E-Beam Evaporator. The desired thickness is 100 nm. Titanium thickness is 25 nm.
- (10) Lift off in NMP-based solvent with ultrasonic cleaner for two twenty-minute cycles.

A.2.5 Chromium Sacrificial Layer

- (1) Bake the wafer to dehydrate the surface for 2 minutes.
- (2) Spin LOR7B lift-off photoresist at 2000 rpm for 45 seconds.
- (3) Bake the wafer to dry out the photoresist at 195 °for 2 minutes.
- (4) Spin S1805 photoresist at 3000 rpm for 45 seconds.
- (5) Bake the wafer to dry out the photoressit at 105 °for 2 minutes.
- (6) Pattern the fourth layer using EVG-620 contact aligner with a lamp intensity of 30 mw/cm².
- (7) Develop in MIF-319 for 25 seconds.
- (8) Inspect the wafer under microscope and descum in oxygen plasma for 30 seconds with low plasma power to remove any photoresist residues.
- (9) Evaporate chromium using CHA E-Beam Evaporator. The desired thickness is 350 nm.

(10) Lift off in NMP-based solvent with ultrasonic cleaner for two twenty-minute cycles.

A.2.6 Dimple Layer

(1) Bake the wafer to dehydrate the surface for 2 minutes.

(2) Spin AZ5214E image reversal photoresist at 3000 rpm for 45 seconds.

(3) Bake the wafer to dry out the photoresist at 105 ° for 2 minutes.

(4) Pattern the fifth layer using EVG-620 contact aligner with a lamp intensity of 30 mw/cm².

(5) Post exposure bake the wafer at 115 ° for 2 minutes.

(6) Flood exposure without mask at lamp intensity of 450 mw/cm².

(7) Develop in AZ developer for 30 seconds.

(8) Inspect the wafer under microscope and descum in oxygen plasma for 30 seconds with low plasma power to remove any photoresist residues.

(9) Evaporate chromium using CHA E-Beam Evaporator. The desired thickness is 500 nm.

(10) Lift off in NMP-based solvent with ultrasonic cleaner for two twenty-minute cycles.

A.2.7 Seed Layer

(1) Bake the wafer to dehydrate the surface for 2 minutes.

(2) Spin AZ5214E image reversal photoresist at 3000 rpm for 45 seconds.

(3) Bake the wafer to dry out the photoresist at 105 ° for 2 minutes.

(4) Pattern the sixth layer using EVG-620 contact aligner with a lamp intensity of 30 mw/cm².

(5) Post exposure bake the wafer at 115 ° for 2 minutes.

(6) Flood exposure without mask at lamp intensity of 450 mw/cm².

(7) Develop in AZ developer for 30 seconds.

(8) Inspect the wafer under microscope and descum in oxygen plasma for 30 seconds with low plasma power to remove any photoresist residues.

(9) Sputter gold/chromium seed layer using Lesker Sputterer with the following settings: RF power = 100 W/300 W, Pressure = 10 mT, Time = 15 mins on gun 3/30mins on gun 5. The thickness of the gold is 50 nm. The thickness of the chromium is 50 nm.

(10) Lift off in NMP-based solvent with ultrasonic cleaner for two twenty-minute cycles.

A.2.8 Plating and Release

(1) Bake the wafer to dehydrate the surface for 2 minutes.

(2) Spin AZ9260 photoresist at 4500 rpm for 45 seconds.

(3) Bake the wafer to dry out the photoresist at 105 °for 10 minutes.

(4) Pattern the seventh layer using EVG-620 contact aligner with a lamp intensity of 300 mw/cm².

(5) Develop in 1:3 diluted AZ400k developer for 180 seconds.

(6) Inspect the wafer under microscope and descum in oxygen plasma for 30 seconds with low plasma power to remove any photoresist residues.

(7) Use Dektak XT profilometer to measure the thickness of photoresist plating mold.

(8) Set up plating solution. Set the plating current to be 2 mA/cm².

(9) Use Dektak XT profilometer to check thickness after plating.

(10) Dice the wafer to get device dies for MEMS release.

(11) Flood exposure on MEMS die with a lamp intensity of 450 mw/cm².

(12) Develop the MEMS die in CD-26 for 5 mins to remove photoresist.

(13) Roughen seed layer using Argon plasma with RF power = 300 W for 1 min.

(14) Etch gold seed layer using gold etchant for 20 seconds.

(15) Etch chromium seed layer and sacrificial layer with chromium etchant for 5 mins.

(16) Soak in DI water for 1 hour.

(17) Soak in DI water for another 4 hours.

- (18) Soak in IPA for 1 hour.
- (19) Soak in IPA for overnight.
- (20) Dry the MEMS die in critical point dryer.
- (21) Store the MEMS die in dehydrate box before testing.

REFERENCES

- [1] R. P. Feynman, "There's plenty of room at the bottom [data storage]," *Journal of Microelectromechanical Systems*, vol. 1, no. 1, pp. 60–66, March 1992.
- [2] *Foundations of MEMS*. Pearson, 2011.
- [3] S. Kamisuki, M. Fujii, T. Takekoshi, C. Tezuka, and M. Atobe, "A high resolution, electrostatically-driven commercial inkjet head," *The Thirteenth Annual International Conference on MEMS*, pp. 793–798, 2000.
- [4] H. Luo, G. K. Fedder, and L. R. Carley, "A 1 mg lateral cmos-mems accelerometer," *The Thirteenth Annual International Conference on MEMS*, pp. 502–507, 2000.
- [5] S. Park and R. Horowitz, "Adaptive control for the conventional mode of operation of mems gyroscopes," *Journal of Microelectromechanical Systems*, vol. 12, no. 1, pp. 101–108, 2003.
- [6] P. F. V. Kessel, L. J. Hornbeck, R. E. Meier, and M. R. Douglass, "A mems-based projection display," *Proceedings of the IEEE*, vol. 86, no. 8, pp. 1687–1704, Aug 1998, 1998.
- [7] T.-W. Yeow, K. L. E. Law, and A. Goldenberg, "Mems optical switches," *IEEE Communications Magazine*, vol. 39, no. 11, pp. 158–163, Nov 2001.
- [8] J. J. Neumann and K. J. Gabriel, "A fully-integrated cmos-mems audio microphone," *12th International Conference on TRANSDUCERS, Solid-State Sensors, Actuators and Microsystems*, vol. 1, pp. 230–233, 2003.
- [9] W. Wang and S. A. Soper, *Bio-MEMS: Technologies and Applications*. CRC, 2007.
- [10] J. Yao, "Rf mems from a device perspective," *Journal of Micromechanics and Microengineering*, vol. 10, no. 4, p. R9, 2000.
- [11] M. C. Wu, O. Solgaard, and J. E. Ford, "Optical mems for lightwave communication," *Journal of Lightwave Technology*, vol. 24, no. 12, pp. 4433–4454, Dec 2006.
- [12] F. Ayazi and K. Najafi, "High aspect-ratio combined poly and single-crystal silicon (harpss) mems technology," *Journal of Microelectromechanical Systems*, vol. 9, no. 3, pp. 288–294, 2000.
- [13] K. Segueni, L. L. Garrec, A.-S. Rollier, R. Robin, S. Touati, A. Kancierzewski, L. Buchaillet, and O. Millet, "Totally free-flexible membrane for low voltage mems metal contact switch," *Microwave Integrated Circuit Conference*, pp. 355–358, 2007.

- [14] Y. Liu, Y. Bey, and X. Liu, "Extension of the hot-switching reliability of rf-mems switches using a series contact protection technique," *IEEE Transactions on Microwave Theory and Techniques*, vol. 64, no. 10, pp. 3151 – 3162, 2016.
- [15] I.-J. Cho, T. Song, S.-H. Baek, and E. Yoon, "A low-voltage and low-power rf mems series and shunt switches actuated by combination of electromagnetic and electrostatic forces," *IEEE Transactions on Microwave Theory and Techniques*, vol. 53, no. 7, pp. 2450–2457, July 2005.
- [16] M. Daneshmand, S. Fouladi, R. R. Mansour, M. Lisi, and T. Stajcer, "Thermally actuated latching rf mems switch and its characteristics," *IEEE Transactions on Microwave Theory and Techniques*, vol. 57, no. 12, pp. 3229–3238, 2009.
- [17] H.-C. Lee, J.-Y. Park, and J.-U. Bu, "Piezoelectrically actuated rf mems dc contact switches with low voltage operation," *IEEE Microwave and Wireless Components Letters*, vol. 15, no. 4, pp. 202–204, 2005.
- [18] G. M. Rebeiz, *RF MEMS: Theory, Design, and Technology*. Wiley, 2003.
- [19] G. M. Rebeiz and J. B. Muldavin, "RF MEMS switches and switch circuits," *IEEE Microwave Magazine*, vol. 2, no. 4, pp. 59–71, 2001.
- [20] C. L. Goldsmith, Z. Yao, S. Eshelman, and D. Denniston, "Performance of low-loss rf mems capacitive switches," *IEEE Microwave and Guided Wave Letters*, vol. 8, no. 8, pp. 269–271, Aug 1998.
- [21] D. Peroulis, S. Pacheco, and L. P. B. Katehi, "Mems devices for high isolation switching and tunable filtering," *IEEE MTT-S International Microwave Symposium Digest, Boston, MA*, June 2000.
- [22] S. Duffy, C. Bozler, S. Rabe, J. Knecht, L. Travis, P. Wyatt, C. Keast, and M. Gouke, "Mems microswitches for reconfigurable microwave circuitry," *Microwave and Wireless Comp. Lett*, 2001.
- [23] J. Maciel, S. Majumder, J. Lampen, and C. Guthy, "Rugged and reliable ohmic MEMS switches," *IEEE MTT-S International Microwave Symposium Digest (MTT)*, pp. 1–3, June 2012.
- [24] G. M. R. et al, "Tuning in to rf mems," *IEEE Microwave Magazine*, vol. 10, no. 6, pp. 55–72, Oct 2009.
- [25] D. Wang, R. Wolf, A. Joseph, A. Botula, P. Rabbeni, M. Boenke, D. Harame, and J. Dunn, "High performance soi rf switches for wireless applications," *10th IEEE International Conference on Solid-State and Integrated Circuit Technology (ICSICT)*, pp. 611–614, 2010.

- [26] A. Basu, G. G. Adams, and N. E. McGruer, “A review of micro-contact physics, materials, and failure mechanisms in direct-contact rf mems switches,” *Journal of Micromechanics and Microengineering*, Sep 2016.
- [27] G.-L. Tan, R. E. Mihailovich, J. B. Hacker, J. F. DeNatale, and G. M. Rebeiz, “Low-loss 2- and 4-bit ttd mems phase shifters based on sp4t switches,” *IEEE Transactions on Microwave Theory and Techniques*, vol. 51, no. 1, pp. 297–304, Jan 2003.
- [28] M. Kim, J. B. Hacker, R. E. Mihailovich, and J. F. DeNatale, “A dc-to-40 ghz four-bit rf mems true-time delay network,” *IEEE Microwave and Wireless Components Letters*, vol. 11, no. 2, pp. 56–58, Feb 2001.
- [29] C. D. Nordquist, C. W. Dyck, G. M. Kraus, I. C. Reines, C. L. Goldsmith, W. D. Cowan, T. A. Plut, I. Franklin Austin, P. S. Finnegan, M. H. Ballance, and C. T. Sullivan, “A dc to 10-ghz 6-b rf mems time delay circuit,” *IEEE Microwave and Wireless Components Letters*, vol. 16, no. 5, pp. 305–307, May 2006.
- [30] N. Somjit, G. Stemme, and J. Oberhammer, “Binary-coded 4.25-bit w-band monocrystalline silicon mems multistage dielectric-block phase shifters,” *IEEE Transactions on Microwave Theory and Techniques*, vol. 57, no. 11, pp. 2834–2840, Nov 2009.
- [31] D. W. Kang, J. G. Kim, B. W. Min, and G. M. Rebeiz, “Single and four-element ka-band transmit/receive phased-array silicon rfics with 5-bit amplitude and phase control,” *IEEE Transactions on Microwave Theory and Techniques*, vol. 57, no. 12, pp. 3534–3543, Dec 2009.
- [32] A. N. et al., “A fully-integrated 16-element phased-array receiver in sige bicmos for 60-ghz communications,” *IEEE Journal of Solid-State Circuits*, vol. 46, no. 5, pp. 1059–1075, May 2011.
- [33] G. M. Rebeiz, C. D. Patel, S. K. Han, K. Chih-Hsiang, and K. M. J. Ho, “The Search for a Reliable MEMS Switch,” *IEEE Microwave Magazine*, vol. 14, no. 1, pp. 57–67, 2013.
- [34] R. Goggin, P. Fitzgerald, B. Stenson, E. Carty, and P. McDaid, “Commercialization of a reliable rf mems switch with integrated driver circuitry in a miniature qfn package for rf instrumentation applications,” *IEEE MTT-S International Microwave Symposium.*, pp. 1–4, 2015.
- [35] M. Daneshmand and R. R. Mansour, “Rf mems satellite switch matrices,” *IEEE Microwave Magazine*, vol. 12, no. 5, pp. 92–109, Aug 2011.
- [36] W. M. van Spengen, “Capacitive rf mems switch dielectric charging and reliability: a critical review with recommendations,” *Journal of*

- Micromechanics and Microengineering*, vol. 22, no. 7, p. 074001, 2012. [Online]. Available: <http://stacks.iop.org/0960-1317/22/i=7/a=074001>
- [37] R. Holm, *Electric Contacts: Theory and Applications*, 4th ed. Springer, 1967.
- [38] D. A. Czaplewski, C. D. Nordquist, C. W. Dyck, G. A. Patrizi, G. M. Kraus, and W. D. Cowan, "Lifetime limitations of ohmic, contacting RF MEMS switches with Au, Pt and Ir contact materials due to accumulation of friction polymer on the contacts," *Journal of Micromechanics and Microengineering*, vol. 22, no. 10, 2012.
- [39] M. Braunovic, N. K. Myshkin, and V. V. Konchits, *Electrical Contacts: Fundamentals, Applications and Technology*, 1st ed. CRC, 2007.
- [40] R. Maboudian and R. T. Howe, "Critical review: Adhesion in surface micromechanical structures," *Journal of Vacuum Science & Technology B, Nanotechnology and Microelectronics: Materials, Processing, Measurement, and Phenomena*, vol. 15, pp. 1–20, 1997.
- [41] A. Basu, R. P. Hennessy, G. G. Adams, and N. E. McGruer, "Hot switching damage mechanisms in mems contacts-evidence and understanding," *Journal of Micromechanics and Microengineering*, vol. 24, no. 10, p. 105004, 2014.
- [42] J. W. McBride, "Electrical contact bounce in medium-duty contacts," *IEEE Transactions on Components, Hybrids, and Manufacturing Technology*, vol. 12, no. 1, pp. 82–90, Mar 1989.
- [43] B. McCarthy, G. G. Adams, N. E. McGruer, and D. Potter, "A dynamic model, including contact bounce, of an electrostatically actuated microswitch," *Journal of Microelectromechanical Systems*, vol. 11, no. 3, pp. 276–283, Jun 2002.
- [44] D. A. C. et al., "A soft-landing waveform for actuation of a single-pole single-throw ohmic rf mems switch," *Journal of Microelectromechanical Systems*, vol. 15, no. 6, pp. 1586–1594, Dec 2006.
- [45] J. C. Blecke, D. S. Epp, H. Sumali, and G. G. Parker, "A simple learning control to eliminate rf-mems switch bounce," *Journal of Microelectromechanical Systems*, vol. 18, no. 2, pp. 458–465, April 2009.
- [46] A. Peschot, C. Poulain, N. Bonifaci, and O. Lesaint, "Contact bounce phenomena in a mem switch," *IEEE 58th Holm Conference on Electrical Contacts (Holm)*, no. 1-7, 2012.
- [47] D. A. Czaplewski, C. D. Nordquist, G. A. Patrizi, G. M. Kraus, and W. D. Cowan, "RF MEMS Switches With RuO₂/Au Contacts Cycled to 10 Billion Cycles," *Journal of Microelectromechanical Systems*, vol. 22, no. 3, pp. 655–661, 2013.

- [48] T. Yamashita, T. Itoh, and T. Suga, "Investigation of anti-stiction coating for ohmic contact {MEMS} switches with thiophenol and 2-naphthalenethiol self-assembled monolayer," *Sensors and Actuators A: Physical*, vol. 172, no. 2, pp. 455 – 461, 2011. [Online]. Available: <http://www.sciencedirect.com/science/article/pii/S0924424711005486>
- [49] D. Peroulis, S. Pacheco, and L. Katehi, "RF MEMS switches with enhanced power-handling capabilities," *IEEE Transactions on Microwave Theory and Techniques*, vol. 52, no. 1, pp. 59–68, Jan 2004.
- [50] M. van Gils, J. Bielen, and G. McDonald, "Evaluation of creep in rf mems devices," *2007 International Conference on Thermal, Mechanical and Multi-Physics Simulation Experiments in Microelectronics and Micro-Systems*, 2007.
- [51] H. H. Hsu, M. Koslowski, and D. Peroulis, "An experimental and theoretical investigation of creep in ultrafine crystalline nickel rf-mems devices," *IEEE Transactions on Microwave Theory and Techniques*, vol. 59, no. 10, pp. 2655–2664, Oct. 2011.
- [52] J. Costa, "RF-MEMS Switch Technology for Radio Front End Applications," in *Workshop WFD: Emerging Applications of RF-MEMS ,IEEE MTT-S International Microwave Symposium (IMS)*, 2009.
- [53] R. P. Hennessy, A. Basu, G. G. Adams, and N. E. McGruer, "Hot-switched lifetime and damage characteristics of MEMS switch contacts," *Journal of Micromechanics and Microengineering*, vol. 23, no. 5, pp. 055 003–055 015, 2013.
- [54] T. Ishida, K. Kakushima, and H. Fujita, "Degradation Mechanisms of Contact Point During Switching Operation of MEMS Switch," *Journal of Microelectromechanical Systems*, vol. 22, no. 4, pp. 828–834, 2013.
- [55] A. Basu, G. G. Adams, and N. E. McGruer, "A review of micro-contact physics, materials, and failure mechanisms in direct-contact rf mems switches," *Journal of Micromechanics and Microengineering*, vol. 26, no. 10, p. 104004, 2016.
- [56] C. Poulain, A. Peschot, M. Vincent, and N. Bonifaci, "A nano-scale investigation of material transfer phenomena at make in a mems switch," in *2011 IEEE 57th Holm Conference on Electrical Contacts (Holm)*, 2011, pp. 1–7.
- [57] T. T. Tsong, "Effects of an electric field in atomic manipulations," *Phys. Rev. B*, vol. 44, p. 13703, 1991.
- [58] Z. Yang, D. Lichtenwalner, A. Morris, J. Krim, and A. I. Kingon, "Contact degradation in hot/cold operation of direct contact micro-switches," *Journal of Micromechanics and Microengineering*, vol. 20, no. 10, p. 105028, 2010.

- [59] R. D. Malucci, "The impact of electro-migration on various contact materials," in *2013 IEEE 59th Holm Conference on Electrical Contacts (Holm 2013)*, 2013, pp. 1–8.
- [60] W. F. Rieder, "Low current arc modes of short length and time: a review," *IEEE Transactions on Components and Packaging Technologies*, vol. 23, no. 2, pp. 286–292, 2000.
- [61] J. Vyskočil and J. Musil, "Cathodic arc evaporation in thin film technology," *Journal of Vacuum Science & Technology A*, vol. 10, no. 4, pp. 1740–1748, 1992.
- [62] F. Charbonnier, "Arcing and voltage breakdown in vacuum microelectronics microwave devices using field emitter arrays: Causes, possible solutions, and recent progress," *Journal of Vacuum Science & Technology B*, vol. 16, no. 2, pp. 880–887, 1998.
- [63] C. D. Patel and G. M. Rebeiz, "A High-Reliability High-Linearity High-Power RF MEMS Metal-Contact Switch for DC to 40-GHz Applications," *IEEE Transactions on Microwave Theory and Techniques*, vol. 60, no. 10, pp. 3096–3112, 2012.
- [64] L. L. W. Chow, J. L. Volakis, K. Saitou, and K. Kurabayashi, "Lifetime Extension of RF MEMS Direct Contact Switches in Hot Switching Operations by Ball Grid Array Dimple Design," *IEEE Electron Device Letters*, vol. 28, no. 6, pp. 479–481, 2007.
- [65] J. M. Gere and S. P. Timoshenko., *Mechanics of Materials*, 4th ed. Nelson Thornes Ltd, 1997.
- [66] H.-H. Hsu, M. Koslowski, and D. Peroulis, "An Experimental and Theoretical Investigation of Creep in Ultrafine Crystalline Nickel RF-MEMS Devices," *IEEE Transactions on Microwave Theory and Techniques*, vol. 59, no. 10, pp. 2655–2664, Oct 2011.
- [67] *Coventorware10*, Coventor Inc., 2015.
- [68] X. Chen and Y. Liu, *Finite Element Modeling and Simulation with ANSYS Workbench*. CRC Press, 2015.
- [69] Y. Liu, Y. Bey, and X. Liu, "Single-actuator shunt-series RF-MEMS switch," in *IEEE MTT-S International Microwave Symposium (IMS)*, 2014, pp. 1–4.
- [70] S. Yong-Ha, K. Min-Wu, L. Jeong Oen, K. Seung-Deok, and Y. Jun-Bo, "Complementary Dual-Contact Switch Using Soft and Hard Contact Materials for Achieving Low Contact Resistance and High Reliability Simultaneously," *Journal of Microelectromechanical Systems*, vol. 22, no. 4, pp. 846–854, 2013.

- [71] S. Yong-Ha, K. Min-Wu, S. Min-Ho, and Y. Jun-Bo, “A complementary dual-contact mems switch using a zipping technique,” *Journal of Microelectromechanical Systems*, vol. 23, no. 3, pp. 710–718, 2014.
- [72] D. M. Pozar, *Microwave Engineering*, 4th ed. Wiley, 2011.